Development of nanomaterials incorporated PDMS-based smart materials for flexible and wearable sensors

A thesis submitted to the University of Hyderabad in partial fulfillment of the requirements for the award of the degree

Doctor of Philosophy (Ph.D.) in Nanoscience and Technology

Submitted by

Bikash Borah Reg. No.12ENPT02

Under the supervision of

Dr. Raj Kishora Dash



School of Engineering Sciences & Technology
University of Hyderabad
Hyderabad-500046,
Telangana, India



CERTIFICATE

This is to certify that the thesis entitled "Development of nanomaterials incorporated PDMS based smart materials for flexible and wearable sensors" submitted by Bikash Borah bearing registration number 12ENPT02 in partial fulfillment of the requirements for the award of Doctor of Philosophy in Nanoscience and Technology in the School of Engineering Sciences and Technology is a bonafide work carried out by him under my supervision and guidance.

This thesis is free from plagiarism and has not been submitted previously in part or in full to this or any other University or Institution for the award of any degree or diploma.

The outcome of the thesis:

- A. Published/Submitted in the following publications:
 - 1. B. Borah, R. K. Dash, G. Raitha. Correlation between the thickness and properties of the ethanol-treated GO-PDMS-based composite material. Journal of Material Sciences: Materials in electronics. 2018, 29, 20216–20224
 - ii. 2. B. Borah, R. K. Dash. A simple and cost-effective approach for producing efficient, flexible, and wearable strain sensors based on laboratory parafilm-based sandwich structure for real-time monitoring human activities. (Manuscript Under Submission)
 - iii. 3. B. Borah, R. K. Dash. Fabrication of Ag-rGO/PDMS flexible polymer composites with high dielectric constant and low loss factor by incorporating low filler content for flexible electronics and energy storage applications. (Manuscript Under Preparation)
- B. Presented in the following conferences:
 - 1. B. Borah, R. K. Dash, "Study of the Electrical, Optical, Thermal and Sensing Properties of the Graphene oxide (GO)-PDMS Flexible Nanocomposite for Sensors and MEMS", *International Conference on Nanotechnology: Idea, Innovations & Initiatives (ICN:31-2017)*, IIT Roorkee, Uttarakhand, 6-8 December 2017.
 - 2. B. Borah, R. K. Dash, "Development of an Ag_rGO/PDMS-based flexible smart composite material for sensor applications", *International conference on functional nanomaterials, IIT BHU 2019*.

Further, the student has passed the following courses towards the fulfillment of coursework requirements for a Ph.D.

Course Code	Name	Credits	Pass/Fail
NT601	Research Methodology	4	Pass

and was exempted from doing coursework (recommended by Doctoral Committee) based on the following course passed during his M. Tech. program (in Int. M.tech./Ph.D. program) and the M.Tech. was awarded:

Course Code	Name	Credits	Pass/Fail
NT401	Thermodynamics and Phase Equilibria	4	Pass
NT402	Characterization of Materials	4	Pass
NT403	Advanced Engineering Mathematics	4	Pass
NT404	Seminar	2	Pass
NT405	Concepts of Nano Science and Technology	4	Pass
NT406	Synthesis and Applications of Nanomaterials	4	Pass
NT407	Materials Processing and Characterization	4	Pass

	Laboratory		
NT408	Polymer Science and Technology	4	Pass
NT451	Nano Biotechnology	4	Pass
NT452	Mechanical Behaviour of Nanomaterials	4	Pass
NT453	Modelling and Simulation	4	Pass
NT454	MEMS and NEMS Nanofabrication Technologies	4	Pass
NT455	Surface Engineering	4	Pass
NT456	Advanced Characterization Techniques	2	Pass
NT457	Laboratory	4	Pass
NT458	Seminar	2	Pass
NT550	Dissertation	18	Pass

Dr. Raj Kishora Dash Supervisor Prof. Dibakar Das Dean, School of Engineering Sciences and Technology, University of Hyderabad



I Bikash Borah, hereby declare that the work reported in the Ph.D. thesis entitled, "Development of nanomaterials incorporated PDMS based smart materials for flexible and wearable sensors" submitted to the University of Hyderabad for the award of Doctor of Philosophy in Nanoscience and Technology in original and was carried out by me during my tenure as a Ph.D. scholar under the supervision of Dr. Raj Kishora Dash, Associate Professor at the University of Hyderabad, India. This thesis has not formed the basis for the award of any degree, diploma, associateship, membership, or similar title of any university or institution. Finally, plagiarism of this thesis is checked and satisfied the requirements.

Bikash Borah

School of Engineering Sciences & Technology

University of Hyderabad

BikahBoral

Hyderabad-500046

India

Place: Hyderabad

Date: 30/08/2021

ACKNOWLEDGEMENTS

I feel privileged to place before you my research work entitled "Development of nanomaterials incorporated PDMS-based smart materials for flexible and wearable sensors". For the overall completion of this research work, I owe its success to numerous diligent personalities.

First and foremost, I wish to place my sincere gratitude to my young, dynamic, and inspiring supervisor Dr. Raj Kishora Dash, Associate Professor, School of Engineering Sciences & Technology, who has provided a considerable wealth of resources, opportunities, and guidance during my whole research work. His support has been an essential factor in the completion of this thesis.

My sincere thanks to my doctoral committee members Prof. M. Ghanashyam Krishna, and Prof. G. Rajaram, School of Physics, UoH, for their kind guidance and support throughout my research work.

I also would like to thank Prof. Dibakar Das, Dean, School of Engineering Sciences and Technology, for his constant suggestions and support towards the completion of my research work in the stipulated time.

I also want to express my sincere thanks to the University Grants Commission, New Delhi, India for the financial support received through the National Fellowship for the OBC candidate.

I also thank all the laboratory technicians for XRD, TEM, FESEM, Raman spectroscopy, SEM for their friendship and technical support.

I also would like to express my sincere thanks to the Centre for Nanotechnology, the University of Hyderabad for helping me to carry out my research work.

I also use this opportunity to convey my thanks to all my group members and fellow students for their cooperation and help.

I would like to take this opportunity to express my thanks to my lab mates and friends Chinmayi, Sandeep, Himadri, Naveen, Deborbrat, Heerock, Manas, Hemanta, Kaushik who helped and supported me in many ways to complete my research work.

Finally, I extend my deep sense of gratitude and thanks to all the teaching and non-teaching staff for their guidance and kind cooperation in the completion of this research work. Last, but not least, I would like to thank my parents for providing an abundance of love, encouragement, and support.

Contents

SI N	0.	Title	Page No.	
I		Contents	[v]	
II		List of Tables	[viii]	
III		List of Figures	[viii]	
IV		List of Abbreviations	[xiii]	
V		List of Publications	[xv]	
VI		Abstract	[xvi]	
Cha	pter 1: Introduction		[1]]
1.1	Introduction		[2]	
1.2	Different types of polymer m	aterials that are utilized for fabricating		
	flexible and wearable strain se	ensors	[4]]
1.3	Different types of nanomater	rials that are utilized for fabricating		
	flexible and wearable strain se	nsors	[6]]
1.4	Literature review		[8]]
1.5	Current challenges		[25	[[
1.6	Objective of the thesis		[27]
Cha	pter 2: Synthesis and Charac	terizations of Nanomaterials	[28]]
2.1	ntroduction		[29]
2.2	Synthesis of GO, rGO, Ag-rGO	, Ag-MWCNT, and Ag-SWCNT nanoma	terials [29]	J
4	2.2.1 Synthesis of Graphene Ox	ide (GO) by improved Hummer's method	1 [29]
2	2.2.2 Synthesis of rGO by chem	ical reduction method using hydrazine mo	onohydrate [2	29
2	2.2.3 Synthesis of Ag_rGO nand	omaterials	[30]]
2	2.2.4 Synthesis of Ag_SWCNT	and Ag_MWCNT nanomaterials	[31]	l
2.3	Characterizations of nanomateri	als	[32]
2	2.3.1 Morphological and compo	ositional study of nanomaterials by FESEM	M [32]]
2	2.3.2 Morphological study of na	nomaterials by TEM	[34]
	2.3.3 Structural analysis of the r	nanomaterials by XRD	[36	П

2.3.4 Molecular vibrational analysis of the nanomaterials by FTIR spectroscopy	[38]
2.3.5 Raman spectroscopy analysis of the nanomaterials	[40]
2.4 Conclusions	[42]
Chapter 3: Fabrication and Characterization of PDMS-Nanofiller-based	
composites	[43]
3.1 Introduction	[44]
3.2 Fabrication of PDMS-Nanofiller composites	[44]
3.3Characterizations of PDMS-Nanofiller composites	[45]
3.3.1 Morphological study of PDMS-Nanofiller composites by SEM	[45]
3.3.2 Structural analysis of PDMS-Nanofiller composites by XRD	[46]
3.3.3 FTIR analysis of PDMS-Nanofiller composites	[48]
3.3.4 Raman analysis of PDMS-Nanofiller composites	[50]
3.3.5 Flexibility and stretchability of PDMS-Nanofiller composites	[52]
3.4. Conclusions	[53]
Chapter 4: Study of electrical properties of PDMS-Nanofiller-based com [54]	ıposites
4.1 Introduction	[55]
4.2 Study of electrical properties of PDMS-Nanofiller composites	[56]
4.3 Study of dielectric properties of PDMS-Nanofiller composites	[57]
4.3.1 Analysis of dielectric permittivity (E') of PDMS-Nanofiller composites	[57]
4.3.2 Analysis of dielectric loss (Tanδ) of PDMS-Nanofiller composites	[64]
4.3.3 Analysis of AC conductivity (σ_{ac}) of PDMS-Nanofiller composites	[68]
4.4 Conclusions	[70]
Chapter 5: Demonstration of PDMS/nanomaterials coated parafilm/PDMS sandwich structure for strain sensing appli	S-based
[72]	ications
9 11	ications [73]
[72]	[73]
[72]5.1 Introduction5.2 Fabrication of different types of PDMS/nanomaterials coated-Parafilm/PDMS	[73] flexible [73]

Chapter 7: References	[95]
Chapter 6: Conclusions	[90]
5.6 Conclusions	[89]
of the human body for a longer duration	[87]
5.6 Demonstration of stability of the fabricated strain sensor in detecting movements	
by using the fabricated strain sensor	[85]
5.5 Demonstration of detection of various movements of the human body	

LIST OF TABLES

Table no.	Description	Page No.
1.1	Summary of different polymers which are used for flexible and wearable strain sensors.	5
1.2	Summary of different nanomaterials which are used for flexible and wearable strain sensors.	7
1.3	Summary of performance characteristics of PDMS-Nanomaterial-based resistive type wearable strain sensors	8
3.1	Specification and wt% of nano-fillers that are utilized for the fabrication of PDMS composites.	45
4.1	Dielectric constant and loss factor of PDMS-Nnaofiller-based composites.	60
5.1	Fabricated sandwich structured PDMS/nanomaterials coated parafilm/PDMS samples	75
5.2	Performance of the sandwich structured strain sensors by applying 35% strain	85
6.1	Comparison of sensing properties of PDMS/Nanomaterials-coated- Parafilm/PDMS-based flexible and wearable sensors with the recently published results.	93

LIST OF FIGURES

Figure	Description	Page
no.		no.
1.1	A brief overview of stretchable and wearable sensors and their applications	2
1.2	(a, b) Schematic representation of two different fabrication processes utilized for flexible sensor structures that are (a) a conductive thin film of nanomaterials such as graphene, CNTs, metal NPs, is encapsulated by two flexible films on top and bottom surface, (b) stretchable and flexible nanocomposites consisting of polymer and nanomaterials with high conductivity that are encapsulated by two flexible films, and (c) Schematic representation of fabrication process for PDMS/MWCNTs composites by using in-situ polymerization	4
1.3	Representation of the molecular formula of PDMS and three-dimensional models of PDMS molecule	6
1.4	Demonstration of various human motion detection experiments by using the rGO/PDMS sensors such as the response of the sensor to the strain applied by the cycle motion of joints of (a) elbow, (b) wrist, (c) knee, (d) abdomen, (e) finger, and (f) human palm	9
1.5	Graphical representation of strain sensing performance of the graphene-coated PDMS sponge based piezoresistive strain sensor which shows (a) the relative change in resistance under 40% applied strain with cycles of stretching and releasing, (b) Current versus voltage characteristics under different applied strain, and (c) relative change of resistance over 15 cycles with time and different maximum strains	10
1.6	Graphical representation of the electromechanical response of the Graphene/PDMS sensor to the applied strain which represents (a) stretching and releasing test with increasing values of the applied strains of 5, 10, 20, 30, 40, 50%, (b) relative change of resistance w.r.t applied strain and (c) Durability of	11

	the sensor under 50% applied strain by stretching and releasing cycles at a rate	
1.7	of 0.5-Hz (a) Experimental setup of the strain sensor and (b) graphical representation of relative resistance vs strain and (c, d) the sensor exhibiting a significant change	12
	in resistance upon stretching and releasing with time	
1.8	(a) Image of the experimental setup for testing of the sensor. Graphical representation of (b) the relative change in resistance vs strain (fragmentized CNT/PDMS composite). (c) the relative change in resistance vs strain curve (unfragmented CNT/PDMS composite) (d) GF as a function of the maximum strain of recently reported resistive-type strain sensors, (e) hysteresis curve of the sensor at 80% strain, (f) frequency response of the sensor at ~10% strain, and (g) the relative change in resistance vs strain of the sensor for more than 10 000 cyclic tension tests	13
1.9	Representation of the fabrication process of CNT films/PDMS sensors which include (a) step-wise illustration of the fabrication process of CNT films/PDMS composite and formation of cracks by pre-stretching, (c) CNT/PDMS sensor after dilution of PDMS solution, infiltration, and curing, (d) photograph of the CNT/PDMS composite cut sample which was attached on a homemade fixing device, (e) morphology of the SEM image showing the network of cracks after pre-stretching, and (f) representation of the sensor that was used in different human body parts for human motion detection	14
1.10	Graphical representation of electromechanical characteristics of the CNT/PDMS-based sensors which illustrate (a) relative resistance change vs strain curves of CNT/PDMS-based sensors (15 layers), which shows two-stage GF behaviors, (b) relative resistance under different applied strains of 5, 10, 20, and 40% for five different cycles, (c) relative resistance vs strain curves in a small region of 1.5% strain, (d) relative resistance change of the sensor during repeated stretching and releasing cycles (1500 cycles) under 20% of applied strain, a relative change in resistance (e) under the bending deformation, and (f) during cyclic inward as well as outward bending tests	15
1.11	Graphical representation of (a-d) the relative change of resistance vs strain of the strain sensors which is based on CNT/PDMS sponges, and (e) sensitivity vs porosity plots of different CNT/PDMS-based sponges	16
1.12	Image of the (a) experimental set-up, and (b) schematic representation of the customized vise. Graphical representation of (c) relative change in resistance in every 2000th cycles from the test that was carried out for 10,000 cycles by utilizing CNT/PDMS (4wt%), (d) resistance change during the test that was carried out for 10,000 number cycles by utilizing CNT/PDMS (4wt%), and (e) resistance vs time for five different cycles such as 100th, 5000th, and 10000th	17
1.13	Graphical representation of the tests which were performed to monitor different human motions by utilizing the fabricated sensors such as bending of (a) finger (b) wrist (c) elbow, (d) knee, (e) squatting, (f) walking, (g) running, and (h) the responses to breathing	18
1.14	(a) Schematically represented the fabrication process of the conductive composite based on Ag flake and PDMS, (b) optical images of the fabricated composite when it was stretched and released by applying 100% strain, (c) conductivity of the composites which varied with the wt% of Ag flakes, and (d) change in electrical conductivity of the composites with different wt% such as 70, 75, 80, 85, and 90 of Ag flakes under the applied strain range from 0 to 100%	19
1.15	(a) Image of the smart glove where the sensors were attached, (b) relative change of resistance in the smart glove for various gestures of the finger, (c) image of the band illustrating the monitoring of the sports performance when forces were applied by using dumbbell of 1 to 4 kg weight, and (d) relative resistance which	20

	changed with time during the monitoring of the sports performance (stretching and releasing) by using the arms	
1.16	(a) Schematic representation of the fabrication process of the sensors that are	20
1.10	based on Ag Nanoparticles and PDMS, and (b) image of the strain sensor which	20
	exhibited excellent flexibility when stretched and twisted	
1.17	Graphical representation of the different rate of change of strain vs resistance,	21
1.1/	(a) 175 wt% at 600 rpm, (b) 200 wt% at 800 rpm, and the respective GF	21
1.18	Schematic representation of the mechanism of sensing by the Ag-rGO/PDMS-	21
1.10		21
	based composite sponge which illustrates the (a) pristine, (b) under pressure, (c)	
	the contacts between the Ag-rGO composites (enlarged version) which depicts the transfer of electrons from AgNPs to rGO sheets and also between the Ag	
	NPs	
1.19		22
1.19	Graphical representation of the hysteresis behavior of the Ag-rGO/PDMS	22
	composite corresponding to the weight ratio of (GO: Ag) (a) 1:1 and (b) 1:2	
	respectively, (c) pressure vs strain plot of PDMS composite-based sponge and	
	(d) relative resistance vs time for dynamic pressure corresponding to the range of	
1.20	pressures (a) Subamatia representation which depicts the stan wise februation process of	22
1.20	(a) Schematic representation which depicts the step-wise fabrication process of	22
1.01	Ag-rGO strain sensors, and (b) cross-sectional representation of the sensor	22
1.21	Graphical illustration of the (a) relative resistance variation of the sensor for	23
	cycle 1, (b) sensitivity (GF) for 0-200% of strain applied, (c) a homemade jig	
	controlling the strain of the sensor, (d) relative resistance variation when the	
	sensor was stretched by applying different strain, (e) current vs voltage	
	characteristics for different strain, and (f) relative resistance when the sensor was	
1.00	subjected to 60% of repeated strain for 500 cycles	22
1.22	Schematic representation of the fabrication process of the strain sensor	23
1.23	Picture of the different tests that were conducted by using the Ag_OH-f-	24
	MWCNT-based portable breathing detector with wrinkled structure (a) breathing	
	in and (b) breathing out. Graphical representation of relative resistance with time	
	which illustrated the expression recognition for (e) facial, (f) frown, and (g)	
	smile respectively	
1.24	Schematic of the process utilized for fabricating the conductive composite and	25
	testing of the wearable sensor in different places of the body, and with different	
	persons such as (a) female, and (b) male respectively	
2.1	Schematic representation of the reduction of GO by hydrazine monohydrate	30
2.2	Schematic representation of the synthesis process for Ag_rGO nanomaterials	31
2.3	Schematic illustration of the synthesis of Ag_SWCNT and Ag_MWCNT	32
2.3	nanomaterials	34
2.4	FESEM image of (a)GO synthesized by improved Hummers method, (b) rGO	33
	synthesized by reduction process using Hydrazine Monohydrate,(c-d) Ag_rGO	
	powder sample synthesized by reduction process using Hydrazine Monohydrate	
	(e, f)Ag_SWCNT and (g, h), Ag_MWCNT nanomaterials at two different	
	magnifications respectively	
2.5	EDS spectra of (a) Ag_rGO, (b) Ag_SWCNT, and (b) Ag_MWCNT powder	34
	samples respectively	
2.6	TEM image of (a) GO that was synthesized by improved Hummer's method, (d)	35
	rGO synthesized by reduction process using Hydrazine Monohydrate, (g)	
	AgNPs, and (h) Ag_rGO powder sample synthesized by reduction process using	
	Hydrazine Monohydrate respectively. TEM image showing the numbers of	
	layers of (b) GO and (e) rGO respectively. SAED pattern of (c) GO, (f) rGO, and	
	layers of (b) GO and (c) IGO respectively. SALD pattern of (c) GO, (1) IGO, and I	
	(i) Ag_rGO respectively	

2.7	TEM images for (a,b) Ag_MWCNT and (d,e) Ag_SWCNT nanomaterials at two different magnifications respectively. SAED pattern of (c) Ag_MWCNT and (f) Ag_SWCNT respectively	36
2.8	XRD pattern of GO synthesized by improved Hummers method, rGO synthesized by chemical reduction process using Hydrazine Monohydrate, AgNPs, and Ag_rGO nanomaterials synthesized by reduction process using Hydrazine Monohydrate respectively	37
2.9	(a) XRD pattern of Ag/SWCNT and (b) Ag/MWCNT nanomaterials respectively	38
2.10	FTIR spectra of GO, rGO, AgNPs, and Ag_rGO powder sample synthesized by reduction process using Hydrazine Monohydrate respectively	39
2.11	FTIR spectra of (a) SWCNT, Ag_SWCNT, and (b) MWCNT, Ag_MWCNT nanomaterials respectively	39
2.12	Raman spectra of GO, AgNPs, rGO, and Ag_rGO powder sample synthesized by chemical reduction process using Hydrazine Monohydrate respectively	40
2.13	Raman spectra of (a) SWCNT, Ag_SWCNT, and (b) MWCNT, Ag_MWCNT nanomaterials respectively	41
3.1	Schematic presentation of the PDMS nanocomposites fabrication process	44
3.2	The SEM micrograhs of 1 wt% GO/PDMS (a, b), Ag/PDMS (c, d), rGO/PDMS (e, f), Ag_rGO/PDMS (g, h), Ag_SWCNT/PDMS (i, j), and Ag_MWCNT/PDMS (k, l) respectively in two different magnification (100µm and 50µm).	46
3.3	XRD pattern of (a) GO/PDMS, (b) Ag/PDMS (c) rGO/PDMS, (d) Ag_rGO/PDMS, (e) Ag_SWCNT/PDMS and (f) Ag_MWCNT/PDMS polymer composites fabricated by incorporating nanofillers with different wt%.	47
3.4	FTIR spectra of (a)GO/PDMS (b) Ag/PDMS (c) rGO/PDMS, (d) Ag_rGO/PDMS, (e) Ag_SWCNT/PDMS and (f) Ag_MWCNT/PDMS composites with different wt% respectively	49
3.5	Raman spectra of neat PDMS	50
3.6	Raman spectra of (a) GO/PDMS, (b) Ag/PDMS, (c) rGO/PDMS, (d) Ag_rGO/PDMS, (e) Ag_SWCNT/PDMS and (f) Ag_MWCNT/PDMS composites with different wt% respectively	51
3.7	(a) Different modes of deformation to show the flexibility and stretchability of GO/PDMS, Ag/PDMS, rGO/PDMS, and Ag_rGO/PDMS composites (1 wt%) (b) Different modes of deformation to show the flexibility and stretchability of Ag_SWCNT/PDMS and Ag_MWCNT/PDMS composites (1wt%).	52
4.1	Photograph of "NovoConrtroll Dielectric Measurement System" and sample holder	55
4.2	I-V characteristics curve of the PDMS-Nanofiller-based composites	56
4.3	Dielectric constant of (a) GO/PDMS, (b) Ag/PDMS, (c) rGO/PDMS, (d) Ag_rGO/PDMS, (e) Ag_SWCNT/PDMS and (f) Ag_MWCNT/PDMS flexible polymer composites with different wt% of nanofillers respectively	58
4.4	(a-b) Comparison of dielectric permittivity of PDMS nanocomposites with different wt% of nanofillers at 1Hz and 10Hz frequency and (c-d) Graphical representation of dielectric permittivity of PDMS nanocomposites with 1wt% of nanofillers at 1 Hz and 1kHz AC frequency respectively.	59
4.5	FESEM image of 1 wt% (a) GO/PDMS, (b) Ag/PDMS and (c) Ag_rGO/PDMS nanocomosites and (d) TEM image of SWCNT and (e) MWCNT nanofillers	61
	respectively	
4.6	Schematic illustration of the distribution of nanofillers in the PDMS-Nanofiller-based composites	62

	Ag_rGO/PDMS, (e) Ag_SWCNT/PDMS and (f) Ag_MWCNT/PDMS flexible	
	polymer composites with different wt% respectively	
4.8	(a-b) Comparison of dielectric loss factor of PDMS nanocomposites with different wt% of nanofillers at 1Hz and 10Hz frequency and (c-d) Graphical representation of dielectric loss factor of PDMS nanocomposites with 1wt% of nanofillers at 1 Hz and 1kHz AC frequency respectively.	66
4.9	AC conductivity of different wt% of (a) GO/PDMS, (b) Ag/PDMS, (c) rGO/PDMS, (d) Ag_rGO/PDMS, (e) Ag_SWCNT/PDMS and (f) Ag_MWCNT/PDMS flexible polymer composites respectively	68
4.10	(a-b) Comparison of AC conductivity of PDMS nanocomposites with different wt% of nanofillers at 1Hz and 10Hz frequency respectively.	69
5.1	Schematic representation of the (a) preparation of nanomaterials coated parafilm for the fabrication of strain sensor, (b-c) Parafilm used for the fabrication process, and (d) the fabricated nanomaterials coated Parafilm	74
5.2	(a) Schematic representation which shows the step-wise fabrication of sandwich structure (PDMS/nanomaterials coated parafilm/PDMS) to be used as a strain sensor (b) fabricated PDMS/nanomaterials coated parafilm/PDMS sandwich structure, and (c) schematic representing the fabricated sandwich structure	74
5.3	FESEM images (cross-sectional view) of the samples (a) 1, (c) 2, (e) 3, and (g) 4 sandwich structure and (b, d, f, h) morphology of the cross-section of the samples respectively	76
5.4	Optical images of the (a) and (b) experimental set-up for the measurement of I-V characteristics and relative change in resistance with the applied strain, (c), (d), and (e) twisting, bending, and stretching deformation of the sandwich structures, and (f) relaxed state of the sensor. (g) The schematic diagram for the measurement of I-V characteristics	80
5.5	LED testing of all the fabricated samples indicates that at 20v, the LED glow is more for samples with higher conductivities. The LED light intensity of (b) Sample 2 is higher than (a) Sample 1 and the (d) Sample 4 LED intensity is higher than (c) Sample 3 which confirms the results obtained from IV measurements as stated above	78
5.6	(a) I-V characteristics curve of the sandwich structure of PDMS/Nanomaterials coated Parafilm and (b) Graphical representation of conductivities of all the samples	78
5.7	Graphical representation of (a, b, c, and d) change in resistance with changing the voltage of the sandwich structured sample 1, 2, 3, and 4 for testing twisting and bending deformations respectively	79
5.8	(a) The 4-Wire Ohms configuration used for the measurement of change in resistance by applying a longitudinal strain and (b) strain measurement by equally pulling both the end of the samples	80
5.9	Graphical presentation of (a) △ R/R0 and (b) GF of all the fabricated samples with applied strain	81
5.10	Graphical representation of (a) △ R/R0 and (b) GF of the fabricated sandwich structure samples	82
5.11	Schematic representation of variation in the conductive network of the (a) rGO, (b) Ag_rGO, (c) SWCNTs, and (d) Ag_SWCNT-based samples under applied strain	83
5.12	Relative resistance of the (a) PDMS/rGO-Parafilm/PDMS, (b) PDMS/Ag_rGO-Parafilm/PDMS, (c) PDMS/SWCNT-Parafilm/PDMS, and (d) PDMS/Ag_SWCNT-Parafilm/PDMS samples under applied strain and relaxation	85
5.13	Detection of various movements of the human body by the fabricated sensors: (a) Response of the sensors to the strain which was applied by the cycle motion of the index finger (i-iv) and (b) elbow (v-viii) and the wrist (ix-xii) respectively	86-87

List of Acronyms, Abbreviations, and Units of measure.

- PDMS-- polydimethylsiloxane
- PVA-- poly(vinyl alcohol)
- PU-- polyurethane
- TPU—Thermo polyurethane
- PS—polystyrene
- PEDOT: PSS-- poly(3,4ethylenedioxythiophene): poly(styrene sulfonate)
- SEBS-- styrene-ethylene-butylene-styrene
- SR-- Silicon Rubber
- SBR--Styrene-butadiene rubber
- Å-- Angstrom
- CNT Carbon Nanotubes
- CB-- Carbon Black
- SWCNT-- single-walled carbon nanotube
- MWCNT-- multi-walled carbon nanotube
- GO-- graphene oxide
- rGO—reduced graphene oxide
- AgNPs-- silver nanoparticles
- NPs—Nanoparticles
- NCs-- Nanocrystals
- GA-- graphene aerogel
- GNPs-- graphene nanopellets
- Ag-rGO-- silver nanoparticles- reduced graphene oxide
- Ag-SWCNT-- silver nanoparticles- single-walled carbon nanotube
- Ag-MWCNT-- silver nanoparticles- multi-walled carbon nanotube
- GF-- gauge factor
- EDS-- Energy Dispersive Spectroscopy
- FESEM-- Field Emission Scanning Electron Microscopy
- FTIR-- Fourier-Transform Infrared Spectroscopy
- HRTEM-- High-Resolution Transmission Electron Microscopy

- SAED Selected Area Electron Diffraction
- SEM Scanning electron microscopy
- XRD X-ray Diffraction
- TEM Transmission electron microscopy
- TGA-- thermo-gravimetric analysis
- wt%-- weight percent
- gm Gram
- H₂SO₄ Sulphuric Acid
- H₃PO₄—phosphoric acid
- H₂O₂ Hydrogen peroxide
- HCL Hydrochloric acid
- KMnO₄ Potassium Permanganate
- DI water-- Deionized water
- Cu-- copper
- hr Hour
- H.H Hydrazine Hydrate
- ID Identity
- I-V Current Voltage
- I_D/I_G ratio Intensity ratio of D band and G band
- K − Kelvin
- MPa-- megapascal
- GPa—Gigapascal
- mL Millilitre
- mg Milligram
- MW Molecular weight
- mm Millimetre
- cm-- centimetre
- µm --Micrometre
- V -- Volt
- NW Nanowires
- \bullet nm Nanometre
- pH Potential for Hydrogen
- RT Room temperature
- AC--Alternating Current
- Hz--hertz

- kHz—kilohertz
- MΩ--Mega Ohm
- GΩ--Giga Ohm
- AC Frequency-- alternating current frequency
- DC Direct Current
- 1D One Dimensional
- 2D Two Dimensional
- °C Celsius or Centigrade
- LED—light-emitting diode

List of publications/Conferences

A. Published/Submitted in the following publications:

- 1. "Correlation between the thickness and properties of the ethanol-treated GO-PDMS-based composite material." B. Borah, R. K. Dash, G. Raitha. Journal of Material Sciences: Materials in electronics, 2018, 29, 20216–20224.
- 2. "A simple and cost-effective approach for producing efficient, flexible, and wearable strain sensors based on laboratory parafilm-based sandwich structure for real-time monitoring human activities." B. Borah and R. K. Dash. (Manuscript under Submission)
- 3. "Fabrication of Ag-rGO/PDMS flexible polymer composites with high dielectric constant and low loss factor by incorporating low filler content for flexible electronics and energy storage applications." B. Borah and R. K. Dash. (Manuscript under preparation)

B. Presented in the following conferences:

- iii. B. Borah, R. K. Dash, "Study of the Electrical, Optical, Thermal and Sensing Properties of the Graphene Oxide (GO)-PDMS Flexible Nanocomposite for Sensors and MEMS", International Conference on Nanotechnology: Idea, Innovations & Initiatives (ICN:3I -2017), IIT Roorkee, Uttarakhand, 6-8 December 2017.
- iv. B. Borah, R. K. Dash, "Development of an Ag_rGO/PDMS-based flexible smart composite material for sensor applications", International conference on functional nanomaterials, IIT BHU 2019.

ABSTRACT

The recent electronic sensor technology demands the use of materials that are lightweight, mechanically flexible, and stretchable, and cost-effective. Polymer-based composites produced by reinforcing hybrid nanomaterials meet the demands for such applications owing to their excellent electrical properties, lightweight, flexible and stretchable nature. Therefore, polymer and nanomaterials-based flexible composites have been emerging as new generation smart materials and immensely studied for applications such as wearable electronic devices, supercapacitors, flexible display, touch screen, human health monitoring, human motion detection, facial recognition, and human-machine interfaces, etc. In this work, the fabrication and testing of nanomaterials incorporating poly(dimethylsiloxane) (PDMS)-based flexible composites and sandwich structures for flexible and wearable sensors are demonstrated. Two different approaches were adopted to fabricate PDMS-based flexible materials. The first one is the fabrication of PDMS-based composite materials by incorporating different wt% of nanomaterials in the PDMS polymer matrix by using a simple solution mixing process. The second one is the fabrication of a sandwich structure of PDMS/nanomaterials coated parafilm/PDMS by a simple cost-effective method. For this purpose, firstly, different nanomaterials such as GO, rGO, AgNPs, Ag_rGO, Ag_SWCNT, and Ag_MWCNT were synthesized and used. The morphology of the synthesized nanomaterials was studied by using FESEM and TEM. The structural analysis of the nanomaterials and PDMS composites was carried out by XRD, FTIR, and Raman spectroscopy. Secondly, the dielectric properties of the PDMS composites were investigated and it was found that the dielectric properties were improved due to the incorporation of nanomaterials in the polymer matrix. The dielectric properties of the PDMS composites increase with the increase in wt% of the nanomaterials in the lower frequency region (1Hz). The AgNPs played a major role to improve the dielectric properties of the PDMS composites fabricated by incorporating Ag_rGO and Ag_SWCNT nanomaterials. It was found that the Ag_rGO/PDMS and Ag_SWCNT/PDMS composites exhibited better improvement in dielectric properties than the other PDMS-based composites. The highest value of dielectric constant was obtained for 1 wt% Ag rGO/PDMS ($\varepsilon' = 108$, $Tan\delta = 0.98$) and Ag_SWCNT/PDMS (E' = 85, $Tan\delta = 0.15$) composites. Finally, the PDMS/nanomaterials coated parafilm/PDMS-based sandwich structures were fabricated by using a simple and cost-effective method. From the study of electrical and strain sensing characteristics of the sandwich structures, it was observed that the strain sensors exhibited good electrical conductivity, a good response to the applied strain, and good sensitivity,

linearity, and repeatability. The AgNPs enhanced the conductivity and sensitivity of PDMS/Ag_rGO-Parafilm/PDMS and PDMS/Ag_SWCNT-Parafilm/PDMS-based sandwich structure by forming an electrical bridge by sitting between the rGO sheets and also between the CNTs. The highest relative resistance (347%), and gauge factor (GF = 10) was achieved for PDMS/Ag_rGO-Parafilm/PDMS-based sandwich structure. The sandwich structure-based strain sensors demonstrated excellent performance to monitor different movements of the human body parts in real-time such as the cycle of motion of index finger, elbow, and wrist joints with better response time. Therefore, we successfully demonstrated that the PDMS and parafilm-based flexible strain sensors have the potential to be utilized for applications such as wearable devices and for the detection of human sensors motions.

CHAPTER 1

Introduction and Literature Review

1.1 Introduction

Sensors are integral parts of all the technology sectors in modern society from automobiles to smart-phone, computers to the smart-watch, biomedical, healthcare to household items, manufacturing, and beyond. In the present technology-driven society, sensors have been playing an indispensable role in daily life to monitor physical health, human motion detection, exercise, and sports activities, weather, and the environment, etc. The developments of flexible materials such as polymers, fabrics, textiles have promoted the fabrication of flexible sensors in the last few decades and the demands for flexible and wearable sensors have been increasing globally. Conventional electronic devices are based on thin-film materials such as Si (silicon), metal, and metal oxide (ITO, Au, Cu, etc.), and organic materials [1].

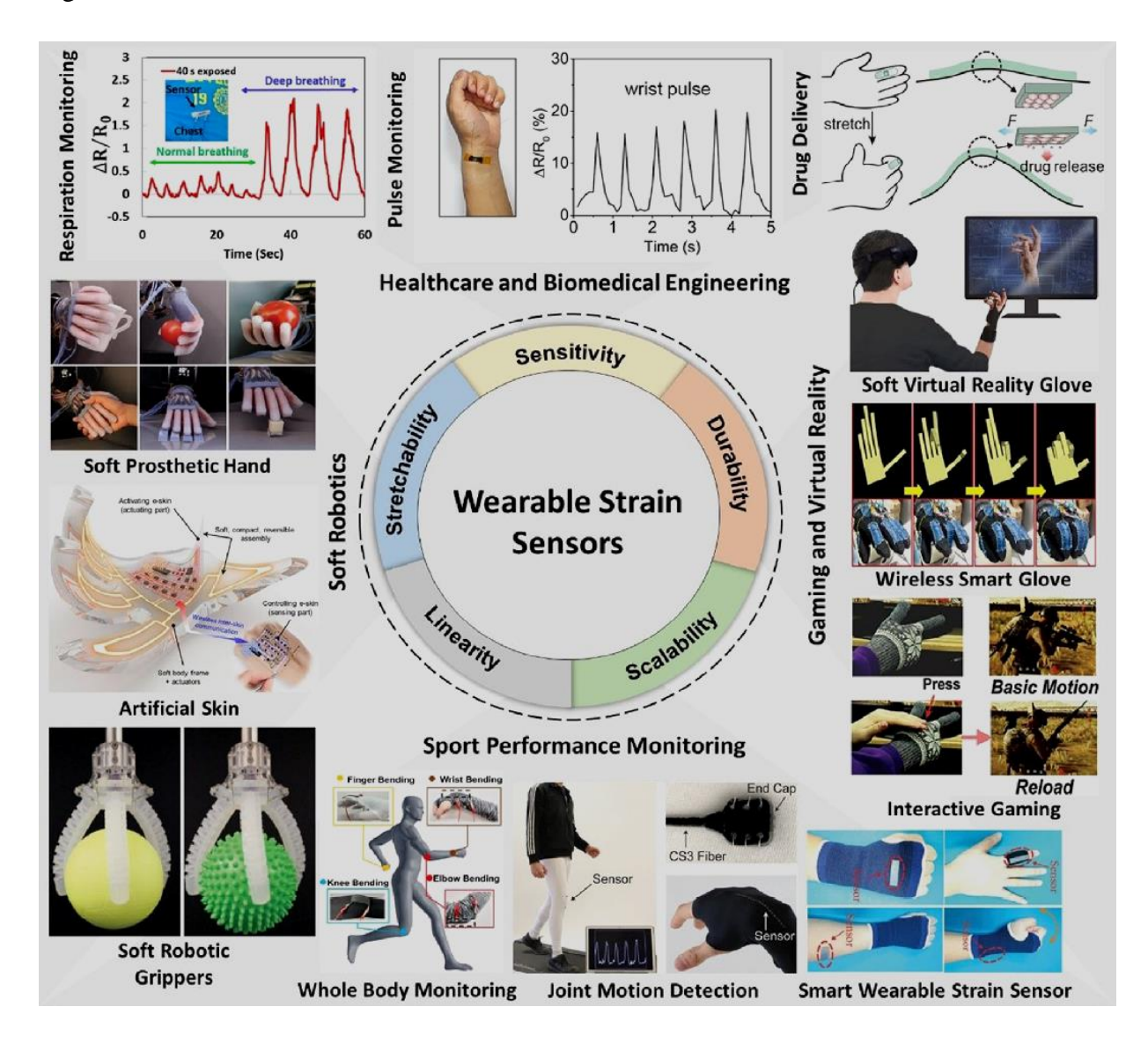


Fig. 1.1 A brief overview of stretchable and wearable sensors and their applications [4]

Although the conventional sensors show high electrical performance, accurate physiological responses are not easy to obtain because of the inability to make strong contact with the human body [1, 2]. Besides, they have limited use for skin attachment, biocompatibility, and applications that require large deformations such as bending, stretching, and twisting due to their brittle and rigid nature [2, 3]. Therefore, flexible/stretchable and wearable sensors have received overwhelming attention and have been extensively studied over the last decades due to the easy interaction with the human skin, body joints and usefulness for real-life based applications such as detection of human motion, soft robotics, sports performance monitoring, healthcare, and biomedical engineering, etc [4---10]. A brief overview of flexible, wearable, and stretchable sensors and their different applications is illustrated in Fig. 1.1 [4]. The key features of flexible and wearable strain sensors are lightweight, stretchability, flexibility, biocompatibility, ease of production, high sensitivity, dynamic durability, linearity, mechanical stability, excellent electrical and dielectric properties [2, 4, 11, 12].

Flexible and wearable sensors mainly consist of two components such as sensing material (conductive nanomaterial) and flexible/stretchable materials (flexible polymer or fabrics). The external mechanical stimuli through various deformations such as stretching, bending, and twisting are transmuted by the sensing material to electrical signals [13]. There are several reported methods to fabricate flexible and wearable sensors. Among them, one of the common methods involves the deposition of conductive nanomaterials over the surface of flexible and stretchable substrates such as a polymer or textile/fabrics, or integration of a laminar conductive film into the substrate which is illustrated in Fig. 1.2 (a) [14]. Another method involves the incorporation of nanomaterials into the bulk of the flexible polymers by employing different methods such as solution blending, latex-blending, melt mixing, and insitu polymerization to form conductive pathways inside the non-conductive polymer matrix [15, 16]. Fig. 1.2 (b) shows the example of this method. In polymer-nanomaterial composites, the combination of properties and interaction of the host polymer and nanomaterials are the key factors that alter the mechanical (flexibility and stretchability), electrical and dielectric properties of the host polymer. Therefore, polymer-based nanocomposites have been emerging as the new generation smart material for various applications such as flexible electronics, wearable sensors, actuators, biomedical devices, energy harvesting, energy storage, and super-capacitors, etc. [17---21]. Based on the performance and response to the external mechanical stimuli, strain sensors are classified into several types such as piezoelectric, turboelectric, resistive, capacitative, and optical strain sensors, etc [4].

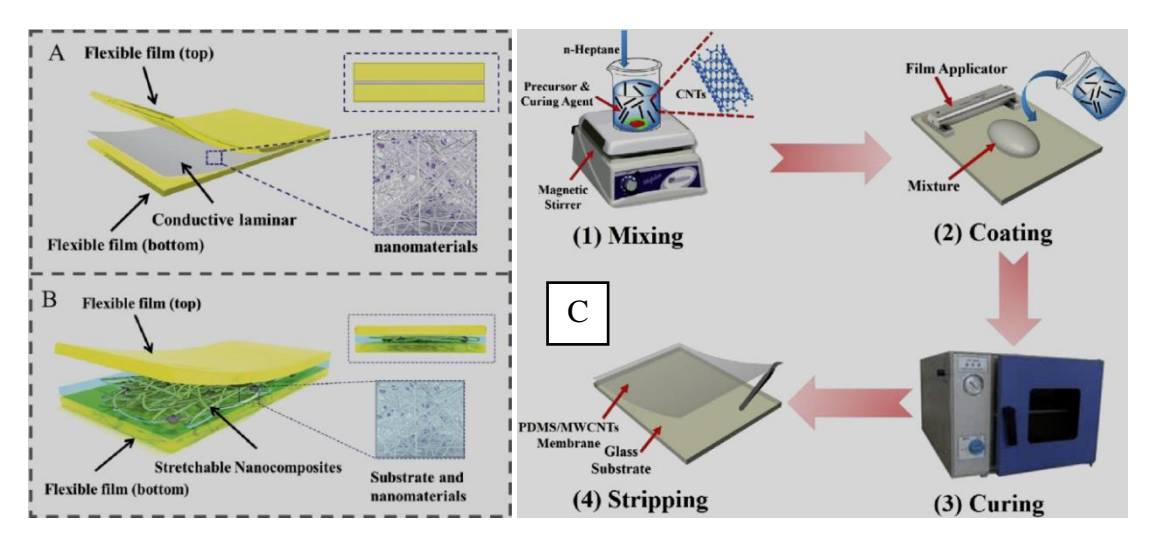


Fig. 1.2 (a, b) Schematic representation of two different fabrication processes utilized for flexible sensor structures that are (a) a conductive thin film of nanomaterials such as graphene, CNTs, metal NPs, is encapsulated by two flexible films on top and bottom surface, (b) stretchable and flexible nanocomposites consisting of polymer and nanomaterials with high conductivity that are encapsulated by two flexible films [14], and (c) Schematic representation of fabrication process for PDMS/MWCNTs composites by using in-situ polymerization [16].

In context to our work which will be presented, the thesis only emphasizes the flexible polymer-based resistive type wearable strain sensors. In the resistive type flexible strain sensors, the conducting pathways formed by the nanomaterials serve as a resistor, and the relative change in electrical resistance corresponding to the applied mechanical strain such as stretching, bending, and twisting can be monitored. The electrical resistance in such strain sensors changes due to the change in the geometry of the active material, tunneling effect, and disconnection in some parts of the conductive pathways formed by the overlapped nanomaterials through opening or closing of micro-cracks [4, 22]. The flexible and wearable polymer-based strain sensors containing conductive nanomaterials can maintain their conductive pathways under very large strain and restore their original properties after the withdrawal of the mechanical strain which makes the flexible polymer-based sensors robust for strain sensing applications.

1.2 Different types of polymer materials that are utilized for fabricating flexible and wearable strain sensors.

Various polymers such as polydimethylsiloxane (PDMS), poly(vinyl alcohol) (PVA), hydrogel, polyurethane (PU), polystyrene (PS), poly(3,4ethylenedioxythiophene):

poly(styrene sulfonate) (PEDOT: PSS), styrene-ethylene-butylene-styrene (SEBS), etc., have been investigated based on their mechanical properties (for example elastic modulus) and biocompatibility [39---43]. Some of the polymers and their elastic modulus are given in Table 1.1.

Table 1.1 Summary of different polymers which are used for flexible and wearable strain sensors.

Polymer	Elastic Modulus GPa	Sensor System	References
PDMS	0.00057-0.0037	Graphene/CNT/PDMS, Au/Ni/PDMS	[23, 24]
SR (Silicon Rubber)	0.001-0.05	Graphene/SR	[25]
SEBS	0.34-0.38	CNT/SEBS CNT/graphene/fullerene/SEBS	[26, 27]
PEDOT	0.9-2.8	Ag NPs/CNTs/PEDOT:PSS	[28]
PU	0.015-0.15	AgNW/graphene/fullerene/PU RGO/PU	[29, 30]
TPU	2.4*10 ⁻⁶	RGO/TPU, Grahene/TPU	[31, 32]
Hydrogel	-	SWCNT/Hydrogel	[33]
PVA	1.5-3.75	PVA-FSWCNT-PDA hydrogels	[34]
SBR (Styrene- butadiene rubber)	0.00025-0.00083	Carbon black/SBR	[35]
PET	2.76-4.14	Graphene/PET	[36]
Natural Rubber	ober 0.01-0.1 CNT/NR RGO foam/NR		[37, 38]

The main challenge to use polymers for sensing applications is their poor electrical properties. Therefore, conductive nano-fillers have been incorporated in the insulating polymer matrix or conductive nanomaterials have been deposited on the top of polymer substrate to fabricate the flexible, stretchable, and conductive polymer-nanomaterial system. The dispersion of nano-filler materials in the polymer matrix via the interaction of nanomaterials and polymer matrix is a key factor in fabricating polymer-nanomaterial composites. Out of different polymers which have been used for flexible and wearable electronics, PDMS (Polydimethylsiloxane) is a silicon-based organic insulating elastomer that is very popular. PDMS has fascinating properties such as non-toxicity, high glass transition temperature, chemical stability, the low mass density of 0.97 kg/m³, high

flexibility, and stretchability (PDMS has Young's modulus of 60-870 KPa, Poisson ratio 0.5, tensile strength 2.24 MPa), due to the presence of Si-O-Si backbone [44, 45]. The molecular formula and 3-D model of PDMS are shown in Fig. 1.3 [16] Pristine PDMS has a dielectric constant of 2.3-2.8 and an index of refraction 1.4. Solid PDMS is resistant to most of the aqueous and organic solvent but some of the solvents such as xylene can swell PDMS. Moreover, pure PDMS shows low surface tension and hydrophobicity. The viscoelastic, optically transparent, biocompatible nature of the polymer along with cost-effectiveness endows PDMS the usefulness for practical applications.

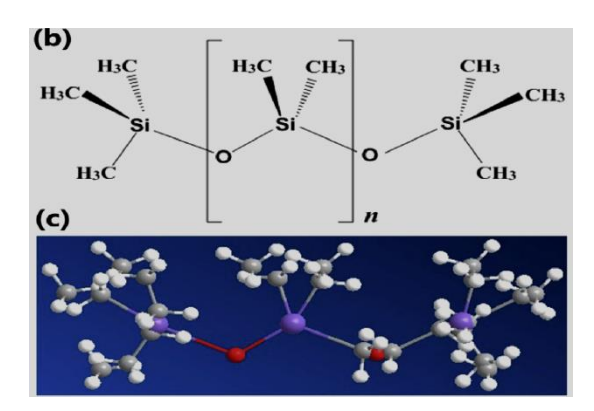


Fig. 1.3 Representation of the molecular formula of PDMS and three-dimensional model of PDMS molecule [16].

1.3 Different types of nanomaterials that are used for fabricating flexible and wearable strain sensors.

Nanomaterials play a major role in fabricating the hybrid sensitive unit material which acts as a sensing part in the flexible and wearable strain sensors. Conductive nanomaterials of different types such as metal NPs, metal oxide NPs, and carbon-based nanomaterials have been extensively investigated with flexible polymers for flexible and wearable strain sensor-based applications. Some notable examples of the PDMS and different nanomaterials-based wearable strain sensors are given in table 1.2. Out of different conductive nanomaterials, carbon-based nanomaterials which includes single-walled carbon nanotube (SWCNT), multi-walled carbon nanotube (MWCNT), graphene, and graphene oxide (GO) have been used for flexible electronic based applications because they possess large surface area, high aspect ratio, excellent mechanical properties, excellent electrical and chemical properties [63---65]. Carbon nanotubes are attractive nano-filler material due to their excellent electrical and thermal conductivity depending upon the chirality of the graphite lattice, flexibility, high aspect ratio (typically >1000), high Young's modulus of around 200-1000 GPa, and tensile strength of around 200-900 MPa [66---70]. For all of these intriguing properties, CNTs have

been used as a reinforcing material in a polymer matrix and to fabricate flexible wearable strain sensors which will be discussed in the literature review. The sp^2 hybridized carbon nano-sheet or graphene, on the other hand, is the most widely studied 2-D material which has unique properties such as high mechanical strength (Young's modulus 1TPa), high fracture strength (130 GPa), high carrier mobility (350000 cm²/(Vs), high thermal conductivity (~3000 W m⁻¹K⁻¹), high electrical conductivity (~6×10³ S/cm) and high theoretical surface area (~2630 m²g⁻¹) [11, 15, 17, 71, 72].

Table 1.2 Summary of different nanomaterials which are used for flexible and wearable strain sensors.

Nanomaterial	Stretchability %	Gauge Factor	References	
Graphene	70, 12, 20, 7, 32	15-29, 27-164, 42, 2.4-	[46, 25, 47, 48, 49]	
		14, 32		
CNTs	280, 100	0.82, 2*104	[50, 51]	
CNT/Graphene	85	20.5	[52]	
EGaIn-PDMS	350	1.6-3.2	[53]	
Carbon Black (CB)	10	5.5	[54]	
CNT/CB	22	29	[55]	
Ag NWs	17, 60, 35, 50	2-14, 9557, 20. NA,	[8, 56, 57, 58]	
Ti_3C_2Tx	50	100	[59]	
Au-TiO ₂ NWs	100	NA	[60]	
Au/Ni	30	NA	[61]	
CNTc/Au NPs/PDMS	50	70	[62]	

The graphene oxide (GO) is produced by oxidizing graphitic layers of pure graphite flakes by a chemical process and hence GO contains the oxygenated functional groups that include hydroxyl (-OH), alkoxy (C-O-C), carbonyl (C=O), and carboxylic (-COOH) groups on its surface and along the edges [73, 74]. Therefore, the chemical and physical properties of GO differ from the properties of graphene. It is possible to functionalize the GO surface with metal or metal oxide nanoparticles which are for useful sensing applications [71]. The presence of different types of functional groups in GO degrades the electrical and mechanical properties and the electrical properties of GO are inferior to the pristine graphene. But these properties can be restored partially by reducing GO surface through thermal or chemical treatments [63, 75]. Thus, the properties of graphene and the derivatives of graphene such as GO and rGO, make them promising nano-filler and sensing materials to produce flexible polymer nanocomposites which will be discussed in the literature review. Among various

metal nanoparticles, AgNPs have been extensively used for various applications such as optical sensors, health care, drug delivery, medical device coating, and so on mainly due to low cost, non-toxicity, biocompatibility, high electrical conductivity, and thermal properties [76--78]. These metal and metal oxide nanoparticles have been integrated into different polymers for fabricating stretchable and wearable strain sensors which will be discussed in the literature review.

1.4 Literature review

In the last decade, numerous research efforts have been carried out and several researchers reported the fabrication and application of flexible, stretchable, and wearable sensors for strain sensing applications.

Table 1.3 Summary of performance characteristics of PDMS-Nanomaterial-based resistive type wearable strain sensors.

Sensor System (year of publications)	Stretchability %	Gauge Factor/ Sensitivity	Linearity	Application	References
rGO/PDMS 2017	-	-	Nonlinear	Measuring the bending angle of the wrist	[79]
rGO/PDMS 2018	-	50.9 kPa ⁻¹	-	E-Skin for wrist pulse detection	[80]
rGO/PDMS 2015	100	-	Linear	Robot movement	[5]
N-Doped rGO/PDMS 2019	1.5	-	Nonlinear	Bending of wrist, neck, and eye-blinking	[81]
rGO/PDMS 2019	350	18.5-88443	Partly linear	Human motion detection	[82]
CNT/PDMS 2015	100	2*104	Nonlinear	Motion of joints	[83]
MWCNT/GNPs/PDMS 2013	40	100	Partly linear	Human Health monitoring	[84]
MWCNTs/PDMS 2014	45	1.2	Nonlinear	Biomedical testing	[85]
CNTs/CBs/Si rubber/PDMS 2017	120	1.25	Linear	Human activity monitoring	[86]
CNT/PDMS 2018	100	2.21	Partly linear	Wearable strain sensor	[87]
CNT/PDMS 2017	20	1140	Linear	Human body movements	[88]
Ag NPs/PDMS 2014	20	4.7-12.5	Partly linear	Human motion detection	[89]
Ag NPs/PDMS 2017	0.81-7.26	547.8		Motion of fingers	[90]
Ag NPs/CNTs/PDMS 2014	2.4	95		Human- machine interface	[91]

In the literature review, only resistive type flexible, stretchable and wearable strain sensors will be discussed which are related to the work that will be presented in the thesis. The flexible sensors in this literature review are based on PDMS, and nanomaterials such as AgNPs, and carbon-based nanomaterials which include graphene, rGO, and CNTs. Some of the PDMS-based resistive type flexible and wearable strain sensors and their performance characteristics which were reported in the past few years are mentioned in Table 1.3. Some of the recent and significant reported pieces of literature are discussed in the following section.

Y. Tang. et al reported an ultrasensitive strain sensor that was stretchable based on rGO microtube/PDMS [92]. The sensor showed excellent sensitivity (GF = 630 under 21.3% applied strain), durability and the sensor showed potential to detect human movement under large strain. S. Wu et al demonstrated a graphene aerogel (GA) and PDMS-based strain sensor and the strain sensor which exhibited high sensitivity (GF = 61.3) [93]. PEI-rGO/PDMS composite thin film-based high sensitive wearable sensor was reported by X. Ye et al. The strain sensor showed high sensitivity (GF = 754), strain range up to 50%, the fast response time (0.6 sec), and durability [94]. F. Han et al reported a strain sensor fabricated by using rGO and Ni NPs coated PU sponge encapsulated by PDMS.

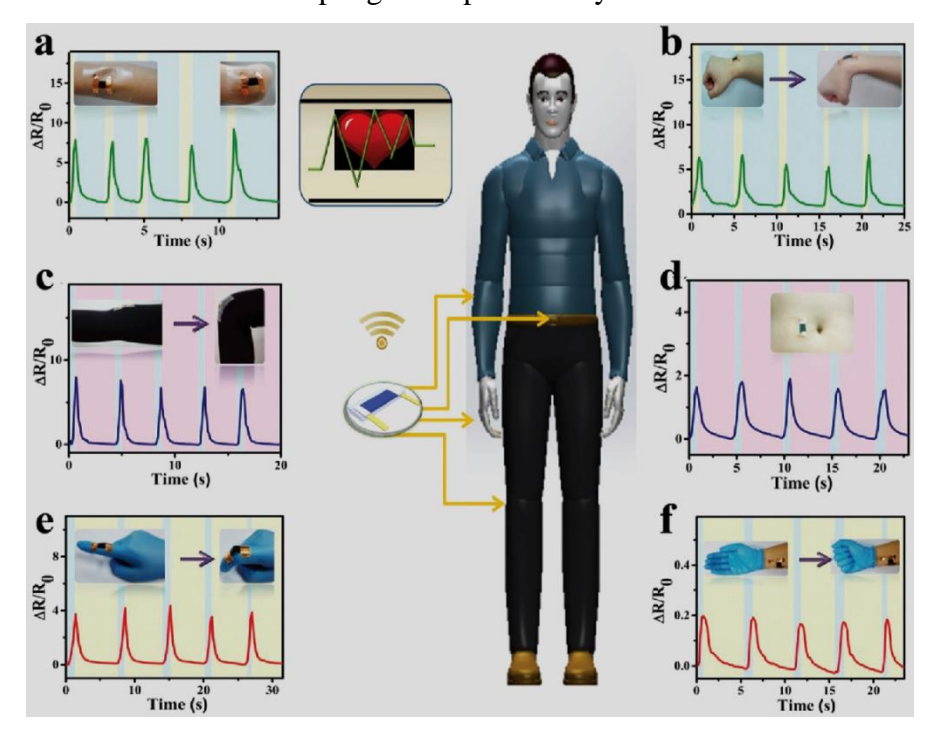


Fig. 1.4 Demonstration of various human motion detection experiments by using the rGO/PDMS sensors such as the response of the sensor to the strain applied by the cycle motion of joints of (a) elbow, (b) wrist, (c) knee, (d) abdomen, (e) finger, and (f) human palm [96].

The sensor was highly stretchable which exhibited a strain range up to 65% and highly sensitive (gauge factor of up to 3360), and also showed fast response time (<100 ms). The sensor was able to detect bodily motions including bending of fingers and facial muscle tension [30]. A flexible strain sensor based on PDMS-GE/PDMS/PDMS sandwich structure was reported by X. M. Zhang et al. The GE/PDMS composites showed excellent conductivity (resistance 9.4 Ω) with 25 wt% GE loading and the strain sensor was tested for the detection of weak human motion, for example, bending of fingers [95]. G. Li et al proposed a simple method to prepare a uniform 3D conductive network by wrapping rGO nanosheets in aligned TPU fibrous mat and encapsulating the sensing layer by PDMS [96]. The combined advantages of the 3D conductive network of rGO/TPU and stretchable PDMS layer resulted in a wide reversible sensing range from 0%-150%, high sensitivity of 593, good stability, and a fast response time of 160 ms. The sensor was utilized to detect the movement of different parts of the body as shown in Fig. 1.4.

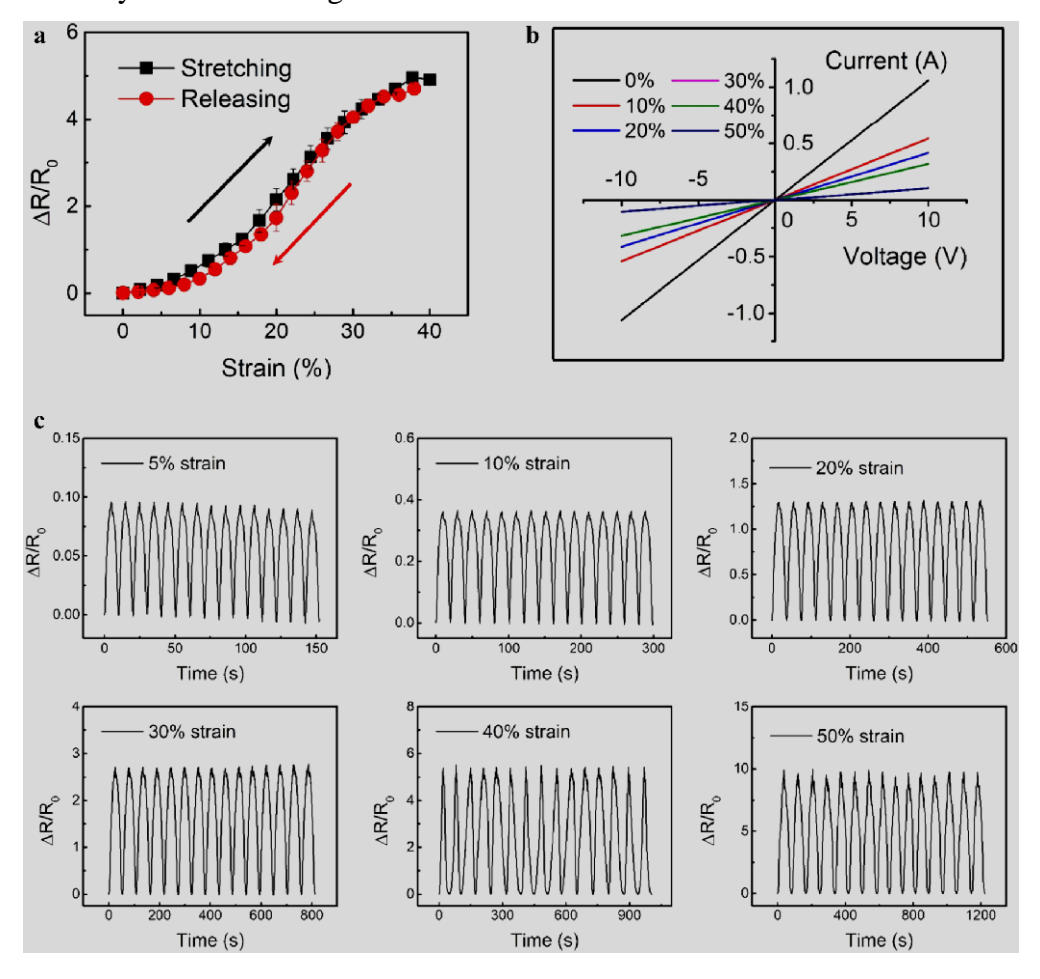


Fig. 1.5 Graphical representation of strain sensing performance of the graphene-coated PDMS sponge based piezoresistive strain sensor which shows (a) the relative change in resistance under 40% applied strain with cycles of stretching and releasing, (b) Current vs voltage characteristics under different applied strain and (c) relative change of resistance over 15 cycles with time and different maximum strains [97].

Graphene-coated three-dimensional microporous PDMS sponge-based piezoresistive wearable sensor structure which was highly elastic was reported by Y. Jung et al. The fabrication of the strain sensor involved a sugar templating process and dip-coating method [97]. The sensor was deformable up to 60% applied strain and showed a sensitivity of 19.21 under the applied strain of 50%. The sensor exhibited high repeatability and low hysteresis as shown in Fig. 1.5. H. Lee et al demonstrated a stretchable and flexible sensor which was fabricated by spray-coating of graphene nanoplatelets on the PDMS substrate and encapsulating the conductive layer by another PDMS substrate [98]. The GF of the sensor was 1.55 under the applied strain of 50% and the strain sensor showed good response and durability which is shown in Fig. 1.6. The strain sensor was able to monitor various human motions.

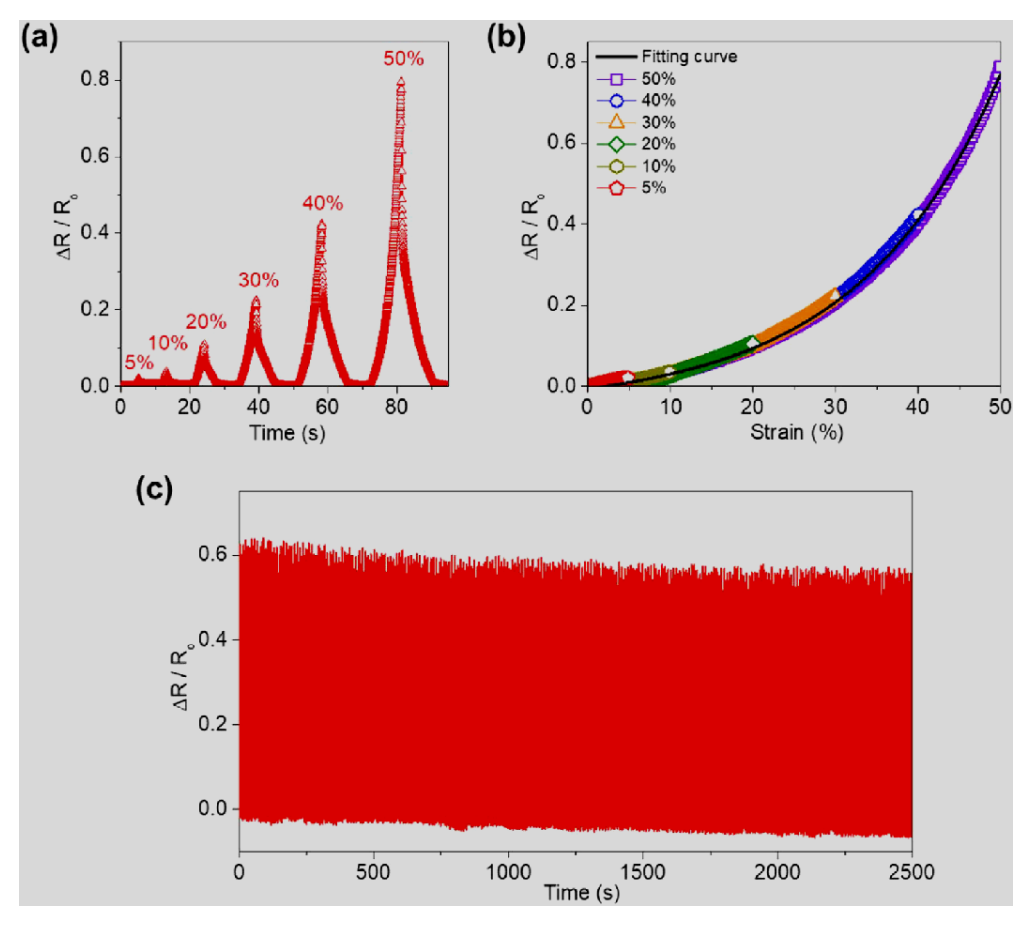


Fig. 1.6 Graphical representation of the electromechanical response of the Graphene/PDMS sensor to the applied strain which represents (a) stretching and releasing test with increasing values of the applied strains of 5, 10, 20, 30, 40, 50%), (b) relative change of resistance w.r.t applied strain and (c) Durability of the sensor under 50% applied strain by stretching and releasing cycles at a rate of 0.5-Hz [98].

Baloda et al. demonstrated a novel fabrication method for a GNP/PDMS-based piezoelectric sensor for human health monitoring and motion detection [99]. The GNP/PDMS mixture (40 wt%) was first prepared and coated over pristine PDMS substrate by a painted brass. The piezo-resistive strain sensor exhibited good strain sensitivity (GF = 62.5), stretchability (65%), stability, reproducibility, and durability (Fig. 1.7). The strain sensor showed good performance used for monitoring human motion and wrist pulse.

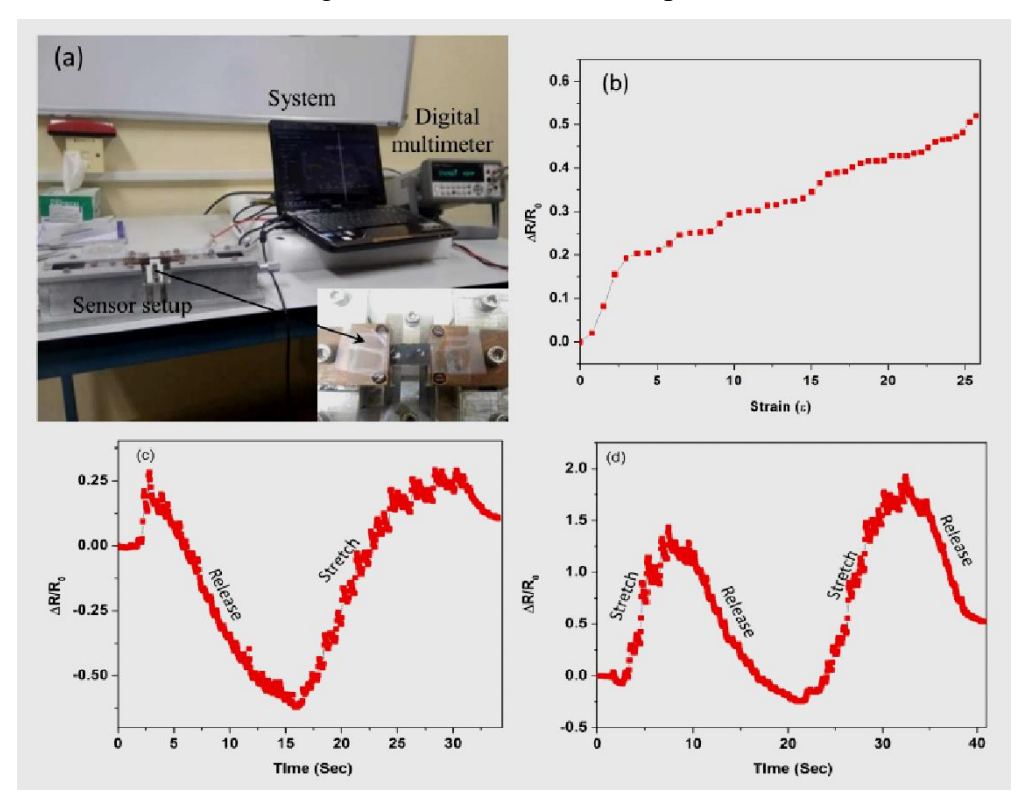


Fig. 1.7 (a) Experimental setup of the strain sensor and (b) graphical representation of relative resistance vs strain and (c, d) the sensor exhibiting a significant change in resistance upon stretching and releasing with time [99].

A stretchable and robust strain sensor was demonstrated by Z. Su et al. A novel method was utilized for the fabrication of the strain sensor with self-assembly of MWCNT and PS microsphere composites. The MWCNT-PS/PDMS composite exhibited a gauge factor of 1.35 and strain range up to 100% [100]. Y. Jung et al demonstrated the fabrication of a CNT/PDMS-based piezoresistive pressure sensor by using a simple cost-effective sugar templating process [101]. The pressure sensor showed linear sensitivity (0.015 kPa⁻¹), excellent repeatability, linearity (0.991 at 50 kPa) hysteresis, and reliability to detect human motions. Y. Gao et al reported a novel method used for developing high-performance stretchable electromechanical sensors using fragmentized CNT/PDMS-based composites where the composite was grounded into fragments which were followed by densification [102]. The fragmentized CNT/PDMS composites showed high sensitivity (GF >200) with a

wide range of applied strain (up to 80%) which is attributed to sliding of the individual fragment particles of CNT/PDMS-based composites during the application of mechanical strain as shown in Fig. 1.8. The CNT/PDMS sensor was tested for the detection of various movements of the human body, breathing, and wrist pulse.

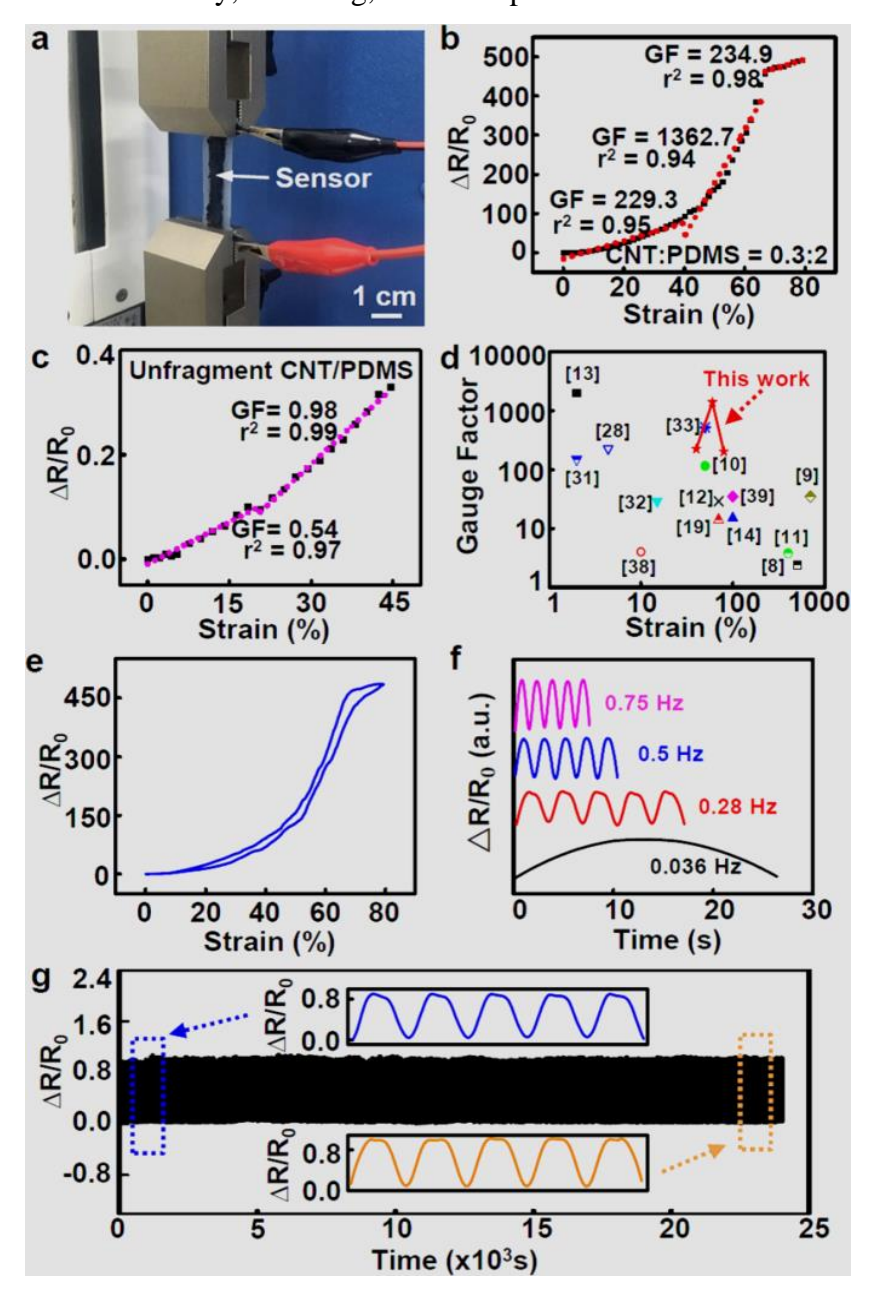


Fig. 1.8 (a) Image of the experimental setup for testing of the sensor. Graphical representation of (b) the relative change in resistance vs strain (fragmentized CNT/PDMS composite). (c) the relative change in resistance vs strain curve (un-fragmented CNT/PDMS composite) (d) GF as a function of a maximum strain of recently reported resistive-type strain sensors, (e) hysteresis curve of the sensor at 80% strain, (f) frequency response of the sensor at ~10% strain, and (g) the relative change in resistance vs strain of the sensor for more than 10 000 cyclic tension tests [102].

S. Wang et al reported a cost-effective and simple technique for the fabrication of a high-performance sensor which was based on crack formation in the multilayer CNT/PDMS composite [103].

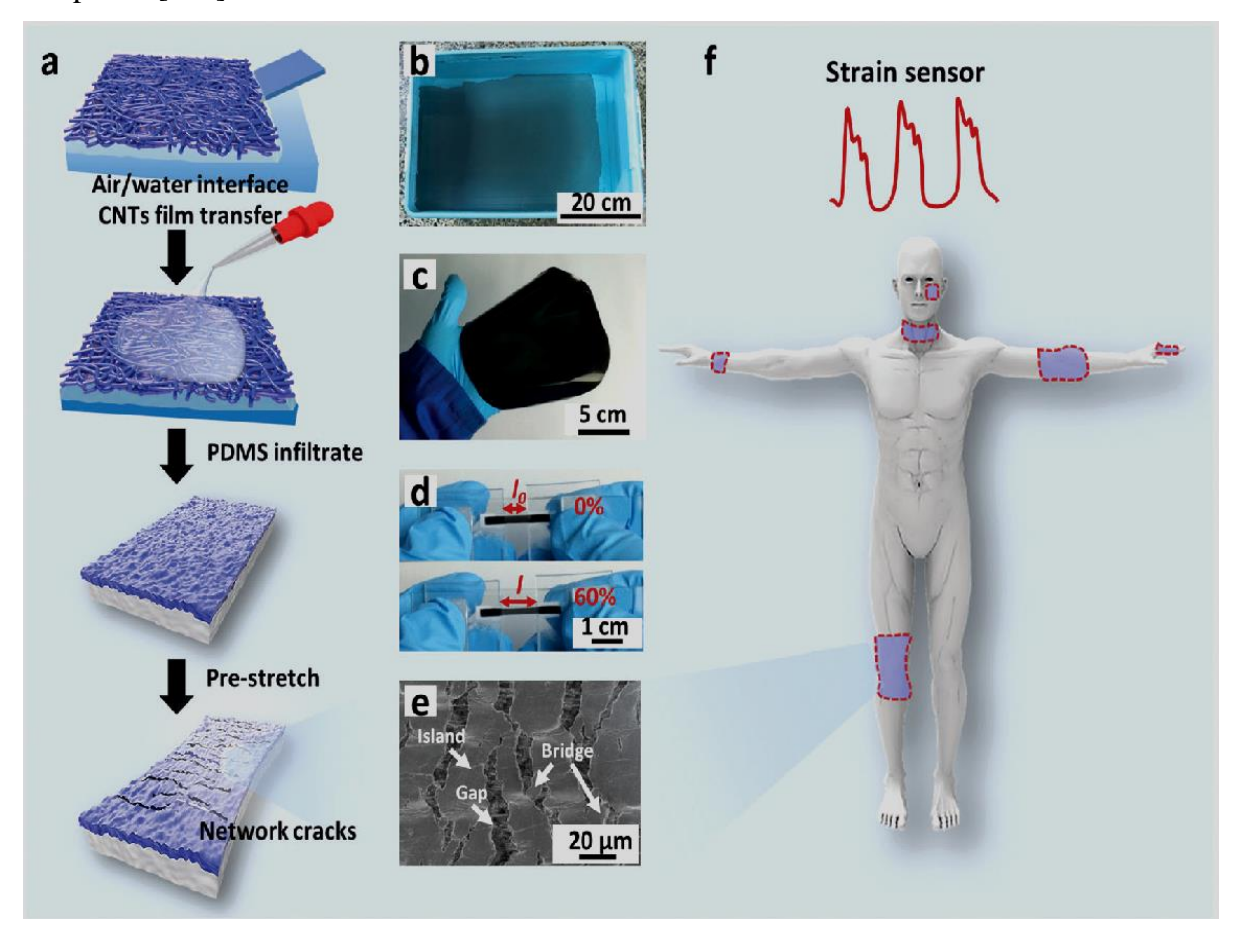


Fig. 1.9 Representation of the fabrication process of CNT films/PDMS sensors which include (a) step-wise illustration of the fabrication process of CNT films/PDMS composite and formation of cracks by pre-stretching, (c) CNT/PDMS sensor after dilution of PDMS solution, infiltration and curing, (d) photograph of the CNT/PDMS composite cut sample which was attached on a homemade fixing device, (e) morphology of the SEM image showing the network of cracks after pre-stretching, and (f) representation of the sensor that was used in different human body parts for human motion detection [103].

The formation of the network crack in the CNT/PDMS composite was tuned by controlling the microscopic thickness of the multilayer CNTs which amplified the GF and sensing range of the CNT/PDMS-based strain sensor as shown in Fig 1.9. The network crack resulted in high sensitivity (GF = 87) under small and high strain (0.007% and 100%) and excellent stability as shown in Fig. 1.10. The sensor was able to detect signals of artery pulse, touch, bending of fingers, wrists and music vibration, etc.

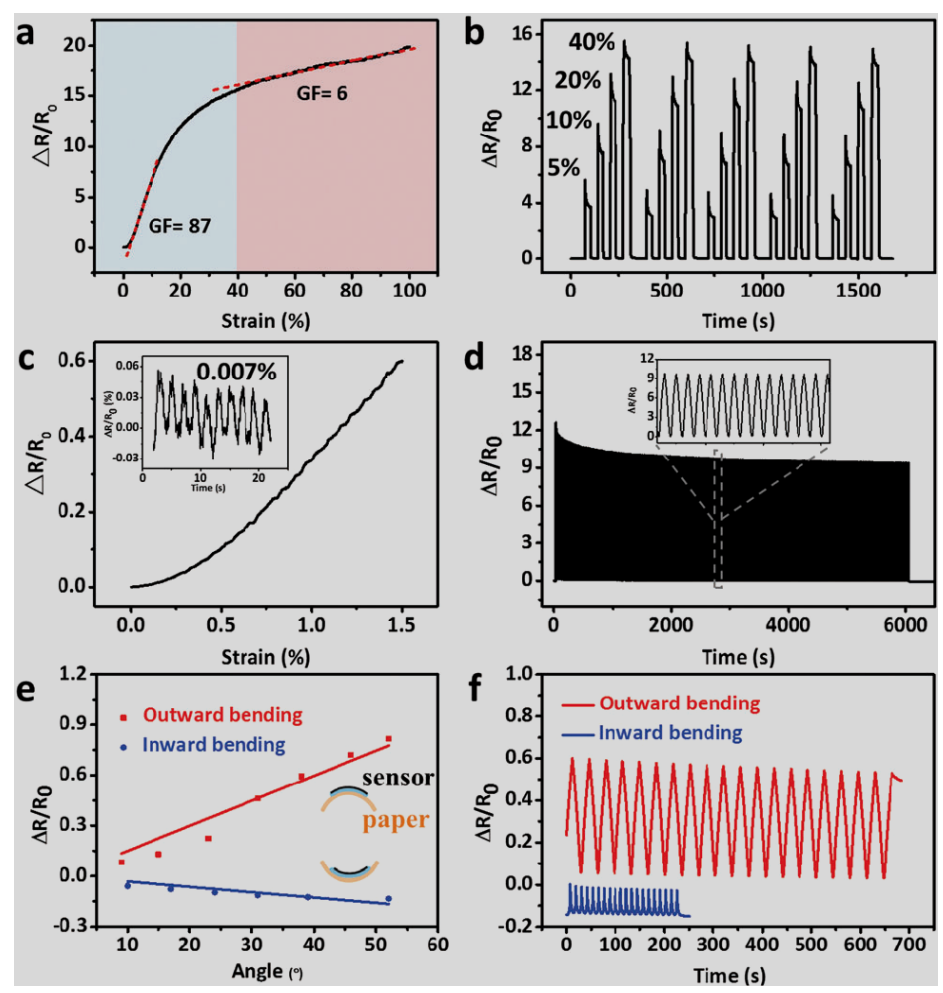


Fig. 1.10 Graphical representation of electromechanical characteristics of the CNT/PDMS-based sensors which illustrate (a) relative resistance change vs strain curves of CNT/PDMS-based sensors (15 layers), which shows two-stage GF behaviors, (b) relative resistance under different applied strains of 5, 10, 20, and 40% for five different cycles, (c) relative resistance vs strain curves in a small region of 1.5% strain, (d) relative resistance change of the sensor during repeated stretching and releasing cycles (1500 cycles) under 20% of applied strain, a relative change in resistance (e) under the bending deformation, and (f) during cyclic inward as well as outward bending tests [103].

K. Park et al. developed an MWCNT/PDMS-based flexible sensor by mixing MWCNTs (1 to 10 wt%) and PDMS by shear mixing and ultrasonication for medical applications such as a tactile sensor for a robotic hand. The sensor had shown sensitivity to mechanical strain 40-50% [104]. Q. Li et al presented a strain sensor that was CNT/PDMS sponge-based where porosity was introduced into the nanocomposite by adding citric acid monohydrate [105]. Due to the porosity, the GF of the CNT/PDMS sensor (GF = 15, when strain > 15%) was better than the sensor with a non-porous structure as shown in Fig. 1.11. The sensor was able to detect human body motions and activities such as drinking, breathing, and speaking.

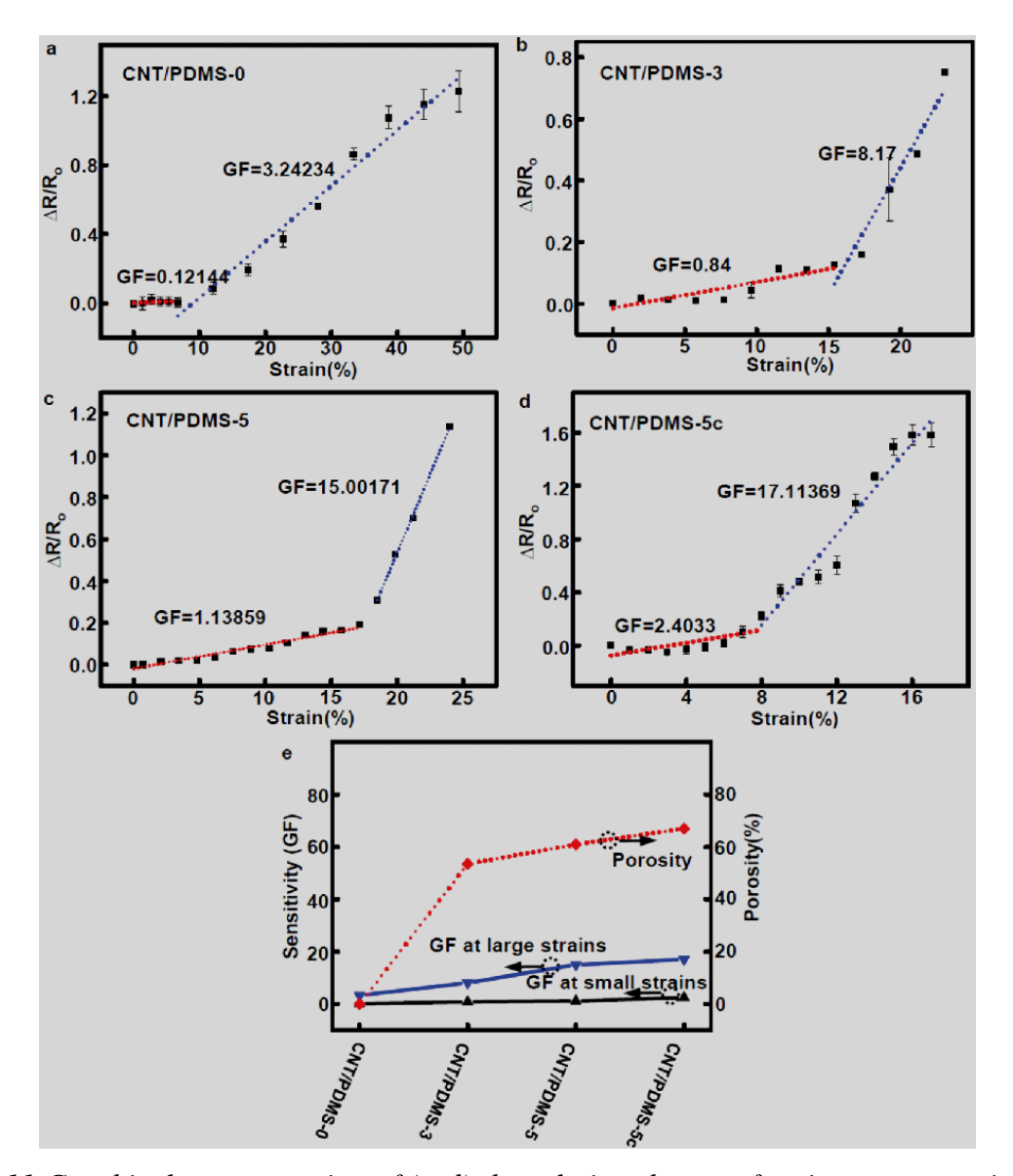


Fig. 1.11 Graphical representation of (a-d) the relative change of resistance vs strain of the strain sensors which is based on CNT/PDMS sponges, and (e) sensitivity vs porosity plots of different CNT/PDMS-based sponges [105].

J. H. Kim et al demonstrated a method that was cost-effective, fast, and simple to fabricate homogeneously hybridized CNT/PDMS polymer composites with excellent conductivity for flexible and wearable electronics applications [106]. It was observed that the CNTs were entangled due to the van der Waals forces. Therefore, non-covalent functionalization is a promising way to obtain a homogeneous dispersion. It has been reported that CNT/PDMS composites had shown high conductivity (sheet resistance $< 20\Omega sq$), high tensile stress (\sim 3.65 MPa), high flexibility, good strain sensitivity, and stability by utilizing isopropanol as a solvent for the non-covalent functionalization of CNTs with methyl group terminated PDMSas shown in Fig. 1.12. The fabricated sensor had shown potential for flexible strain sensing and wearable electronics applications such as ECG material for healthcare.

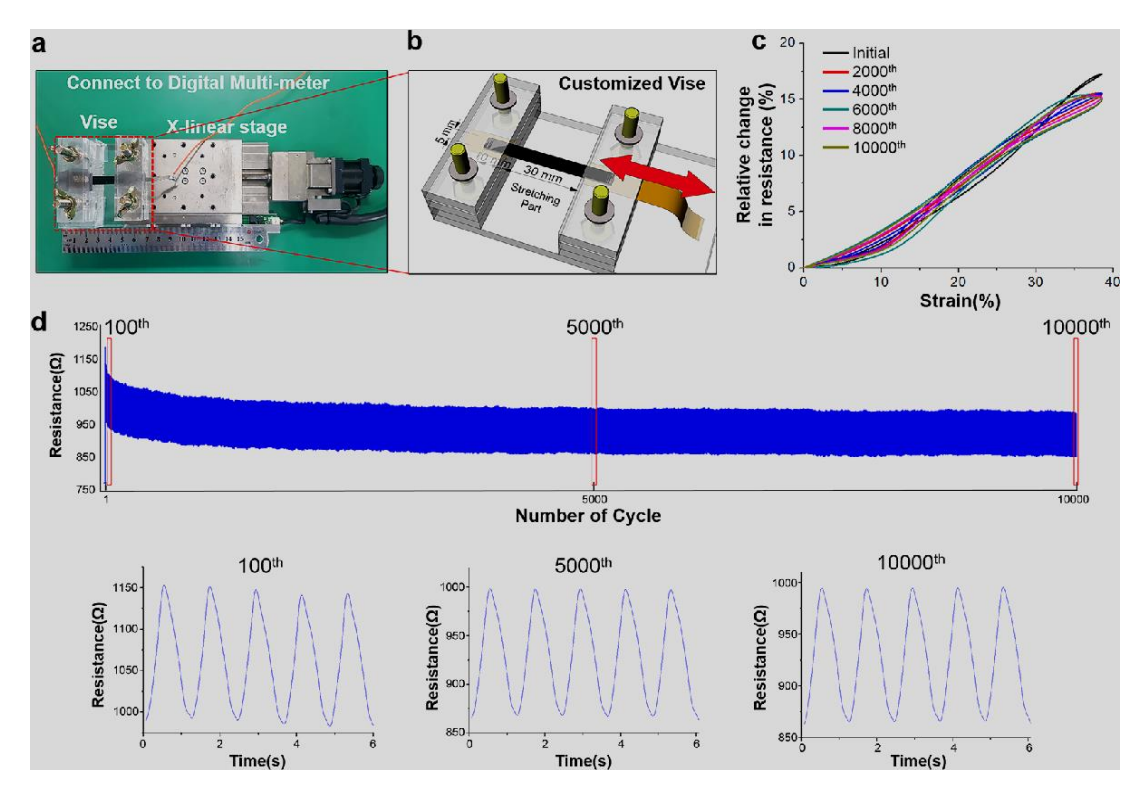


Fig.1.12 Image of the (a) experimental set-up, and (b) schematic representation of the customized vise. Graphical representation of (c) relative change in resistance in every 2000th cycles from the test that was carried out for 10,000 cycles by utilizing CNT/PDMS (4wt%), (d) resistance change during the test that was carried out for 10,000 number cycles by utilizing CNT/PDMS (4wt%), and (e) resistance vs time for five different cycles including 100th, 5000th, and 10000th [106].

T. Li, J. Li, and A. Zhong et al demonstrated a flexible strain sensor which was based on MWCNTs/PDMS microspheres/PDMS fabricated by a unique oil-in-water Pickering emulsion method [107]. The sensing material MWCNTs/PDMS microspheres were coated with PDMS and the flexible sensor exhibited high conductivity of (resistance of 157.64 Ω .cm), more than 40% strain range, good stability and sensitivity (GF=7.22). The strain sensor was capable of detecting the movements of different human body parts such as bending of the knee joints, wrist, and elbow. The fabrication of a flexible resistive-based strain sensor which was composed of a porous structured CB/MWCNT layer deposited on the top of porous PDMS substrate was reported by P. Zhang et al. The synergistic contribution of the conductive network formed by CB/MWCNT and porous PDMS structure improved the sensitivity (GF = 61.82), strain range (130%) along and the CB-MWCNT/PDMS strain sensor showed good linearity and high stability [108]. The porous CB-MWCNT/PDMS strain sensor was capable of detecting movements of different joints of the human body as shown in Fig. 1.13. J. Du et al investigated the electrical, mechanical, and electromechanical properties of CNTs/PDMS composites and found that CNTs/PDMS-based flexible composite with 8

wt% of CNTs exhibits a comparable sensitivity (GF = 1.21) under strain range of 0%-40% [109].

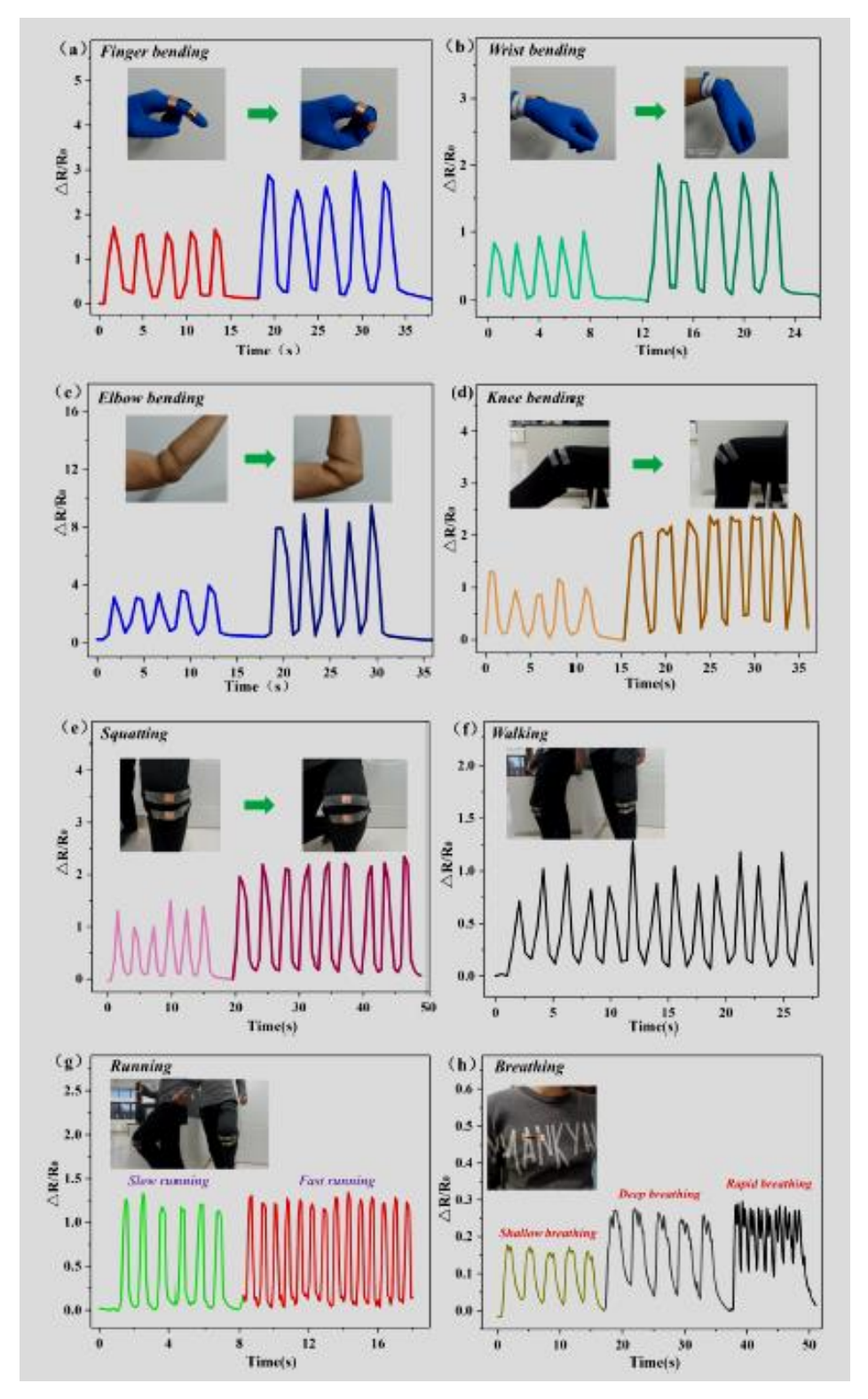


Fig. 1.13 Graphical representation of the tests which were performed to monitor different human motions by utilizing the fabricated sensors such as bending of (a) finger (b) wrist (c) elbow, (d) knee, (e) squatting, (f) walking, (g) running, and (h) the responses to breathing [108].

H. M. Soe et al reported a resistive strain sensor that was based on AgNPs encapsulated by PDMS substrate (Ag-PDMS) and Ag NPs modified PDMS composites (Ag-PDMS) [110]. The GF of the Ag_PDMS-based sensor was 8.46-10.44 under the applied strain of 70% and the GF of the Ag-PDMS-based sensor under the applied strain of 70% was 12.76-25.74. The strain sensor was tested for the detection of various human movements. The fabrication of a hybrid material-based strain sensor was proposed by I. Kim et al where Ag flakes/Ag nanocrystals (NCs) were incorporated into the bulk of PDMS elastomer as shown in Fig. 1.14.

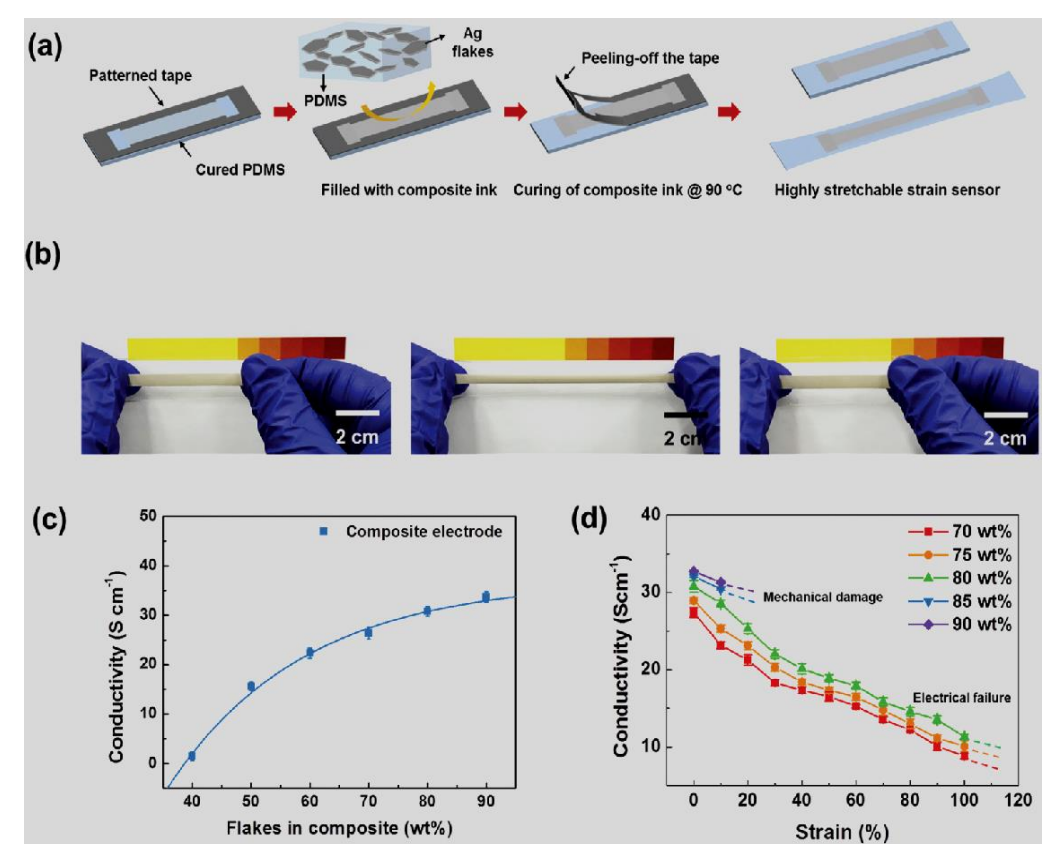


Fig. 1.14 (a) Schematically represented the fabrication process of the conductive composite based on Ag flake and PDMS, (b) optical images of the fabricated composite when it was stretched and released by applying 100% strain, (c) conductivity of the composites which varied with the wt% of Ag flakes, and (d) change in electrical conductivity of the composites with different wt% such as 70, 75, 80, 85, and 90 of Ag flakes under the applied strain range from 0 to 100% [111].

The incorporation of the Ag flakes enhanced the conductivity of the strain sensor and during stretching the Ag flakes maintained a conductive network and at the same time the contact resistance between the Ag flakes was reduced by the Ag NCs reduced [111]. The hybrid Ag/PDMS-based strain sensor demonstrated high sensitivity (GF = 7.1), strain up to 50%, good stability, and the sensor was applied to detect finger motion and human muscle strength as shown in Fig. 1.15.

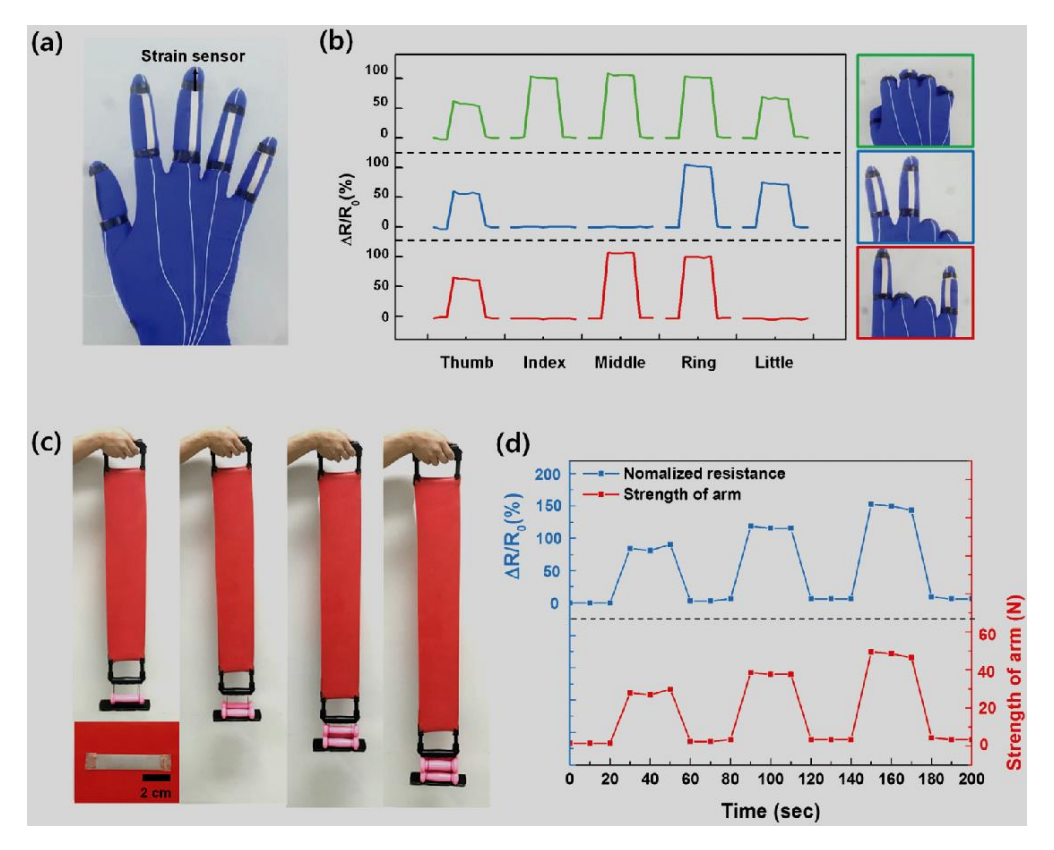


Fig. 1.15 (a) Image of the smart glove where the sensors were attached, (b) relative change of resistance in the smart glove for various gestures of the finger, (c) image of the band illustrating the monitoring of the sports performance when forces were applied by using dumbbell of 1 to 4 kg weight, and (d) relative resistance which changed with time during the monitoring of the sports performance (stretching and releasing) by using the arms [111].

Ag/PDMS composite-based flexible and wearable strain with sensing abilities of force and strain was reported by H. Li et al. A simple fabrication method was adopted which involves physical grinding of Ag NPs and mixing with liquid PDMS as shown in Fig. 1.16.

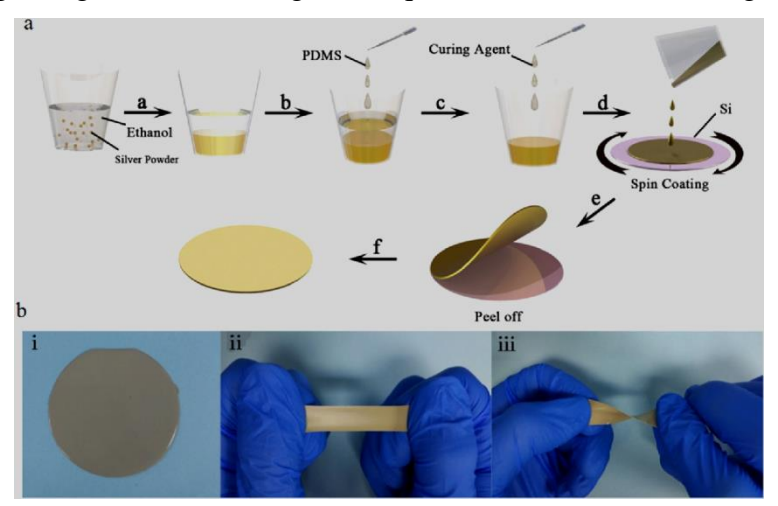


Fig. 1.16 (a) Schematic representation of the fabrication process of the sensors that are based on Ag Nanoparticles and PDMS and (b) image of the strain sensor which exhibited excellent flexibility when stretched and twisted [112].

Different wt% of Ag NPs was used and the strain sensors showed high sensitivity when different strains were applied as shown in Fig. 1.17. The Ag/PDMS-based strain sensor exhibited highest sensitivity (GF = 939) under 36% strain and detection of force as low as 0.02N for 175 wt% AgNPs [112]. The strain sensor also demonstrated multidimensional sensing abilities from sound detection to monitoring human body dynamics.

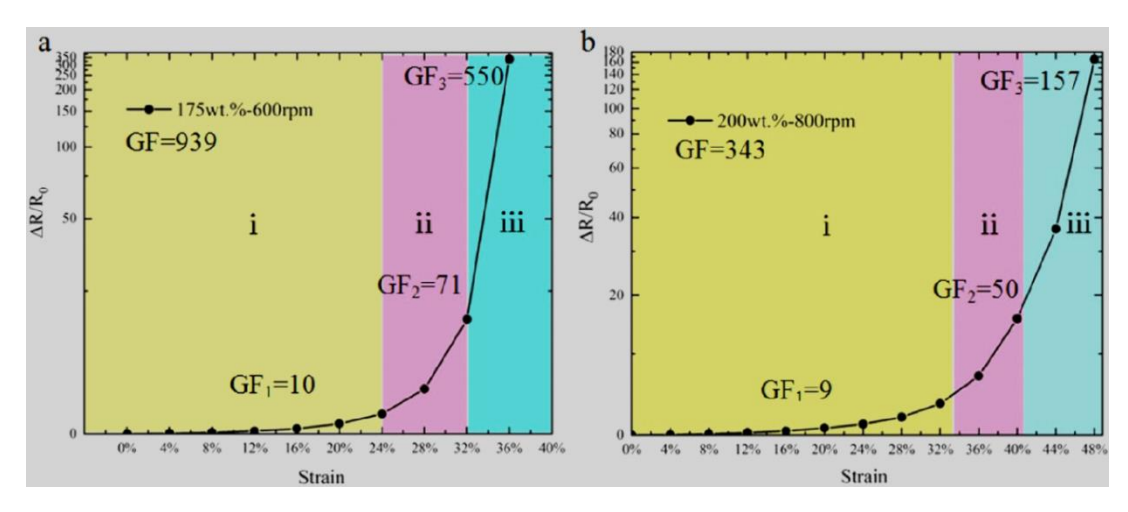


Fig. 1.17 Graphical representation of the different rate of change of strain vs resistance, (a) 175 wt% at 600 rpm, (b) 200 wt% at 800 rpm, and the respective GF [112].

X. Zhao et al. demonstrated a flexible pressure-sensitive sensor by incorporating AgNPs decorated rGO nanocomposite into the sponge of PDMS elastomer [113]. The nanocomposite was synthesized by using GO, AgNO₃ as a precursor, and hydrazine hydrate as a reducing agent. The AgNPs coated on the rGO surface enhanced the electrical conductivity of the AgrGO/PDMS composite sponge through the transfer of electrons from AgNPs to the rGO sheets as shown in Fig. 1.18. The Ag-rGO/PDMS composite exhibited the highest pressure sensitivity of 8.86 KPa⁻¹ which is useful for all types of mechanical forces such as pressure, stretching, bending, and twisting as shown in Fig. 1.19

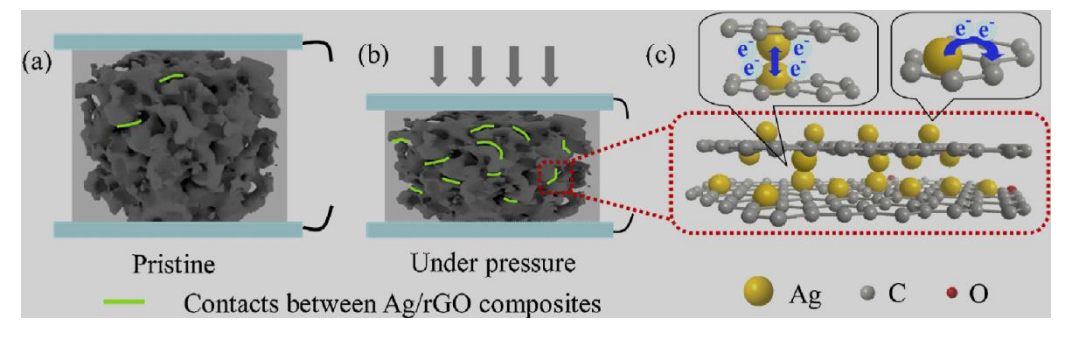


Fig. 1.18 Schematic representation of the mechanism of sensing by the Ag-rGO/PDMS-based composite sponge which illustrates the (a) pristine, (b) under pressure, (c) the contacts between the Ag-rGO composites (enlarged version) which depicts the transfer of electrons from AgNPs to rGO sheets and also between the Ag NPs [113].

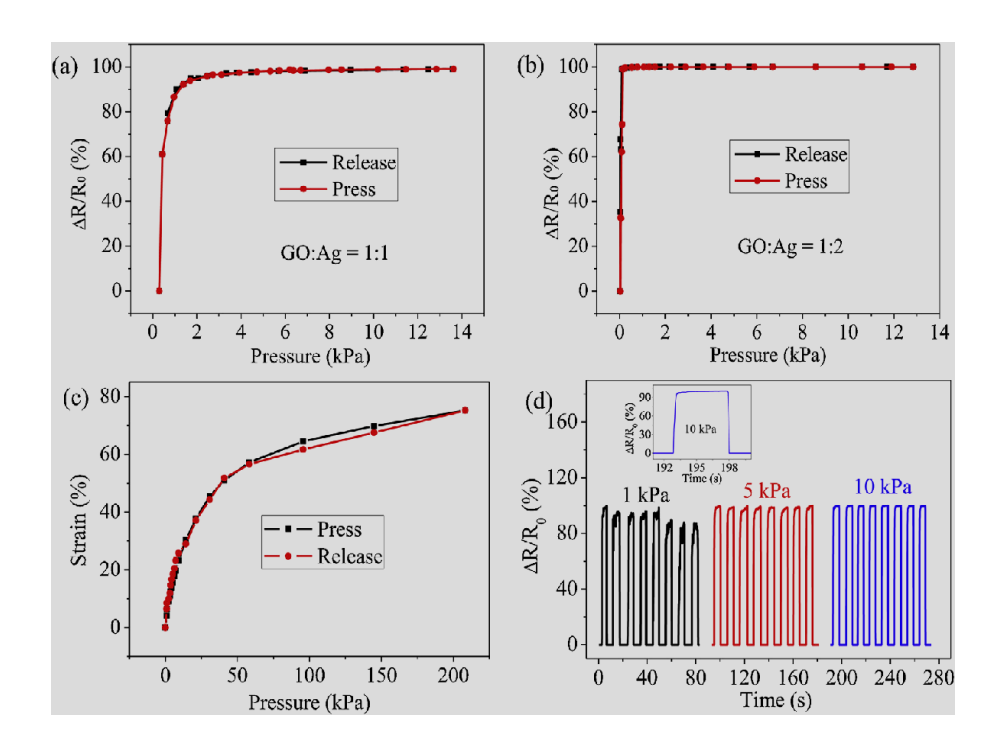


Fig. 1.19 Graphical representation of the hysteresis behavior of the Ag-rGO/PDMS composite corresponding to the weight ratio of (GO: Ag) (a) 1:1 and (b) 1:2 respectively, (c) pressure vs strain plot of PDMS composite-based sponge and (d) relative resistance vs time for dynamic pressure corresponding to the range of pressures [113].

AgNPs/rGO/PDMS-based flexible sensor was fabricated by L. Zhang et al. The sensor was fabricated by adopting a very simple and low-cost method where PDMS elastomer was used as the substrate to construct a sandwiched structure as shown in Fig. 1.20.

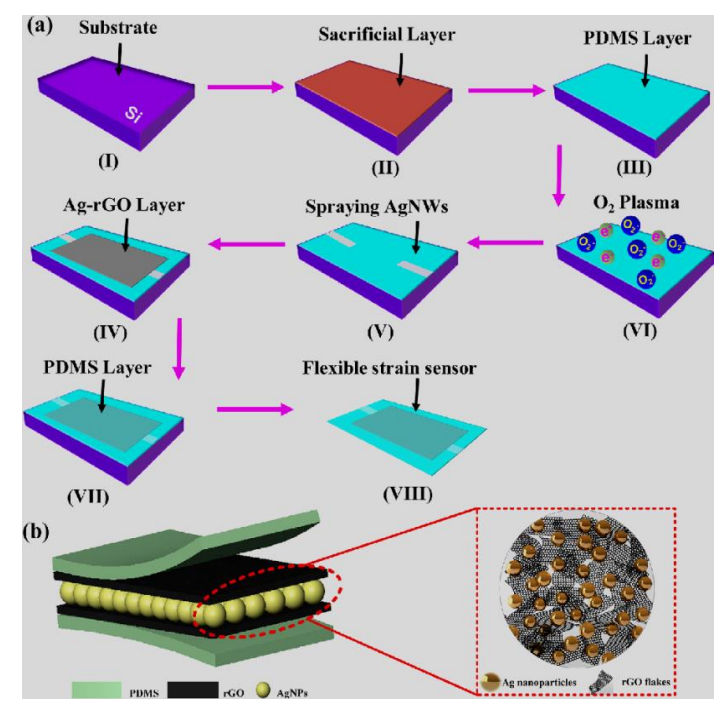


Fig. 1.20 (a) Schematic representation which depicts the step-wise fabrication process of AgrGO strain sensors, and (b) cross-sectional representation of the sensor[114].

The Ag NPs acted as the connecting point to the rGO layer and improves the conductivity of rGO in the conductive 3D structure [114]. Hence, the strain sensor exhibited an excellent range of sensitivity under the low and high strain range (GF = 7.2 to 429 under the applied strain of 0.2% to 200%) as shown in Fig. 1.21. Therefore, the wearable sensor was efficient for monitoring human motion and activities in real-time such as breathing, speaking, facial expressions, and wrist pulse.

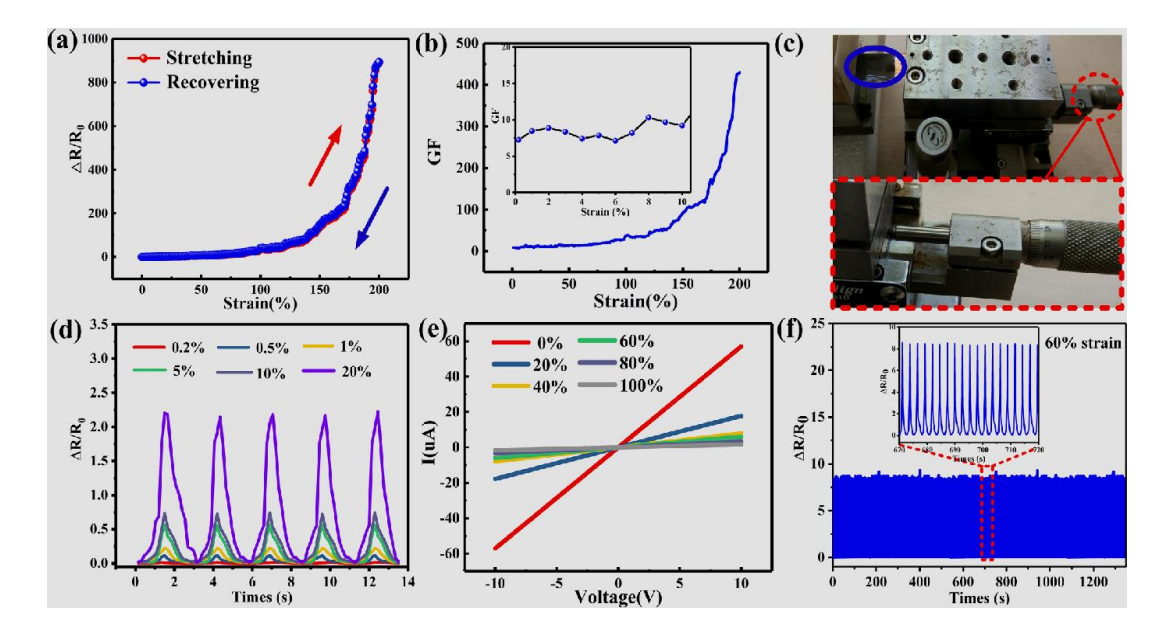


Fig. 1.21 Graphical illustration of the (a) relative resistance variation of the sensor for cycle 1, (b) sensitivity (GF) for 0-200% of strain applied, (c) a homemade jig controlling the strain of the sensor, (d) relative resistance variation when the sensor was stretched by applying different strain, (e) current vs voltage characteristics for different strain, and (f) relative resistance when the sensor was subjected to 60% of repeated strain for 500 cycles [114].

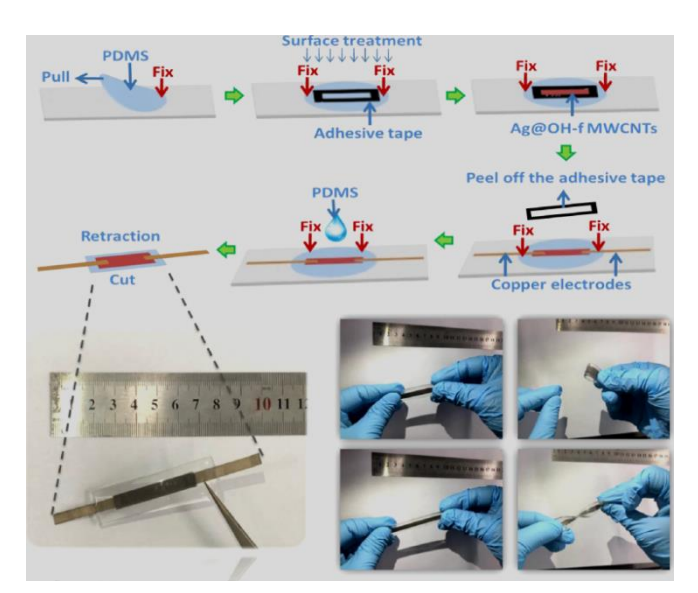


Fig. 1.22 Schematic representation of the fabrication process of the strain sensor [115]

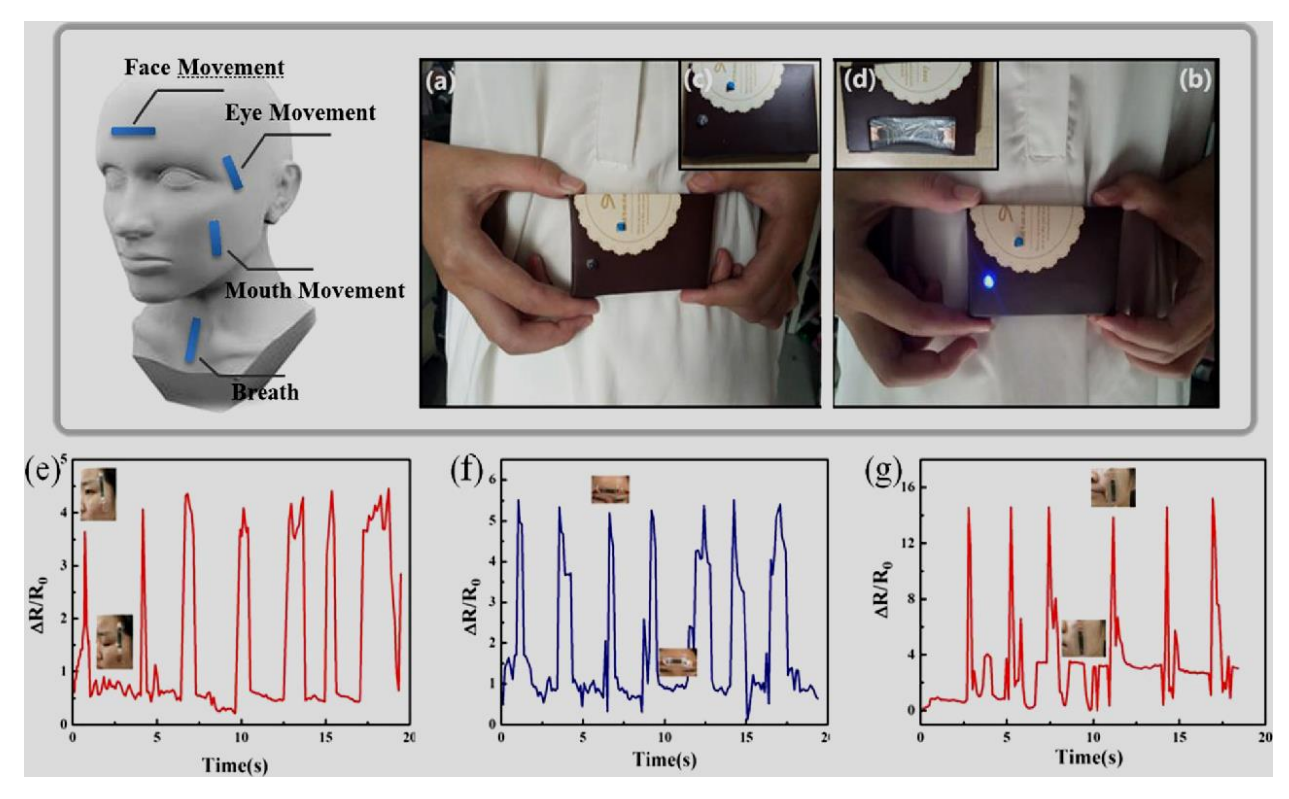


Fig. 1.23 Picture of the different tests that were conducted by using the Ag_OH-f-MWCNT-based portable breathing detector with wrinkled structure (a) breathing in and (b) breathing out. Graphical representation of relative resistance with time which illustrated the expression recognition for (e) facial, (f) frown, and (g) smile respectively [115].

A novel Ag_OH-fMWCNT/PDMS-based sensor to monitor soft-strain was fabricated by Z. Yuan et al as shown in Fig. 1.22. The stretching and depositing method was adopted to fabricate wrinkled and sandwich structures which improved the sensitivity (GF = 412.32) and strain range (42%) [115]. The Ag_OH-f MWCNT/PDMS-based sensor was lightweight, wearable, flexible, and was able to detect breathing, facial, and hand movement as shown in Fig. 1.23. Y. Yang et al reported a flexible Ag/CNTs/PDMS composite film sensor where CNTs film was transferred to a pre-stretched PDMS substrate and upon releasing the substrate to create wrinkled structure in the CNTs film [116]. The Ag film which acts as a sensitive transducer was deposited on the CNTs film. The wrinkled structure of the CNTs film resulted in high sensitivity (GF = 30) and a larger strain range (50%). B. Liu et al reported a very simple process for the fabrication of AgNPs/CNT/PDMS-based composites for electrocardiograph (ECG) measurements by incorporating 11 wt% and 12 wt% of CNTs and Ag nanoparticles in the PDMS matrix as shown in Fig 1.21 [117]. The composites were utilized for fabricating the two-dimensional electrodes for ECG measurements as shown in Fig 1.24. The polymer electrodes had proven to be a potential material for long-term ECG measurements after being used for 14 days of continuous ECG monitoring.

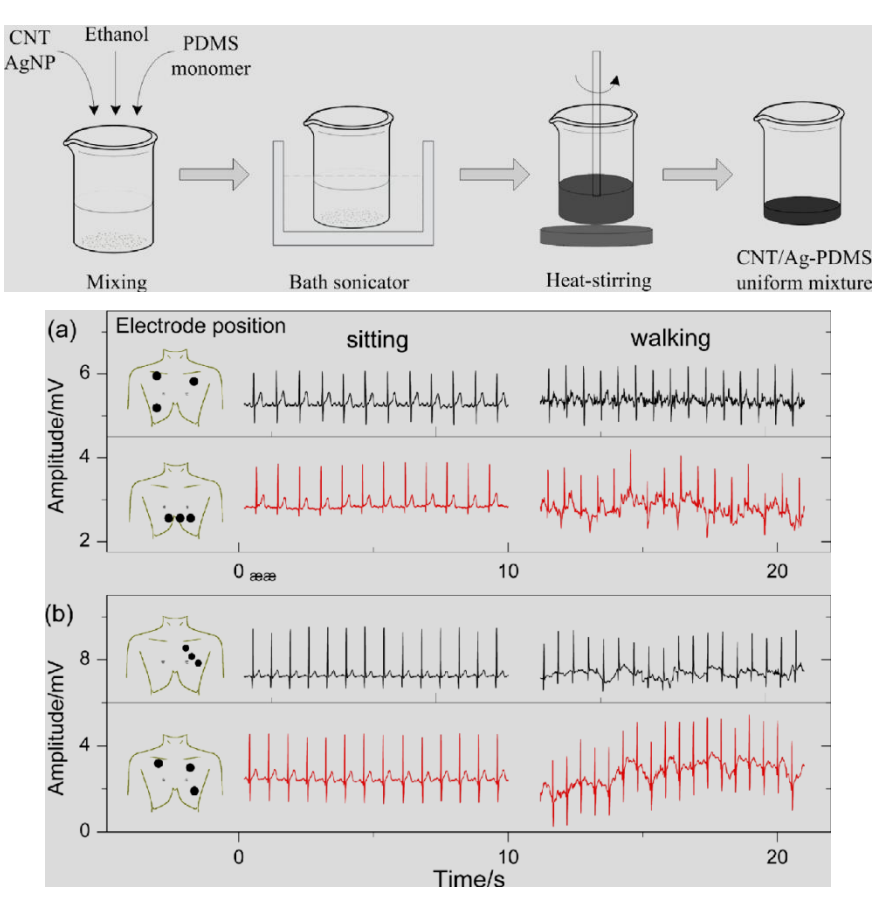


Fig. 1.24 Schematic of the process utilized for fabricating the conductive composite and testing of the wearable sensor in different places of the body, and with different persons such as (a) female, and (b) male respectively[117].

1.5 Current challenges

With the advancement of material science and electronics, the strain sensors which are flexible/stretchable, and wearable have shown promising performances for applications in soft robotics, sports performance monitoring, health monitoring, flexible devices for wearable communications, stretchable energy storage, and harvesting devices, etc. [4]. Still, there are several challenges associated with the fabrication and application of flexible/stretchable and wearable strain sensors such as cost of production, biocompatibility, comfortability, integration, performance, and safety. Also, achieving balanced performance characteristics of a strain sensor such as excellent stretchability (\mathcal{E} %), sensitivity (GF), linearity (\mathcal{R} 2), range of detection (low and high strain), durability, and response time is quite challenging [25].

The low-cost production of conductive nanomaterials and the low-cost fabrication process of the flexible and wearable sensor are most demanding [3]. Most of the processes which have been reported to fabricate strain sensors require costly types of equipment and fabrication of the flexible sensors involves a higher weight percent (wt %) of nanofiller materials.

Moreover, the fabrication processes are complex and the sensing material shows very poor electrical conductivity and sensitivity at lower wt%. Therefore, a simple, cost-effective process and lower wt% of nanomaterials which are very the requirements for the fabrication of high-performance wearable and flexible strain sensors are still needed to be investigated.

The wearable sensors come with direct contact with the human body during usage and hence comfortability, compactness, and biocompatibility are the much-needed requirements. The flexible and stretchable polymer materials used for the wearable strain sensor must fulfill the requirement of biocompatibility and must not prevent blood circulations and must not cause skin irritation, inflammation, and bacterial infections.

The electrical, dielectric, and mechanical properties of the polymer-nanomaterial composites directly depend on the proper distribution of the nano-filler materials inside the polymer matrix. Also, the interaction that occurs between the nano-filler and polymer chain and also filler-filler interactions play a major role to attain desired dielectric or electrical properties. The nano-fillers such as graphene and their derivatives are known to be agglomerated in the polymer matrix. The CNTs also tangle with each other in the polymer matrix. The agglomeration or restacking occurs in the polymer matrix due to the π - π interaction and van der Waals force of attraction. Functionalization of the GO, rGO, and CNTs by using different approaches can overcome the agglomeration process. However, functionalization also degrades the physical and chemical properties of the nano-fillers. Therefore, a proper functionalization process needs to be investigated without degrading the electrical properties and flexibility of the smart composite materials. PDMS is a flexible elastomer but it is hydrophobic and it does not dissolve in most of the polar and organic solvents due to its high chemical resistance. Hence, the distribution of the nano-fillers in the PDMS elastomer is a crucial issue.

By summarizing all the aspects, we have realized that achieving excellent dielectric and electrical properties of the polymer-based nanocomposites with a very low nano-filler wt% is a major challenge. The polymer retains the mechanical property or elasticity with a low wt% of the filler nanomaterials. But, polymer composites with low wt% possess very low electrical properties. At the same time, with higher loading of nanofillers, the polymer composites possess higher electrical properties. But, polymer composites with higher wt% of nanofillers lose flexibility which is a key factor in developing flexible and wearable sensors. Therefore, simple and cost-effective approaches with lower loading of nanofillers to fabricate strain sensors which are high-performance, flexible/stretchable, and wearable are still needed to be addressed to overcome the current challenges.

1.6 Objective of the thesis

The main objective of this thesis work is the development of PDMS-based smart materials for stretchable/flexible and wearable sensor applications. For this purpose, two approaches have been investigated. The first approach is to develop PDMS-based nanocomposites by incorporating different nanomaterials in the PDMS matrix. The second approach is to fabricate a strain sensor consisting of a hybrid conductive nanomaterials sandwich between two PDMS substrates by using a simple and cost-effective method. The second objective is to study the electrical properties and flexibility of the PDMS-based composite materials containing lower wt% of nanofillers for wearable and flexible sensors. The final objective is to demonstrate the capability of the fabricated smart material for monitoring human motions in real-time.

CHAPTER 2

Synthesis and Characterizations of Nanomaterials

2.1 Introduction

In this chapter, the synthesis and characterization of the different nanomaterials such as GO, rGO, Ag-rGO, Ag-MWCNT, and Ag-SWCNT are presented. The characterizations of the nanomaterials were performed with different analytical instruments to evaluate for composition, morphology, and molecular structure which are also presented in this chapter. Also, the characterizations were utilized to investigate the suitable nanomaterials for producing smart materials which will be utilized for the fabrication of flexible/stretchable and wearable sensors.

2.2 Synthesis of GO, rGO, Ag-rGO, Ag-MWCNT, and Ag-SWCNT nanomaterials

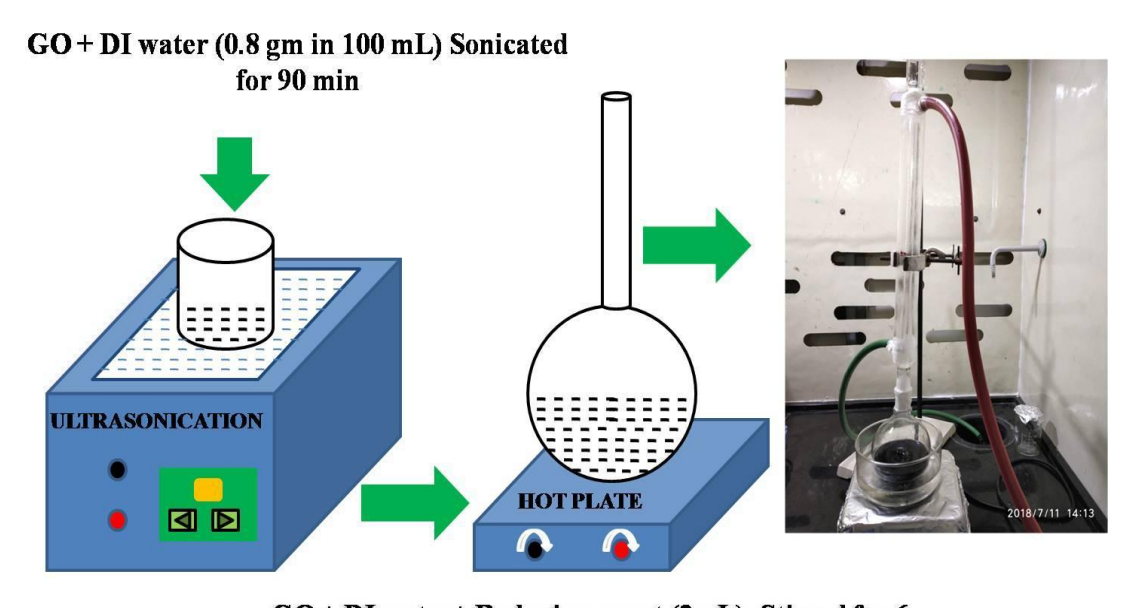
2.2.1 Synthesis of Graphene Oxide (GO) by improved Hummer's method

The synthesis of GO was carried out by using the improved Hummer method [119]. For this purpose first of all graphite powder (3 gm, flake size 45 micron, Sigma Aldrich) was mixed with a 9:1 ratio of H₂SO₄ (Fisher Scientific) and H₃PO₄ (SRL) in a 500 mL glass beaker (Borosil). The solution mixture was then stirred magnetically for proper mixing. Then, 18 gm of KMnO₄ (MERCK) was mixed with the solvent mixture and it was again magnetically stirred for proper mixing of KMnO₄ with other constituents for a few minutes. The abovementioned mixture solution was stirred continuously for 18 hrs at 50 °C. After 18 hours, the temperature of the solution mixture was allowed to come down to room temperature and poured into an ice-cold DI water solution containing 30% H₂O₂. The solution mixture was initially washed with 30 % HCl and further, it was diluted by adding more DI water in a 5L glass beaker to allow the particles to settle down. Once the larger particles were settled down the top transparent solution was thrown away and the remaining solution containing the particles was centrifuged to collect the solid material. After washing repeatedly with DI water the remaining solid material was once again washed by using ethanol solution and finally vacuum dried at 70 °C overnight to obtain the graphite oxide powder. The graphite oxide powder was dispersed in DI water through ultrasonication for proper exfoliation. The solution mixture was again centrifuged and the remaining solid material was dried in a vacuum at 70 °C for six hours to obtain the GO powder.

2.2.2 Synthesis of rGO by chemical reduction method using hydrazine monohydrate

In a typical process, 0.8 gm of the obtained GO powder was initially dispersed in DI water (100 mL) by using ultrasonication for 90 mins at room temperature. Then 2 mL of hydrazine

monohydrate (NH₂NH₂H₂O, purchased from Sigma Aldrich) was mixed with the GO solution and magnetically stirred for about 6 hrs at 100 °C in a controlled environment using a water condenser as shown in Fig. 2.1. After 6 hours, the reaction was stopped and cooled down to room temperature. The black precipitate was deposited at the bottom of the flask and collected by centrifuging the solution. The solid material was repeatedly washed with HCL, ethanol, and finally with DI water. The rGO powder was obtained by drying the powder in a vacuum at 80 °C for 4 hours.



GO + DI water+ Reducing agent (2mL) Stirred for 6 hours at 100 °C

Fig. 2.1 Schematic representation of the reduction of GO by hydrazine monohydrate.

2.2.3 Synthesis of Ag rGO nanomaterials

For the synthesis of Ag_rGO nanocomposites, 0.4 gm of AgNPs (average particle size ~40nm were purchased from Alfa Aesar) and 0.8 gm (1:2) of GO synthesized by improved Hummer's method was dispersed in DI water in two separate glass beakers by ultrasonication for 8 hours and 2 hours respectively as shown in Fig. 2.2. Then the solution containing AgNPs was poured into the GO solution dropwise and again sonicated for 2 hours. The solution was then transferred to a round-bottom flask and hydrazine monohydrate (4 mL) was mixed with the AgNPs/GO solution mixture. The solution was stirred for 6 hours at 100 °C similar to the reduction process of GO as discussed earlier. The reaction was stopped after 6 hours and the solution temperature was allowed to come down to room temperature and the

solid material was obtained by centrifuging the solution mixture. The Ag_rGO nanomaterials were obtained after washing the solid material several times and finally drying as discussed in the reduction process of GO.

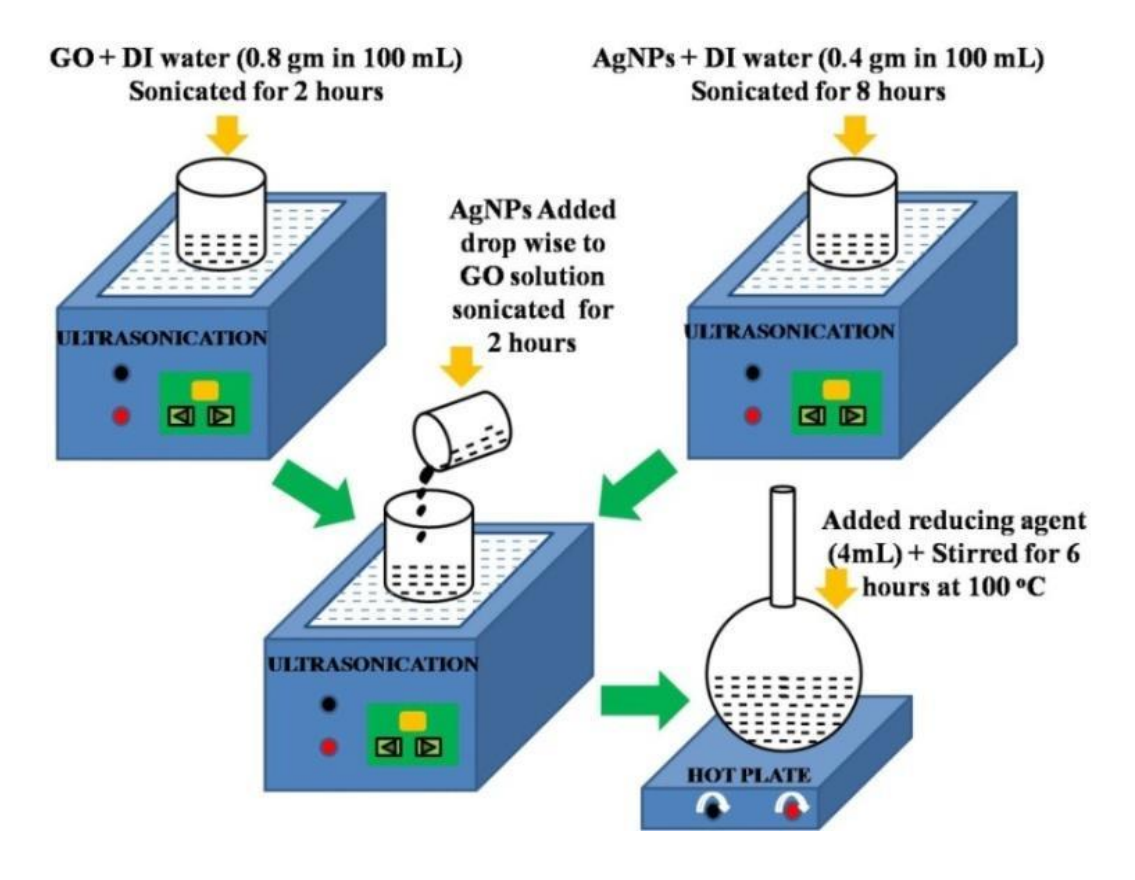


Fig. 2.2 Schematic representation of the synthesis process of Ag_rGO nanomaterials.

2.2.4 Synthesis of Ag_SWCNT and Ag_MWCNT nanomaterials

Both the Ag_SWCNT and Ag_MWCNT nanomaterials were prepared by a similar method as discussed in the earlier section. SWCNT and MWCNT were purchased from Alfa Aesar. Firstly, the Ag nanoparticles (0.3 gm) were dispersed in 200 mL of isopropanol (IPA) and 0.6 gm of CNTs (1:2) was also dispersed in 300 mL of isopropanol separately by ultrasonication for 8 hours and 2 hours respectively as shown in Fig. 2.3. Then the IPA solution containing AgnNPs was poured dropwise into the CNT solution and the solution mixture was sonicated for 3 hours. The solution mixture was then magnetically stirred for 18 hours at room temperature for proper mixing of Ag nanoparticles and CNTs. Finally, the solution mixture was centrifuged and the solid material was dried in a vacuum at 80 °C for 4 hours to obtain the Ag_SWCNT and Ag_MWCNT nanomaterials.

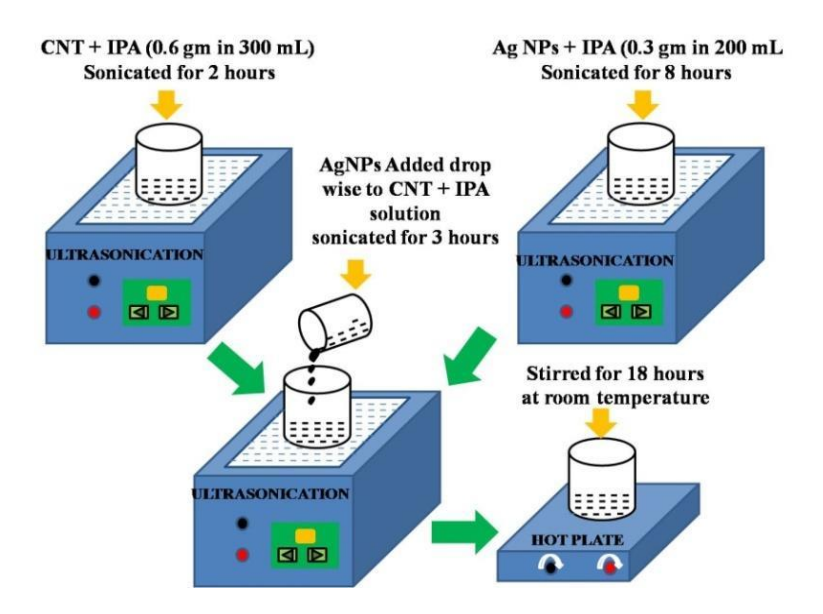


Fig. 2.3 Schematic illustration of the synthesis of Ag_SWCNT and Ag_MWCNT nanomaterials.

2.3 Characterizations of nanomaterials

2.3.1 Morphological and compositional study of nanomaterials by FESEM

The morphology of the GO, rGO, Ag-rGO, Ag-MWCNT, and Ag-SWCNT nanomaterials was investigated by using the FESEM. The FESEM images of all the obtained nanomaterials were recorded by using the FEI Nova Nanosem Field Emission Scanning Electron Microscope (FESEM). The morphology of the GO synthesized by improved Hummer's method, AgNPs, rGO, and Ag_rGO samples are shown in Fig. 2.4. As shown in Fig. 2.4 (a), it is observed that Ag NPs are agglomerated. The GO shows flake-like morphology with very thin layers as evident from Fig. 2.4 (b). The layers are piled up one on another. After chemical reduction of GO by hydrazine monohydrate, the individual layers are separated from each other as shown in Fig. 2.4 (c). The AgNPs are not distributed individually and uniformly on the surfaces of rGO but they are agglomerated as shown in Fig. 2.4 (d). This is because the AgNPs were not grown on the GO surface by the in-situ synthesis method but synthesized AgNPs were added directly during the reduction process of GO. Therefore, it is possible to form clusters and or nanoparticles agglomerate each other due to van der Waals's force of attraction. The FESEM images of Ag_SWCNT and Ag_MWCNT samples at two different magnifications are depicted in Fig. 2.4 (e--h)

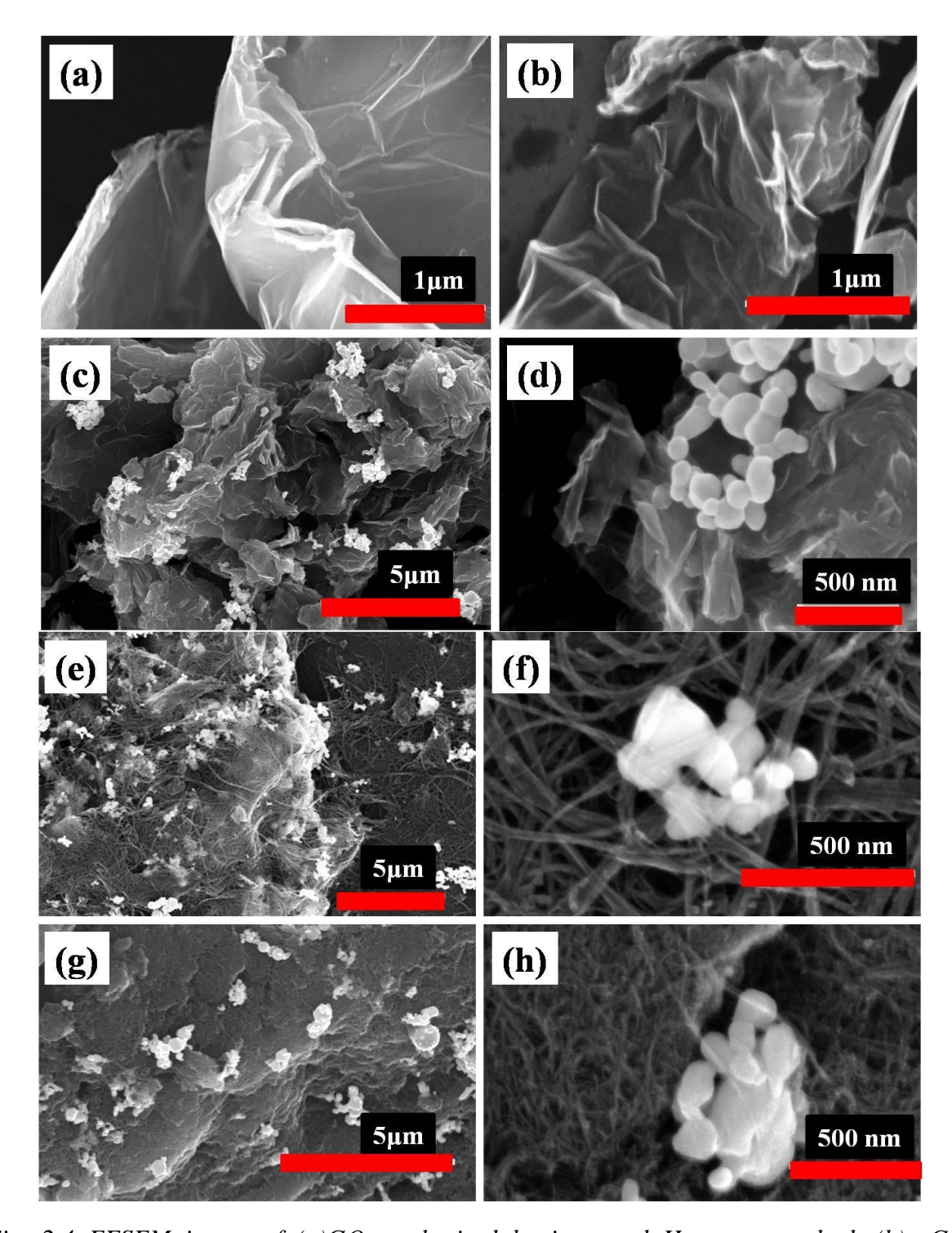


Fig. 2.4 FESEM image of (a)GO synthesized by improved Hummers method, (b) rGO synthesized by reduction process using Hydrazine Monohydrate,(c-d) Ag_rGO powder sample synthesized by reduction process using Hydrazine Monohydrate (e, f)Ag_SWCNT and (g, h), Ag_MWCNT samples at two different magnifications respectively.

It is observed that CNTs are tangled and AgNPs are distributed in between the tangled CNTs forming clusters that are attributed to the van der Waals force of attraction. The EDS

spectrum of Ag_rGO nanocomposite is also shown in Fig. 2.5 (a). The EDS spectrum of Ag_SWCNT and Ag_MWCNT is also shown in Fig. 2.5 (b) and (c) respectively.

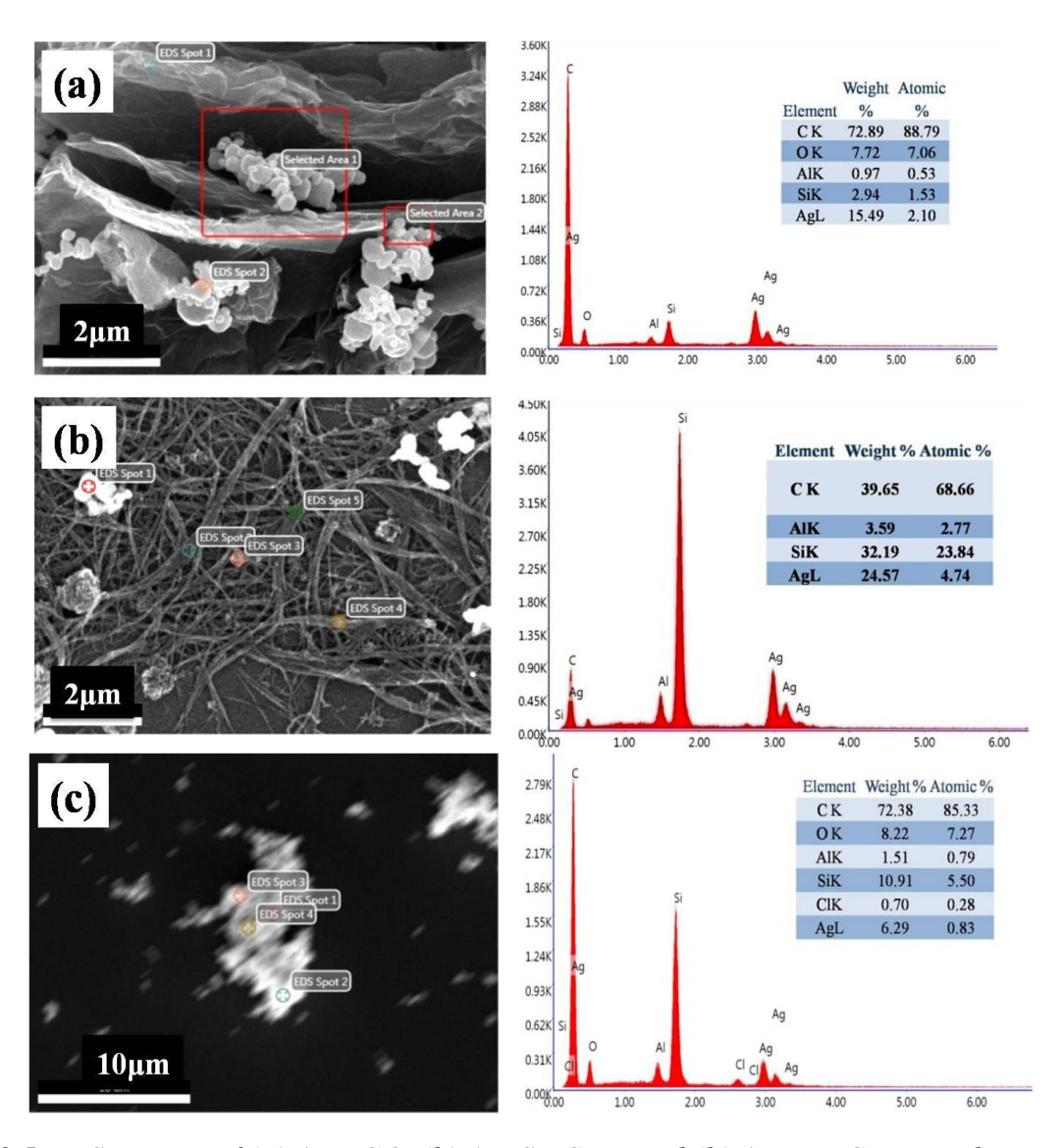


Fig. 2.5 EDS spectra of (a) Ag_rGO, (b) Ag_SWCNT, and (b) Ag_MWCNT powder samples respectively.

2.3.2 Morphological study of nanomaterials by TEM

The morphology of the nanomaterials was also studied by using HRTEM (FEI Model Tecnai G2 S Twin, 200 kV). The TEM images of GO and rGO are shown in Fig. 2.6. (a) and (d) respectively. From the TEM images, it is seen that GO and rGO samples show sheet-like morphology: the numbers of layers are stacked together forming wrinkles and scrolls. The higher transparent nature of the TEM images of GO and rGO indicates thinner sheets with a few layered structures as shown in Fig. 2.6 (a), and (d). The numbers of layers in GO are

approximately 10 and the number of layers for rGO is approximately 3 as shown in Fig. 2.6 (b), and (e) respectively. The SAED pattern of GO shows a distorted hexagonal crystalline structure which upon chemical reduction retained the crystalline nature up to some extent which is shown in Fig 2.6 (c), and (f) respectively. The TEM image of AgNPs shows that the particles of the size of the nanoparticles ranging from ~20nm to 50nm are present.

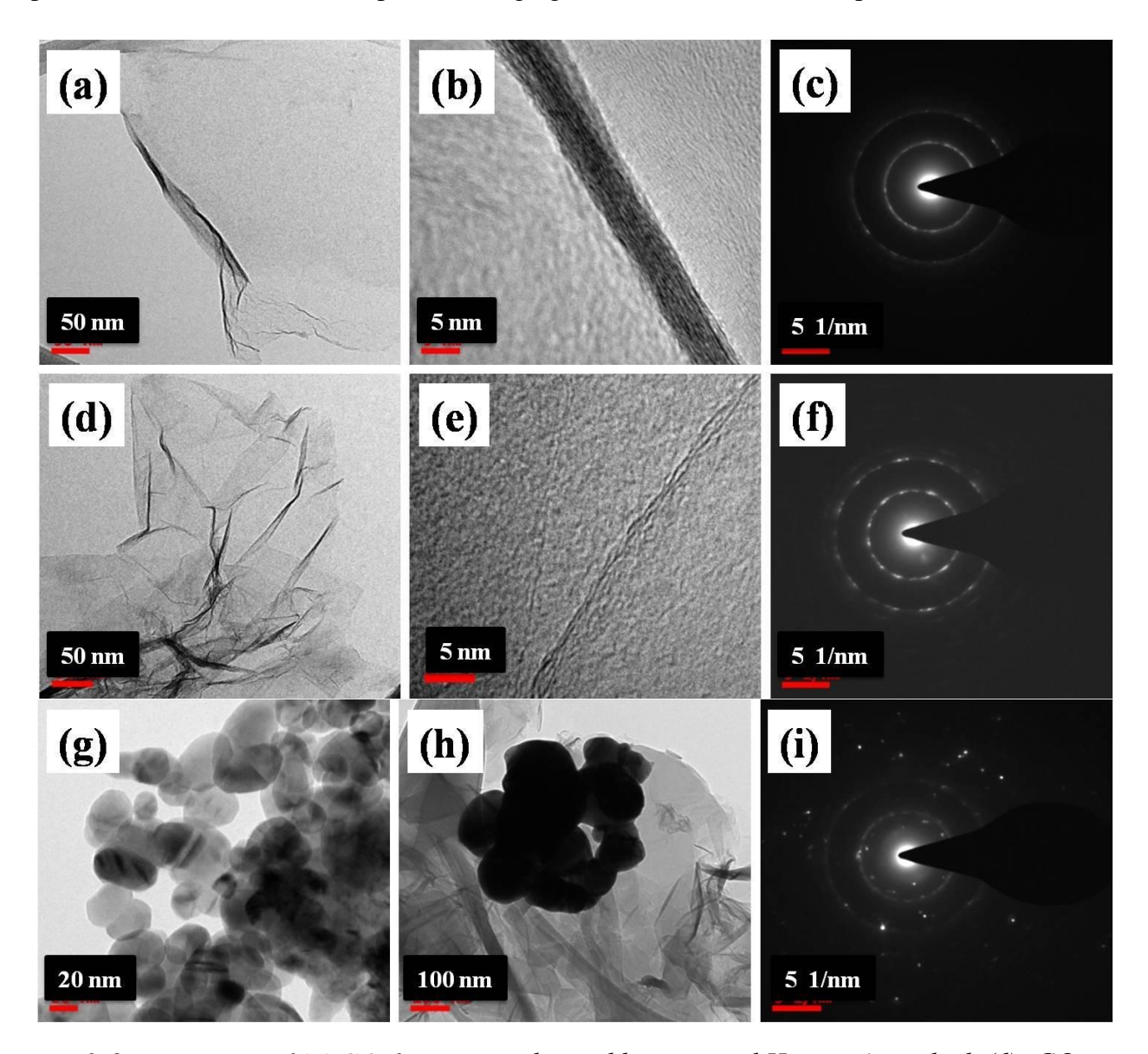


Fig. 2.6 TEM image of (a) GO that was synthesized by improved Hummer's method, (d) rGO synthesized by reduction process using Hydrazine Monohydrate, (g) AgNPs, and (h) Ag_rGO powder sample synthesized by reduction process using Hydrazine Monohydrate respectively. TEM image showing the numbers of layers of (b) GO and (e) rGO respectively. SAED pattern of (c) GO, (f) rGO, and (i) Ag_rGO respectively.

It is evident from the TEM image (Fig. 2.6 (h)) that a cluster of AgNPs is sitting on the surface of rGO flakes. The TEM images of Ag_MWCNT and Ag_SWCNT samples synthesized by directly mixing AgNPs with CNTs are depicted in Fig. 2.7 (a, b, d, e). There

is non-covalent interaction between the CNTs and AgNPs as the size of the nanoparticles is larger than the diameter of the CNTs. As AgNPs are tangled with the CNTs forming clusters, their presence can be seen in the crystal structure of CNTs as shown in the SAED pattern as shown in Fig. 2.7 (c and d).

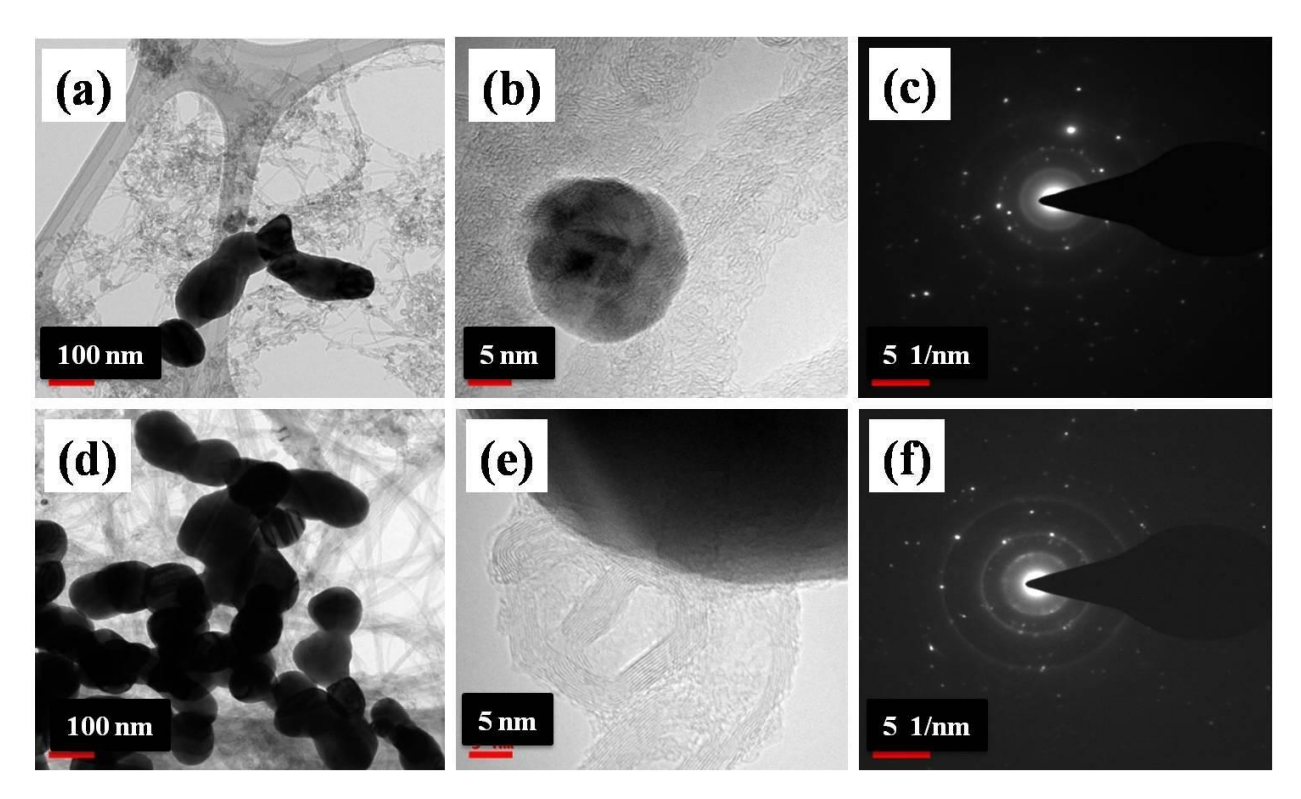


Fig. 2.7 TEM images for (a,b) Ag_MWCNT and (d,e) Ag_SWCNT nanomaterials at two different magnifications respectively. SAED pattern of (c) Ag_MWCNT and (f) Ag_SWCNT respectively.

2.3.3 Structural analysis of the nanomaterials by XRD

The X-ray diffraction (XRD) patterns of the nanomaterials were obtained by using XRDD8, Bruker diffractometer (CuK α radiation, λ = 1.54 Å), where the angle of diffraction was taken from 5° to 70°. The XRD pattern of GO, rGO, AgNPs, and Ag_rGO nanomaterial is shown in Fig. 2.8. The XRD peak of GO is found at a diffraction angle of 2θ = 10.5° which is attributed to the (001) crystal plane and the corresponding d-spacing is 0.841nm [120]. The d-spacing of pristine graphite of 45µm flake size is nearly 0.35 nm as stated earlier. It is noticed that there is a considerable difference between the d-spacing of GO and graphite which confirmes that the graphitic layers were oxidized during the synthesis process by the insertion of oxygenated functional groups between layers. The XRD peak which is observed at 2θ = 44° and 45° in the XRD pattern of GO and rGO can be attributed to the short-range order in the

stacked graphitic layers [120]. These two peaks signify the (100) crystal plane where the oxygenated functional groups are stacked with the graphitic layers of graphite oxide [121]. The reduction of GO to rGO is confirmed from the diffraction peak which is observed at $2\theta = 24.26^{\circ}$ with the corresponding d-spacing of 0.372 nm as shown in Fig. 2.8. The interlayer spacing of GO decreases upon reduction which is primarily because of the removal of the functional groups containing oxygen and restacking of the rGO sheets [122]. The humps observed at $2\theta = 12^{\circ}$ and 19° in the XRD pattern of rGO are due to the multimodal/bimodal characteristics of the d-spacing of rGO layers [123].

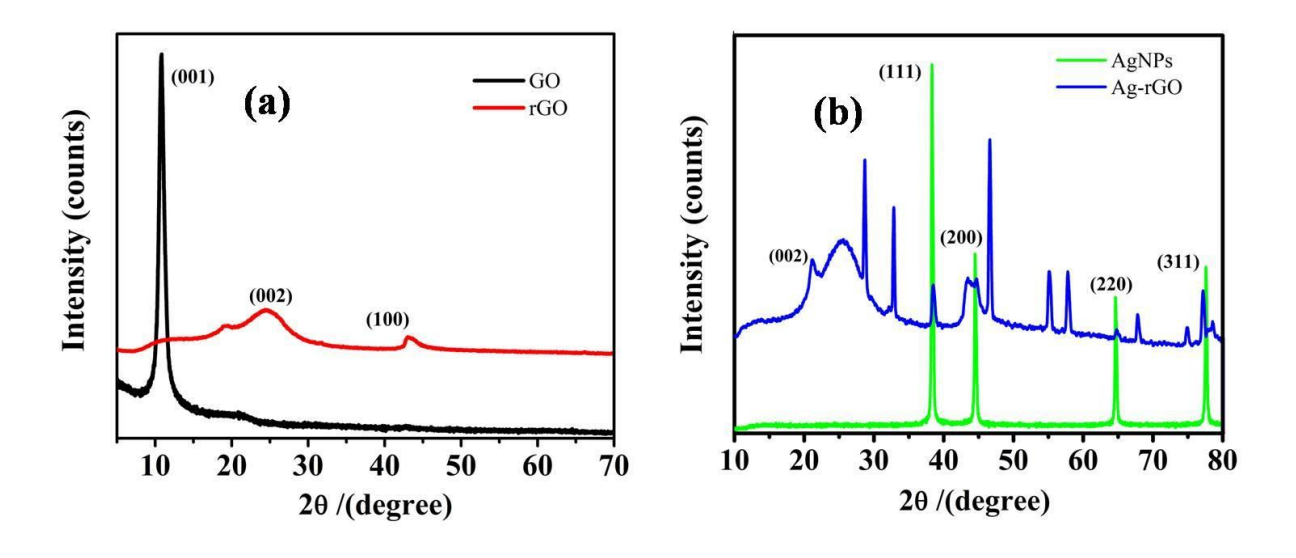


Fig. 2.8 XRD pattern of (a) GO synthesized by improved Hummers method, rGOsynthesized by chemical reduction process using Hydrazine Monohydrate, (b) AgNPs, and Ag_rGO powder sample synthesized by reduction process using Hydrazine Monohydrate respectively.

The XRD pattern of AgNPs shows diffraction peaks at $2\theta = 38.2^{\circ}$, 44.49° , 64.67° , and 77.65 correspondings to the crystal planes such as (111), (200), (220) and (311) respectively [124]. The XRD peaks related to rGO and AgNPs are present in the XRD peaks of Ag_rGO nanomaterial which is shown in Fig. 2.8. Some additional peaks which are observed at 28.5° , 32.6° , 46.5° , 54.9° , 57.6° , 68.5° , and 75.4° diffraction angles are due to unwanted metal and organic compounds [125, 126].

The XRD patterns of SWCNT, Ag/SWCNT, MWCNT, and Ag/MWCNT nanomaterials are presented in Fig. 2.9 (a, b). The diffraction peak that appears at $2\theta = 26^{\circ}$ and $2\theta = 25.8^{\circ}$ corresponds to the (002) crystal plane of SWCNTs and MWCNTs as shown in Fig. 2.9.

(a) and (b) respectively [127]. The diffraction peaks related to AgNPs, SWCNT, and MWCNT are present in the XRD pattern of Ag/SWCNT and Ag/MWCNT nanomaterials.

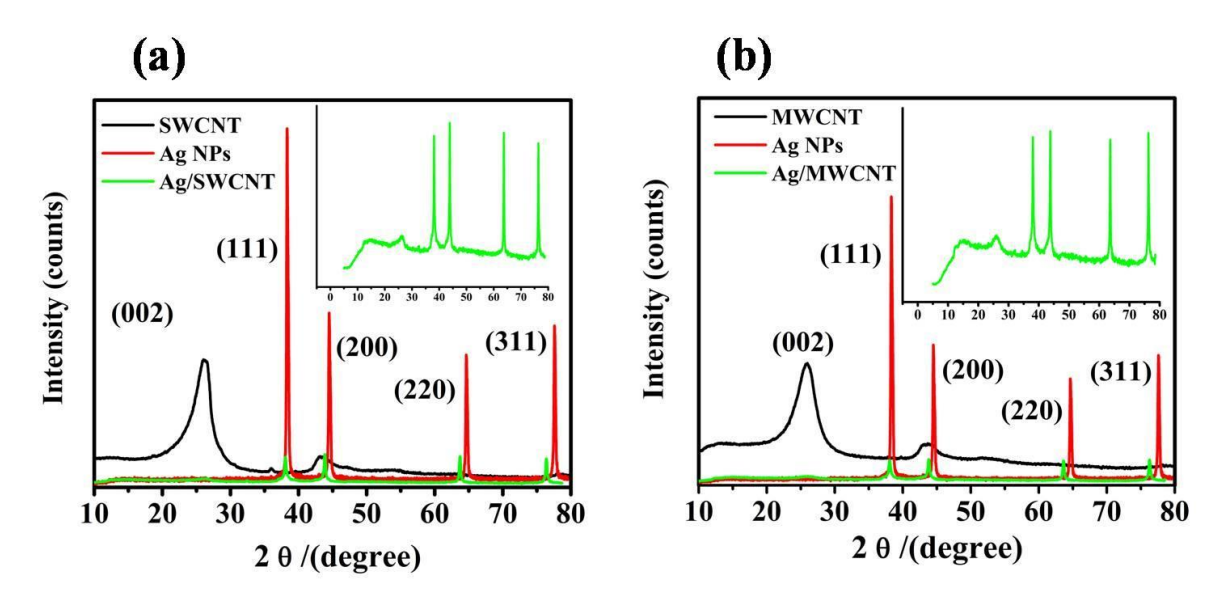


Fig. 2.9 (a) XRD pattern of Ag/SWCNT and (b) Ag/MWCNT nanomaterials respectively.

However, the intensity of these peaks is very low and hence they are presented separately in the inserted images in the XRD plots. No unwanted peaks appear in the XRD pattern of Ag_CNTs as observed for Ag_rGO samples. Therefore, the unwanted peaks in the Ag_rGO samples are due to some metal compounds which were added to the samples due to the chemical reduction process by hydrazine monohydrate.

2.3.4 Molecular vibrational analysis of the nanomaterials by FTIR spectroscopy

The Fourier Transform Infrared Spectroscopy (FTIR) of the nanomaterials was performed in transmittance mode from 400 to 4000 cm⁻¹ wave-number range by using PerkinElmer FTIR/FIR Spectrometer, Frontier. The FTIR spectrums of GO, rGO, AgNPs, and Ag_rGO nanomaterials are shown in Fig. 2.10. In the FTIR spectra of the nanomaterials, the broad peaks that appear at the wavenumber from~ 3385 to 3350 cm⁻¹ are the O-H vibration and the intensity of the peak is lower for the rGO sample than the GO [128]. The other peaks of GO which are found in the wavenumber~ 1740, 1630, 1372, 1290, and 1074 cm⁻¹ represents the C=O (sp²-hybridized C group after oxidation), C=C (graphitic carbon), C-OH, C-O-C (epoxy symmetric ring deformation), and C-O (alkoxy group) vibrational modes respectively [128, 129]. The FTIR spectrum of rGO exhibits two peaks at wavenumber~1182 and 1550 cm⁻¹ which are ascribed to the C=C and C-O vibrational modes respectively.

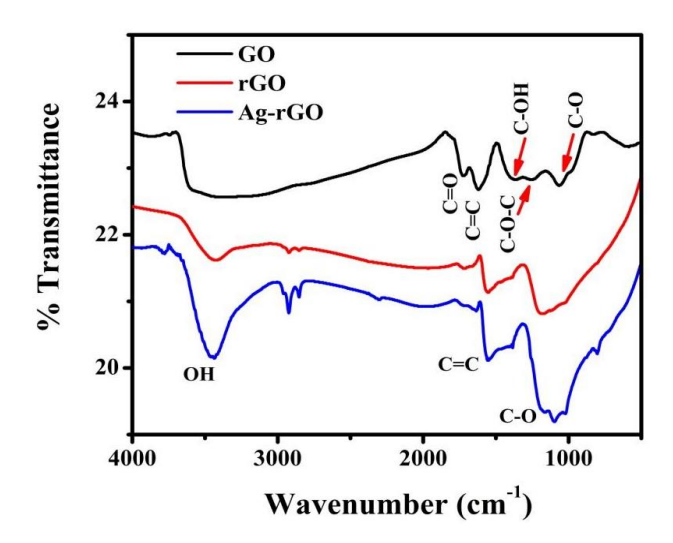


Fig.2.10 FTIR spectrum of GO, rGO, and Ag_rGO powder samples synthesized by reduction process using Hydrazine Monohydrate respectively.

The other oxygenated groups including C=O, C-OH are not present in the FTIR spectra of rGO which suggests that GO is entirely reduced to rGO effectively and the sp² carbon network has been restored up to some extent [130]. The Ag-O ionic group and Ag-Ag metallic group vibrational modes are not present in the FTIR spectra as these modes appear in the FIR region.

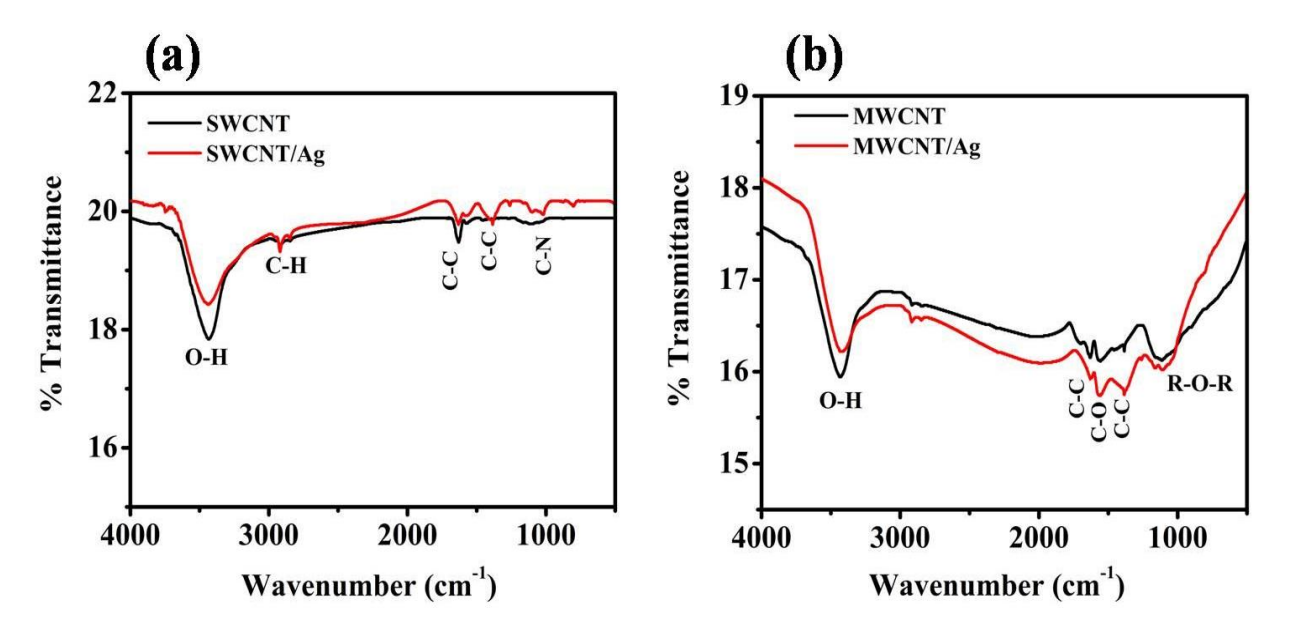


Fig. 2.11 FTIR spectra of (a) SWCNT, Ag_SWCNT, and (b) MWCNT, Ag_MWCNT nanomaterials respectively.

The peaks that appear at 1081, 1331, and 1625 cm⁻¹, which are present in the FTIR spectra of AgNPs are due to the C-N, C-C, and -C=C-, and stretching modes and these peaks appear due to the PVP blends present in the AgNPs as dispersant [131]. In the FTIR spectra of

SWCNT and MWCNT samples, the molecular vibrational peaks at 3440 and 2918cm⁻¹ are ascribed to O-H and C-H stretching modes which are shown in Fig. 2.11. The FTIR peaks that appear at 1628 cm⁻¹ in both spectra as shown in Fig. 2.11 is the C-C stretching mode of vibration [132]. The FTIR peak at 1558 cm⁻¹ represents the C-O stretching mode [133]. The other peaks that appear at 1377, 1343 and 1056 cm⁻¹ are related to the C-C and C-N stretching vibration modes present in the AgNPs [131].

2.3.5 Raman spectroscopy analysis of the nanomaterials

The Raman spectroscopy was performed by using Witec-300, Focus Innovation instrument (532nm laser wavelength). The Raman spectra of the GO, rGO, AgNPs, and Ag_rGO nanocomposites are shown in fig 2.12. The most significant Raman shift corresponding to GO and rGO appears due to the D-band which represents the breathing mode of j-point photons of A_{1g} symmetry and the G-band which represents the first-order scattering of E_{2g} phonons by sp² carbon respectively [134]. The D and G bands also represent the disorder in the sp² lattice of GO due to structural defects and the C-C stretching vibration in the sp² carbon network [135].

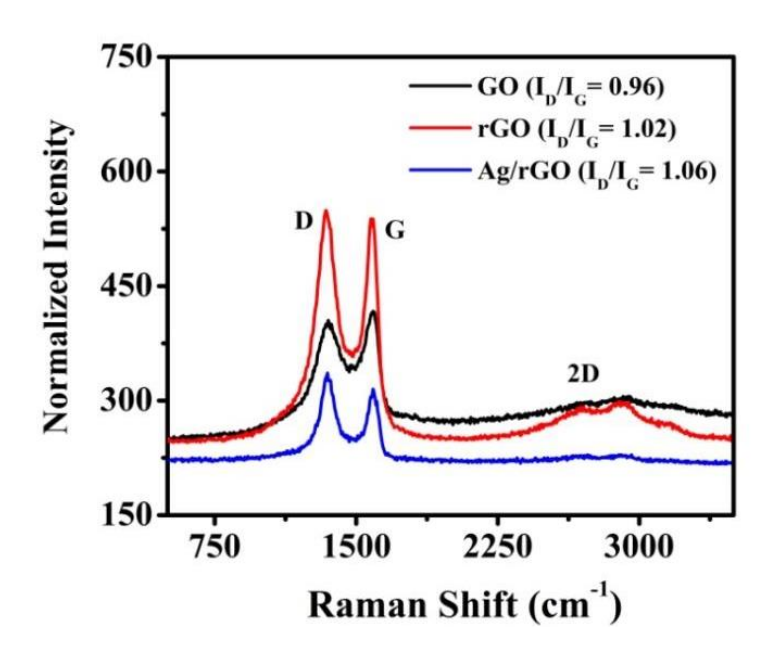


Fig. 2.12 Raman spectra of GO, AgNPs, rGO, and Ag_rGO powder sample synthesized by chemical reduction process using Hydrazine Monohydrate respectively.

The D bands of GO, rGO, and Ag_rGO samples in the Raman spectra appear at 1352, 1340, and 1348 cm⁻¹ respectively. Similarly, the G bands of GO or rGO and Ag_rGO appear at 1590, 1582, and 1588 cm⁻¹ respectively. The calculated I_D/I_G values of GO, rGO, and Ag_rGO are 0.96, 1.02, and 1.06 respectively. The peak shift of D and G bands and the

increasing I_D/I_G ratios suggest that the small-sized aromatic domain increases in the samples upon removal of oxygenated functional groups from the GO surfaces in the chemical reduction process [134, 136]. Also, the presence of a low-intensity 2D peak at 2695 cm⁻¹ signifies the few-layer structure of rGO [134].

The Raman spectra of SWCNT, Ag_SWCNT, MWCNT, and Ag_MWCNT samples are shown in fig 2.13. The D, G, and 2D bands of both SWCNT and MWCNT appear at 1340, 1570 and 2665 cm⁻¹ respectively. However, the D-band intensity corresponding to the CNTs is lower than the G-band intensity which suggests the presence of more sp³ hybridized carbon atoms in CNTs [137]. The difference between the intensities of D and G bands is not prominent for MWCNT. The D-band and G-band corresponding to the Ag_SWCNT sample is present at 1396 and 1598 cm⁻¹ respectively. Similarly, the D-band and G-band of Ag_MWCNT are observed at 1354 and 1590 cm⁻¹ respectively. The D-band and G-band intensity of the Ag_SWCNT and Ag_MWCNT samples are higher than the intensities of these peaks corresponding to the pristine CNTs.

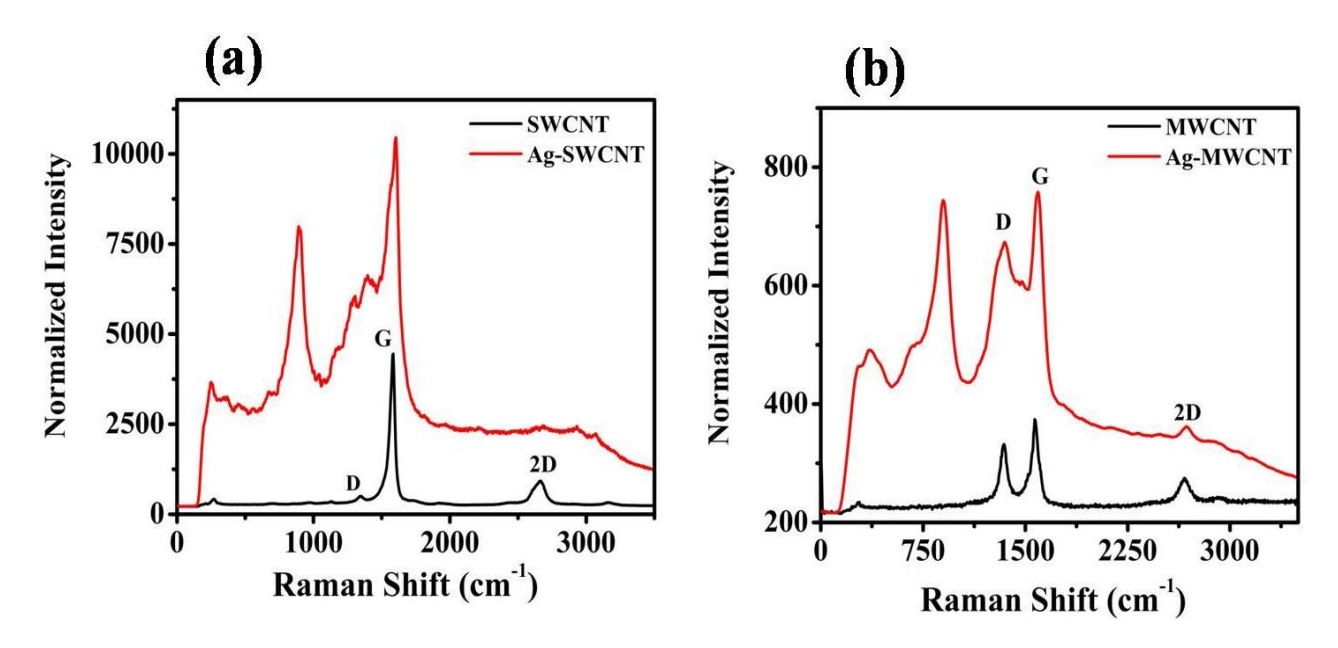


Fig. 2.13 Raman spectra of (a) SWCNT, Ag_SWCNT, and (b) MWCNT, Ag_MWCNT nanomaterials respectively.

Additionally, peak broadening and peak shifting of D and G bands are observed which are due to the presence of AgNPs in between the tangled CNTs [129]. The reason for the occurrence of the peak at 908 cm⁻¹ is not known because the physics of the intermediate frequency mode of CNTs from 600 to 1100 cm⁻¹ is complex and a similar peak was found for other functionalized CNT samples [138].

2.4 Conclusions

For the fabrication of PDMS-based smart composite materials and flexible sensors, we synthesized different nanomaterials such as GO, rGO, Ag_rGO, Ag_SWCNT, and Ag_MWCNT. Firstly, GO was synthesized by the improved Hummers method, and GO was chemically reduced by using hydrazine monohydrate to obtain rGO. Secondly, AgNPs were used to produce Ag_rGO nanomaterials by the chemical reduction method. Similarly, Ag SWCNT and Ag MWCNT nanomaterials were prepared by direct mixing the CNTs and AgNPs in isopropanol. To evaluate different properties of the nanomaterials such as the morphology, molecular structure, and chemical compositions, several analytical characterizations were utilized. From the TEM images, it is observed that the GO and rGO show a few-layer morphology. The reduction of GO to rGO is confirmed from the XRD analysis. From the FTIR and Raman analysis, it is observed that the reduction process removed the oxygenated functional groups of GO. The TEM images of Ag_rGO show that the AgNPs are sitting on the rGO surface forming clusters. The presence of AgNPs in the Ag rGO sample is confirmed from the XRD and FTIR analysis. The TEM, XRD, FTIR, and Raman analysis of Ag_SWCNT and Ag_MWCNT show that the AgNPs are distributed between the tangled CNTs.

CHAPTER 3

Fabrication and Characterizations of PDMS-Nnaofiller-based composites

3.1 Introduction

In this chapter, the fabrication process of PDMS-based composite materials is presented. The PDMS-based nanocomposites were fabricated by incorporating different carbon-based nanomaterials which were mentioned in chapter 2, such as GO, rGO, Ag_rGO, Ag_SWCNT, and Ag_MWCNT. Five different wt% of the nanomaterials were used for the fabrication of PDMS nanocomposites. All the fabricated PDMS-based nanocomposites were characterized for morphology, structure, and identification of molecular vibrations present in the samples by using different analytical methods such as SEM, XRD, FTIR, and Raman spectroscopy. The distribution of the nanomaterials in the PDMS polymer matrix was also investigated which is presented in this chapter.

3.2 Fabrication of PDMS-based nanocomposites

The PDMS-based nanocomposites were fabricated by a solution mixing method where five different wt% of each nanofiller material such as GO, rGO, Ag_rGO, Ag_SWCNT, and Ag_MWCNT were incorporated. The fabrication process of PDMS-based composites is presented schematically in Fig.3.1. Firstly, the pre-calculated amount of nanofiller materials were dispersed in ethanol (10 mL) by using ultrasonication for 8 hours at room temperature.

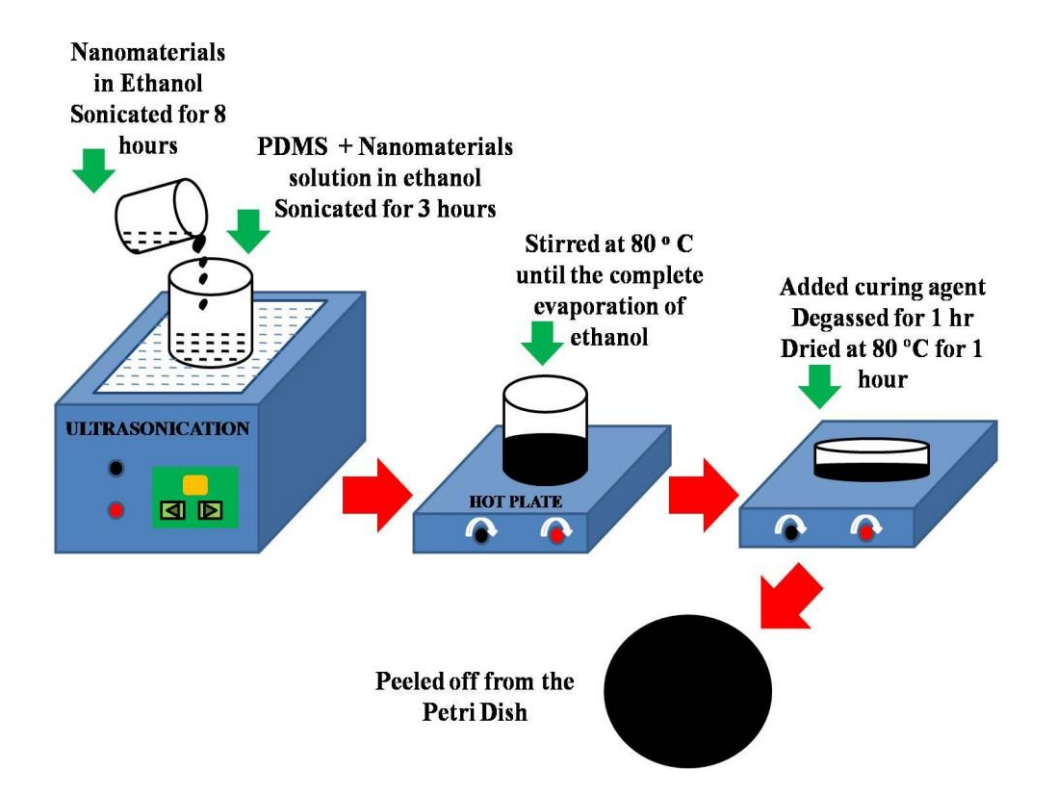


Fig. 3.1 Schematic presentation of the fabrication process of PDMS-based composites.

Secondly, 5 mL of PDMS (SYLGARD 184) pre-polymer was taken in a glass beaker and the dispersed solutions of nanofiller were added dropwise to the PDMS pre-polymer followed by ultrasonication at room temperature for 3 hours. Thirdly, the nanofiller-PDMS solution mixture was magnetically stirred till the complete evaporation of ethanol at 80 °C. Fourthly, the nanofiller-PDMS solution mixture was cooled down and PDMS curing agent was added to it. The nanofiller-PDMS with curing agent mixture was degassed by using a vacuum pump to eliminate the air bubbles that were formed inside the elastomer-nanofiller mixture. Finally, the elastomer-nanofiller mixture was transferred to a plastic Petri-dish and was dried at 80 °C to obtain the solid PDMS-based composite samples. Table 3.1 shows the details about the nanofillers and wt% for the fabrication of PDMS nanocomposites. The wt% of the nanofillers was calculated by using the following equation

$$wt\% = \frac{M_{filler}}{M_{filler} + M_{CA} + M_{PDMS}} \times 100$$

Where, M_{filler} , M_{CA} , and M_{PDMS} are the mass of the nanofiller, the mass of the curing agent, and mass of the PDMS pre-polymer respectively.

Table 3.1 Specification and wt% of nano-fillers that are utilized for the fabrication of PDMS composites.

Nanofiller	wt %	Number of samples
GO	0.1, 0.25, 0.5 0.75 and 1	5
rGO	0.1, 0.25, 0.5 0.75, 1,	5
AgNPs	0.1, 0.25, 0.5 0.75, 1,	5
Ag_rGO	0.1, 0.25, 0.5 0.75 and 1	5
Ag_MWCNT	0.1, 0.25, 0.5 0.75 and 1	5
Ag_SWCNT	0.1, 0.25, 0.5 0.75 and 1	5

3.3 Characterizations of PDMS-Nanofiller composites.

3.3.1 Morphological study of PDMS-Nanofiller composites by SEM

The morphology GO/PDMS, Ag/PDMS, rGO/PDMS, Ag_rGO/PDMS, Ag_SWCNT/PDMS, and Ag_MWCNT/PDMS samples containing 1 wt% of nano-fillers are shown in Fig. 3.2 (a-n). It is observed from the SEM images that the nano-fillers are not uniformly distributed and agglomerated in the PDMS matrix. The agglomeration is observed for GO/PDMS,

Ag/PDMS, and rGO/PDMS-based composites and that is shown in Fig. 3.2 (a-f). However, the agglomeration of the nanofillers is lesser for Ag_rGO/PDMS, Ag_MWCNT/PDMS, and Ag_SWCNT/PDMS composites than for the GO/PDMS, Ag/PDMS, and rGO/PDMS composites as shown in Fig. 3.2 (i-n).

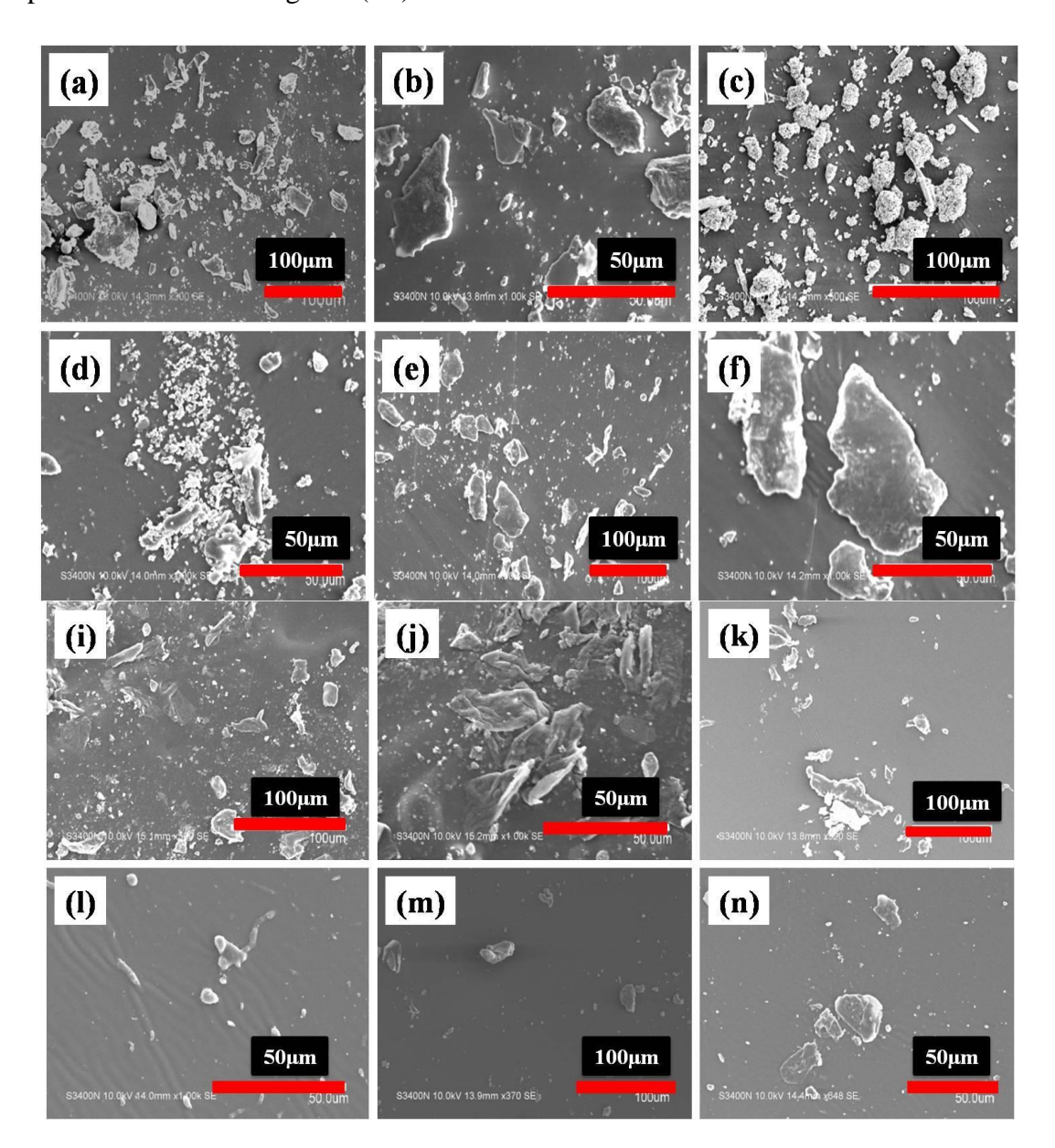


Fig. 3.2 The SEM micrograhs of 1 wt% GO/PDMS (a, b), Ag/PDMS (c, d), rGO/PDMS (e, f), Ag_rGO/PDMS (g, h), Ag_SWCNT/PDMS (i, j), and Ag_MWCNT/PDMS (k, l) respectively in two different magnification (100 μ m and 50 μ m).

3.3.2 Structural analysis of PDMS-Nanofiller composites by XRD

The XRD pattern of GO/PDMS, Ag/PDMS, rGO/PDMS, Ag_rGO/PDMS, Ag_SWCNT/PDMS, and Ag_MWCNT/PDMS samples are shown in Fig. 3.3 (a-e). In all the

XRD patterns, the broad peak that appears between the $2\theta = 10^0$ to 15^0 corresponds to the diffraction from the amorphous phase of neat PDMS [139].

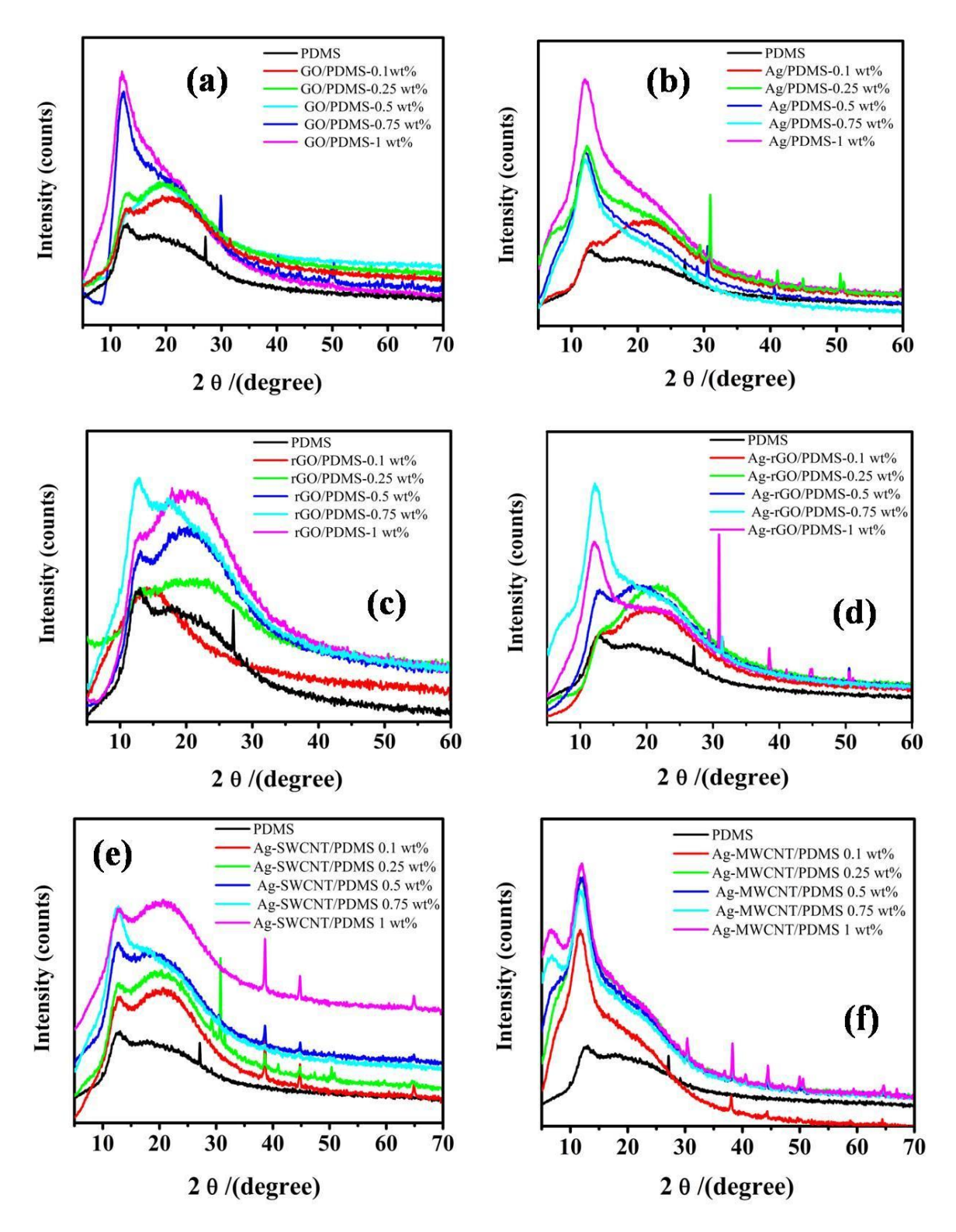


Fig. 3.3 XRD pattern of (a) GO/PDMS, (b) Ag/PDMS (c) rGO/PDMS, (d) Ag_rGO/PDMS, (e) Ag_SWCNT/PDMS and (f) Ag_MWCNT/PDMS polymer composites fabricated by incorporating nanofillers with different wt%.

It is also found that the intensity of the amorphous peak of PDMS increases with increasing the nanofiller wt%. The variation in the intensity of PDMS nanocomposites indicates that the nanofillers in the PDMS matrix disrupt the local order in the amorphous crystal structure of the PDMS matrix. The intercalation of nano-fillers during the solution mixing process into the PDMS matrix possibly restricts the mobility of the polymer chain and limits the cross-linking process during polymerization reaction [28, 139]. In the XRD pattern of Ag/PDMS, Ag_rGO/PDMS, Ag_SWCNT/PDMS, and Ag_MWCNT/PDMS the diffraction peaks which appears at $2\theta = 38.4^{\circ}$, 44.4° , and 64.6° are corresponding to (111), (200), and (220) crystal planes of AgNPs respectively [124]. Some additional peaks which are observed at 29.5°, 31°, 41°, 45°, 50.4°, and 51.6° diffraction angles are due to unwanted metal and organic compounds [125, 126]. The XRD peaks related to both GO and rGO are not present in the XRD pattern of PDMS composites.

3.3.3 FTIR analysis of PDMS-Nanofiller composites

The effect of nanofiller incorporation in the molecular bonding of the PDMS nanocomposites was studied from the FTIR spectra as shown in Fig. 3.4. Carbon-based nanofillers are used for the fabrication of PDMS composites and hence ATR reflectance data was taken instead of % transmittance. The neat PDMS sample exhibits FTIR reflectance peaks in the wavenumber ~785 cm⁻¹ to 690 cm⁻¹ which are related to the CH₃ (rocking) and Si-C (stretching) in the Si-CH₃ vibrational peaks. The FTIR peaks in the wavenumber ~1015, 1260, 1410, and 2965 cm⁻¹ are related to the symmetric deformation of Si-O-Si, deformation of CH₃ in Si-CH₃, and CH₃ deformation (asymmetric) in Si-CH₃ molecular vibrations respectively [140, 141]. From the FTIR spectra of GO_PDMS, Ag/PDMS, rGO/PDMS, Ag_rGO/PDMS, Ag_SWCNT/PDMS, and Ag_MWCNT/PDMS polymer composites, it is observed that the FTIR peaks related to the vibrational mode of different functional groups of the nanofillers are not present. However, the small amount of change in the peak intensity of the PDMS nanocomposites containing higher wt% of nanofillers indicates the formation of Si-C bond that is due to the H-bonding (hydrogen-bonding) between the nanofillers and PDMS matrix [142].

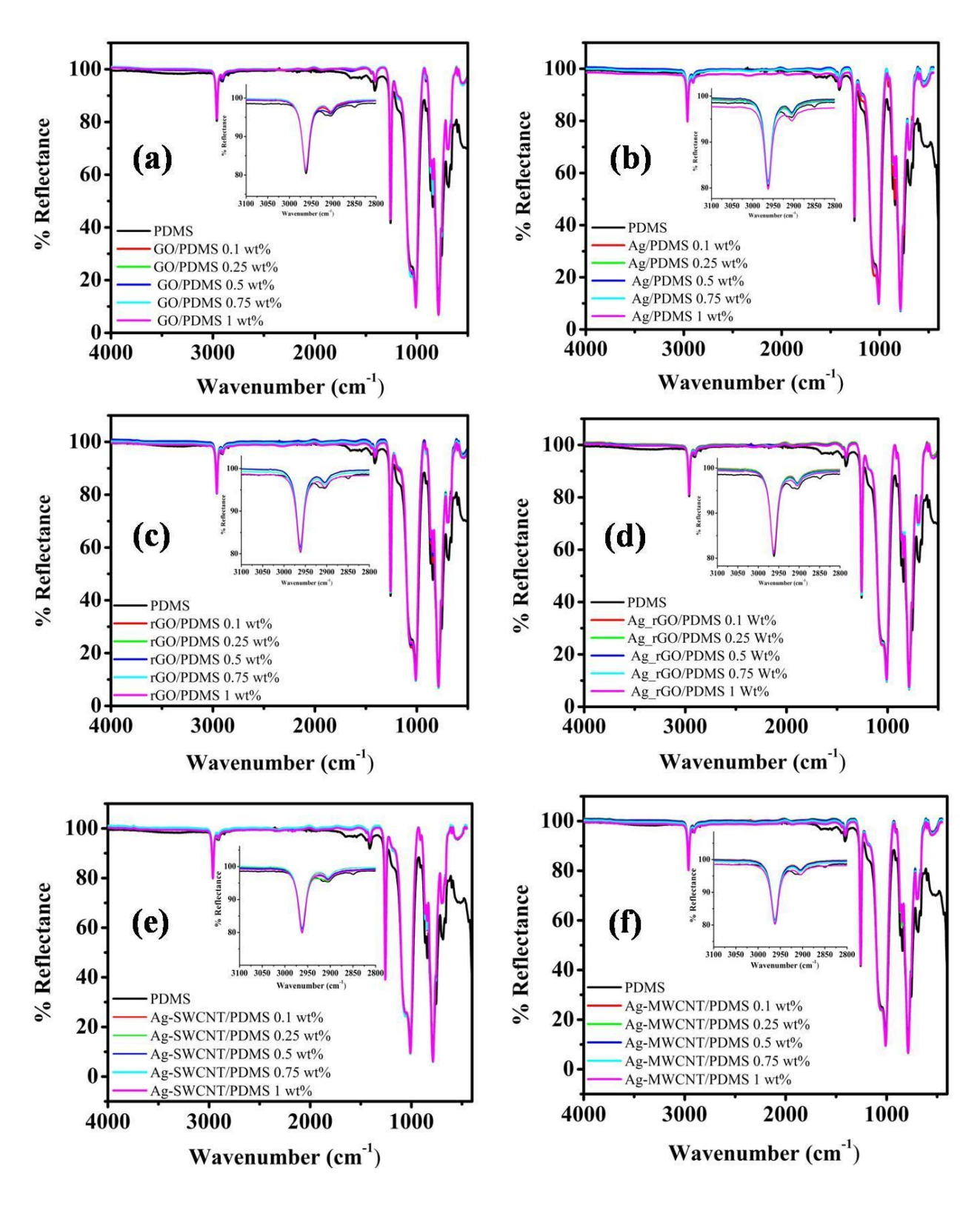


Fig. 3.4 FTIR spectra of (a)GO/PDMS (b) Ag/PDMS (c) rGO/PDMS, (d) Ag_rGO/PDMS, (e) Ag_SWCNT/PDMS and (f) Ag_MWCNT/PDMS composites with different wt% respectively.

3.3.4 Raman analysis of PDMS-Nanofiller composites

The Raman spectra of GO/PDMS, Ag/PDMS, rGO/PDMS, Ag_rGO/PDMS, Ag_SWCNT/PDMS, and Ag_MWCNT/PDMS nanocomposites with different wt% of nanofillers are shown in fig 3.5. Neat PDMS shows Raman shift at wavenumber 490, 620, and 710 cm⁻¹ which corresponds to Si-O-Si symmetric deformation, rocking mode of Si-CH₃, and stretching mode of vibrations of Si-C in the polymer matrix of pristine PDMS respectively as shown in Fig. 3.6.

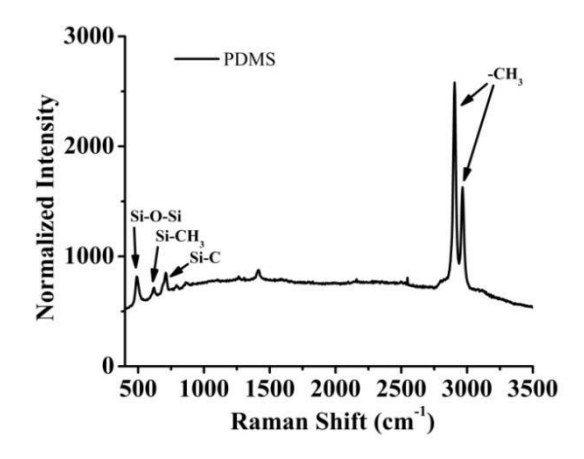


Fig. 3.5 Raman spectra of neat PDMS

The other Raman peaks which appear at wavenumber 1260, 1415, 2900 and 2970 cm⁻¹ are attributed to the symmetric and asymmetric vibrations of the CH₃ group in the PDMS matrix [139, 143]. From the Raman spectra of PDMS nanocomposites, it is observed that the Raman shift of all the samples containing lower wt% of nanofillers is disordered. However, for higher wt% of nanofillers, the disordered nature is not observed. The D-bands of GO, rGO, and Ag_rGO nanofiller samples appear at wavenumber 1350, 1343 cm⁻¹, and the G-bands at 1590, 1582 cm⁻¹ respectively (Chapter 2). In the Raman spectra of PDMS nanocomposites the D and G bands corresponding to GO/PDMS, rGO/PDMS, and Ag-rGO/PDMS are also present at 1355 cm⁻¹ and 1595 cm⁻¹ respectively. Along with the small peak shift, the intensity of the D and G bands gradually increases for the PDMS nanocomposites with higher wt% of nanofillers. The results indicate that the nanofillers were distributed in the PDMS matrix and hydrogen bonding between the nanofillers and PDMS matrix was present [138. 139]. However, the Raman spectra of PDMS nanocomposites containing AgNPs are more disordered and with the increase of AgNPs wt%, the Raman shift does not retain the ordered structure similar to the GO rGO and Ag-rGO based PDMS nanocomposites. In the Raman

plots of Ag_SWCNT/PDMS-based and Ag_MWCNT/PDMS-based composites, the peak that appears at 1580 cm⁻¹ is the G-band and the intensity of this peak gradually increases with the increase of CNTs wt%.

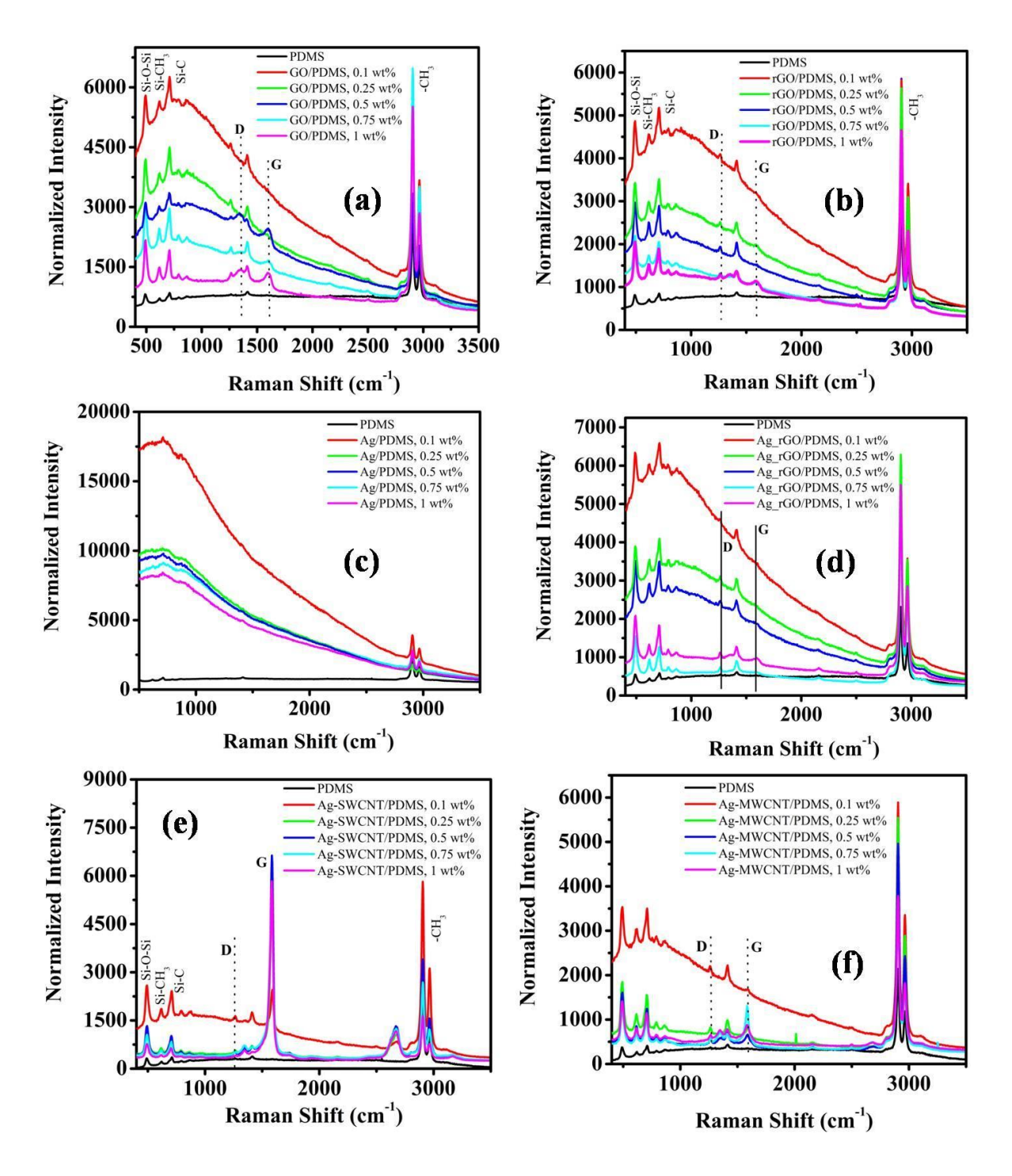


Fig. 3.6 Raman spectra of (a) GO/PDMS, (b) Ag/PDMS, (c) rGO/PDMS, (d) Ag_rGO/PDMS, (e) Ag_SWCNT/PDMS and (f) Ag_MWCNT/PDMS composites with different wt% respectively.

The G-band's peak intensity related to the Ag_SWCNT/PDMS nanocomposites is higher than the G-bands intensity related to Ag_MWCNT/PDMS composites. Additionally, the 2D

band appears at 2665 cm⁻¹ for Ag_SWCNT/PDMS composites, and the 2D band's peak intensity increases with the increase of Ag_SWCNT in the PDMS samples. Thus, the presence of D-band, G-band, and 2D-band in the Raman spectra of PDMS nanocomposites indicates the proper distribution of nanofillers in the PDMS matrix.

3.3.5 Flexibility and stretchability of PDMS-Nanofiller composites

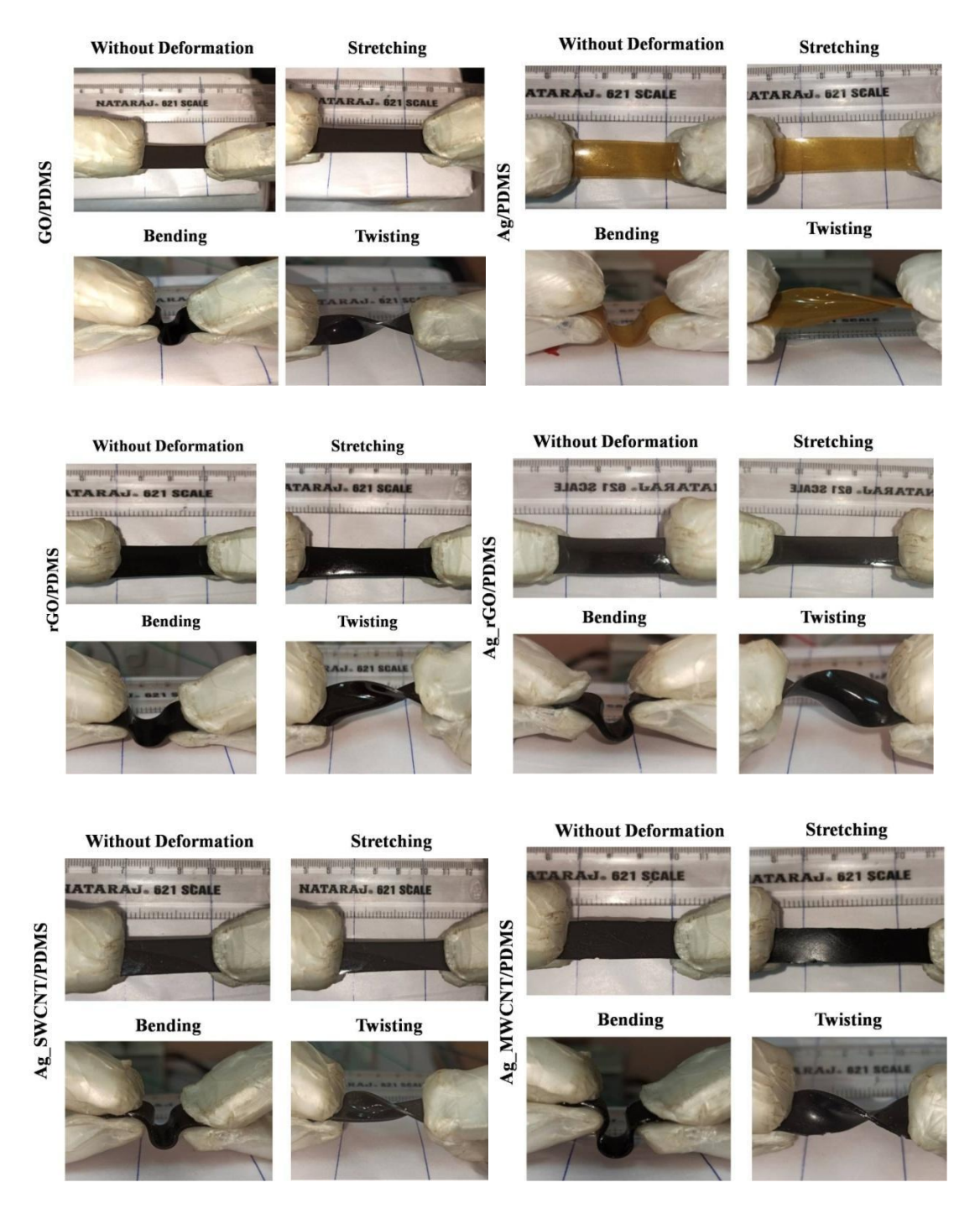


Fig. 3.7 Different modes of deformation to show the flexibility and stretchability of GO/PDMS, Ag/PDMS, rGO/PDMS, Ag_rGO/PDMS Ag_SWCNT/PDMS, and Ag_MWCNT/PDMS composites (1wt%).

The fabricated PDMS composites are flexible and it is possible to deform them by employing several modes such as stretching, bending, and twisting.

3.4 Conclusions

The PDMS nanocomposites were fabricated by incorporating different wt% of nanofillers such as GO, AgNPs, rGO, Ag_rGO, Ag_SWCNT, and Ag_MWCNT. The SEM images of PDMS-based composites show that the nanofillers are distributed in the PDMS nanocomposites but are agglomerated. The XRD, FTIR, and Raman analysis confirmed the presence of filler-matrix interaction due to the H-bonding between different functional groups that are present in the nanofillers and PDMS matrix. The PDMS composites are flexible and stretchable.

CHAPTER 4

Study of electrical properties of PDMS-Nanofiller-based composites

4.1 Introduction

The study of electrical and dielectric properties of PDMS-based composite materials is presented in this chapter. The measurements of DC-current vs voltage (*I-V*) characteristics of the PDMS-based composites were done by using the Agilent 34972A LXI data acquisition unit and DC power supply unit and the corresponding resistances were calculated. The measurements of the dielectric properties were carried out by using the "NovoConrtroll dielectric measurement system" at room temperature in the frequency range from 1 Hz to 1 kHz as shown in Fig. 4.1. For the measurements, the samples were cut into square-shaped pieces (1cm× 1cm) and both the surfaces of the samples (top and bottom) were covered with conductive Cu tape. The thickness of the samples was around ~1200μm-1300μm. The change in the dielectric permittivity, dielectric loss, AC conductivity, and capacitance of the PDMS composites to the wt% of nanofillers was investigated which will be discussed in this chapter.

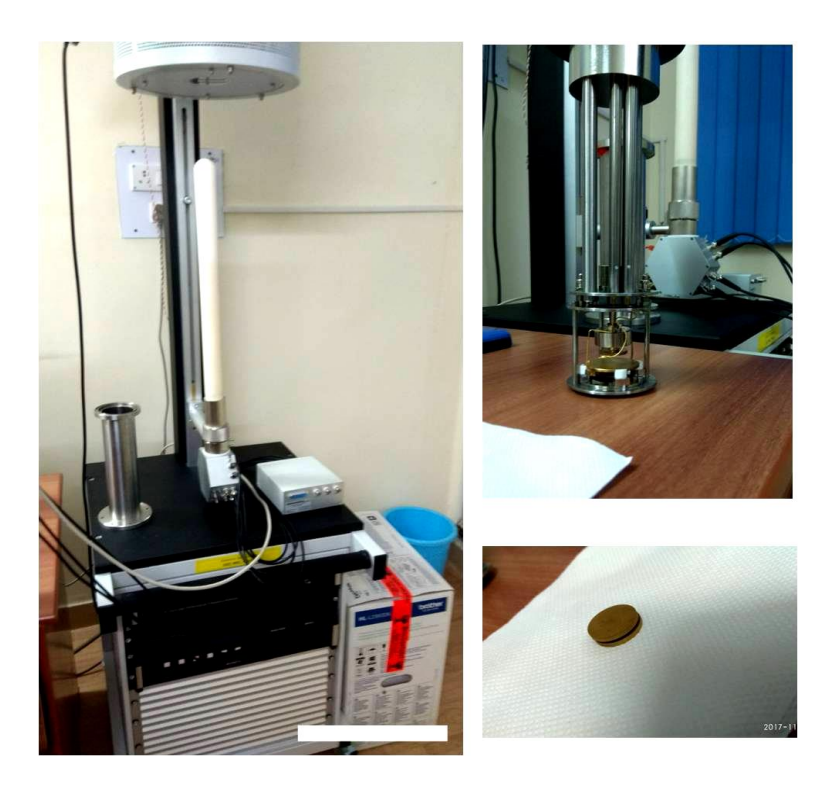


Fig. 4.1 Photograph of "NovoConrtroll Dielectric Measurement System" and sample holder.

The complex permittivity (\mathcal{E}) of a composite is related to the real (\mathcal{E}') and imaginary (\mathcal{E}'') part of the permittivity by the following equation [144].

$$\mathcal{E} = \mathcal{E}' + \mathcal{E}''$$

The capacitance (C) of capacitor electrodes with the surface area "A" separated by a distance "d" is directly proportional to the dielectric constant as shown in the equation. The loss factor $(\tan \delta)$ is the ratio between the imaginary and real part of permittivity as given in the following equation.

$$C = \varepsilon' \frac{A}{d} = \varepsilon_o \varepsilon_r \frac{A}{d}$$
$$\tan \delta = \frac{\varepsilon''}{\varepsilon'}$$

Where \mathcal{E}_o is the vacuum permittivity (8.85 \times 10⁻¹² Fm^{-1}).

4.2 Study of electrical properties of PDMS-Nanofiller composites

The measurements of DC-current vs voltage (*I-V*) characteristics of the PDMS-based composites were done by applying different voltages across the two ends of the samples and measuring the corresponding current. The applied voltages ranged from 10-80 Volts. The corresponding resistances were calculated that are shown in Fig. 4.2. It is observed from Fig. 4.2 that the resistances of the samples are in the range from $1M\Omega$ to $1G\Omega$ which are very high. The range of resistances that can be measured by the instrument in 2-wire and 4-wire ohm configuration is 100Ω to $100M\Omega$. Therefore, the results suggest that the samples are not electrically conductive. Also, the current voltage variation is non-linear, and it is not possible to obtain accurate data for the resistivity and conductivity of the samples. Hence, dielectric spectroscopy measurements were carried out for the PDMS-based composites.

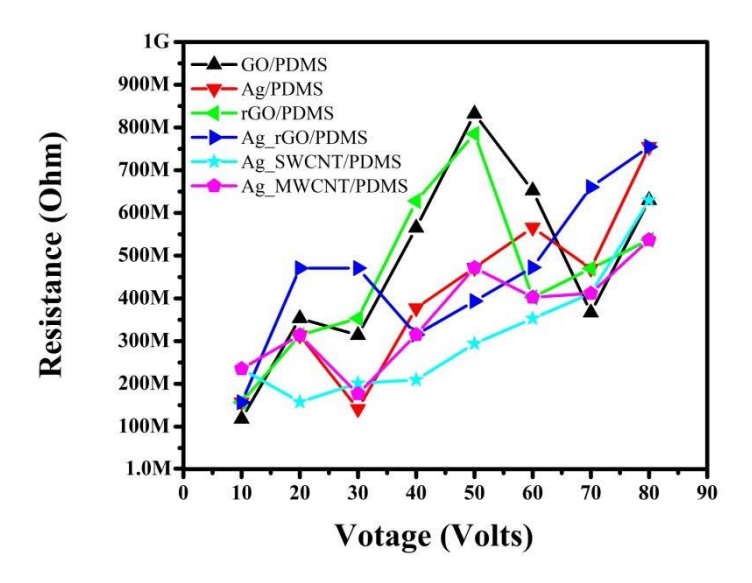


Fig. 4.2 I-V characteristics curve of the PDMS-Nanofiller-based composites.

4.3 Study of dielectric properties of PDMS-Nanofiller composites

4.3.1 Analysis of dielectric permittivity (\mathcal{E}') of PDMS-Nanofiller composites

The dielectric constant of the GO/PDMS, Ag/PDMS, rGO/PDMS, Ag_rGO/PDMS, Ag_SWCNT/PDMS and Ag_MWCNT/PDMS flexible polymer composites fabricated by incorporating 0.1, 0.25, 0.5, 0.75 and 1 wt% nanofillers are shown in Fig. 4.3 (a-f). From the results, it is observed that the dielectric constants of the PDMS composites are higher than the dielectric constant of the neat PDMS. Due to the 2-D structure of GO or rGO sheets, they form a micro-capacitor in the polymer matrix where two layers of GO sheets form a sandwich-like structure with a thin layer of insulating polymer in between them. These micro-capacitors can align themselves under the influence of an AC field which contributes to the higher value of the dielectric constant of the PDMS-based composites compared to neat PDMS [145]. The interfacial polarization also occurs in the composites due to the difference in the electrical conductivity of nanofillers and insulating elastomer [145, 146].

The \mathcal{E}' of the PDMS composites is increasing with the wt% of the nanofillers due to the increase in the number of nano or micro capacitors and decreases when the distance between the adjacent nanofillers increases [73]. Therefore, the dielectric constants of the PDMS composites are increasing with the wt% of the nanofillers as shown in Fig. 4.3 (a-f). However, the dielectric constants of the Ag_rGO/PDMS sample are showing a sudden decrease from 10Hz frequency. It is also observed that the dielectric constants of rGO/PDMS and Ag_SWCNT/PDMS composites are showing a decreasing trend from the low (1Hz) to high (1 kHz) AC frequency. The fluctuation of the AC field is slow at low frequency. Therefore, at low AC frequency such as at 1Hz, it is easy for the micro capacitors to align completely along the direction of the AC field in the polymer matrix as they get sufficient time for polarization. The orientation of a large number of dipoles ultimately increases the dielectric permittivity of the PDMS composite material at a low AC frequency such as 1Hz [42, 147]. However, the fluctuation of the AC field is very fast at a higher AC frequency. The decrease in the dielectric constant of the PDMS composites in the high-frequency region such as 1 kHz is because of the lower rate of separation of charges than the rate of change in AC frequency [148]. That means the polarization or orientation of the dipoles is unable to follow the rapid variation of the AC field in the high frequency and the relaxation in the polarization leads to the decrease in the dielectric constant of the polymer composites [149].

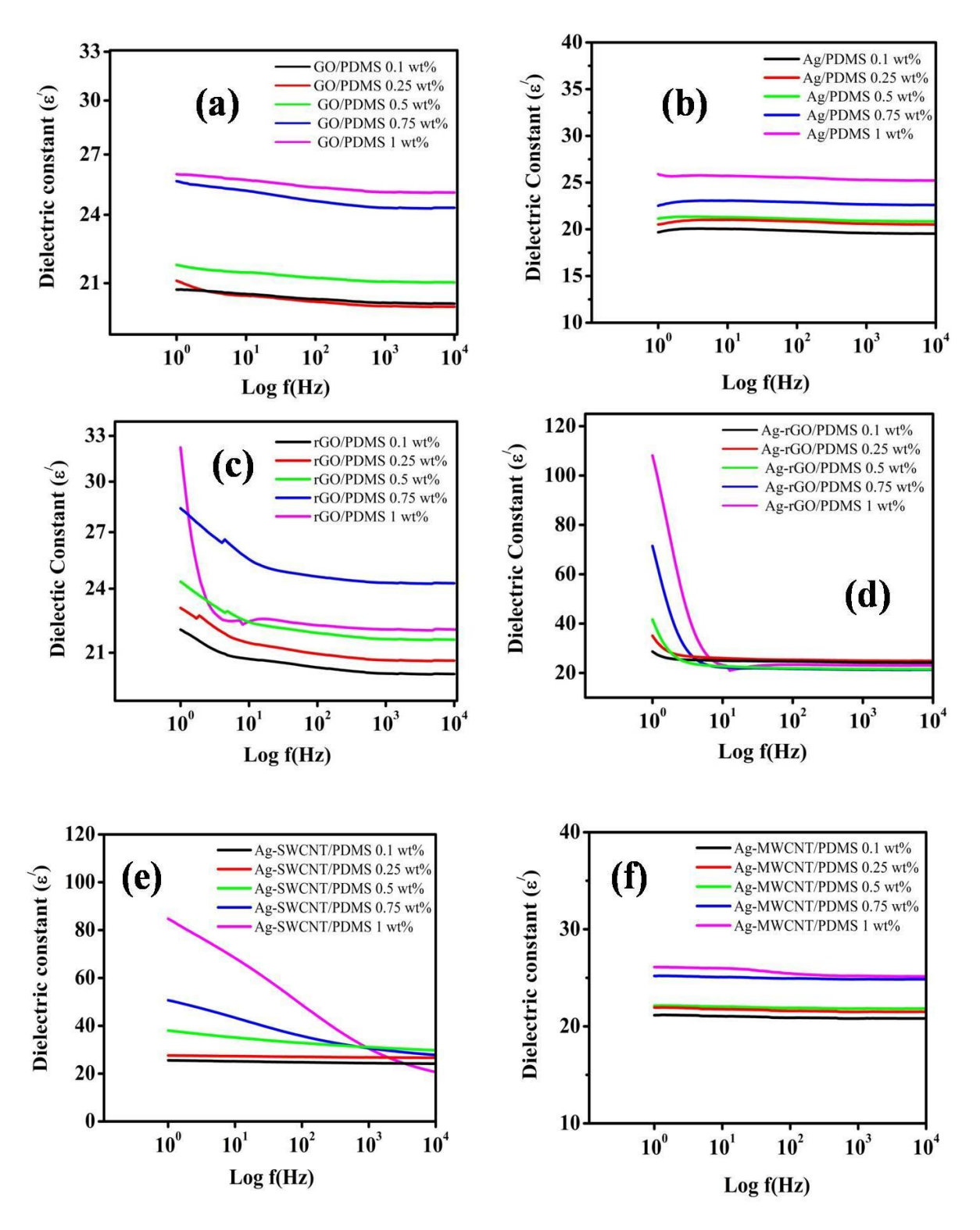


Fig. 4.3 Dielectric constant of (a) GO/PDMS, (b) Ag/PDMS, (c) rGO/PDMS, (d) Ag_rGO/PDMS, (e) Ag_SWCNT/PDMS and (f) Ag_MWCNT/PDMS flexible polymer composites with different wt% of nanofillers respectively.

The dielectric constants of the PDMS composite samples are listed in table 4.1. The comparison of dielectric permittivity of PDMS nanocomposites with different wt% of nanofillers in 1Hz and 10Hz frequency is shown in Fig. 4.4 (a-b) and the graphical

representation of dielectric permittivity of PDMS composites with 1wt% of nanofillers at 1 Hz and 1 kHz AC frequency is shown in Fig. 4.4 (c-d). The \mathcal{E}' of the Ag_rGO/PDMS sample is increasing with the wt% of nanofillers in the 1 Hz frequency which is observed in Fig. 4.3 (d) and Fig. 4.4 (a-b) respectively. But, a sudden decrease in the \mathcal{E}' values of the composite samples is seen from 10 Hz frequency onwards.

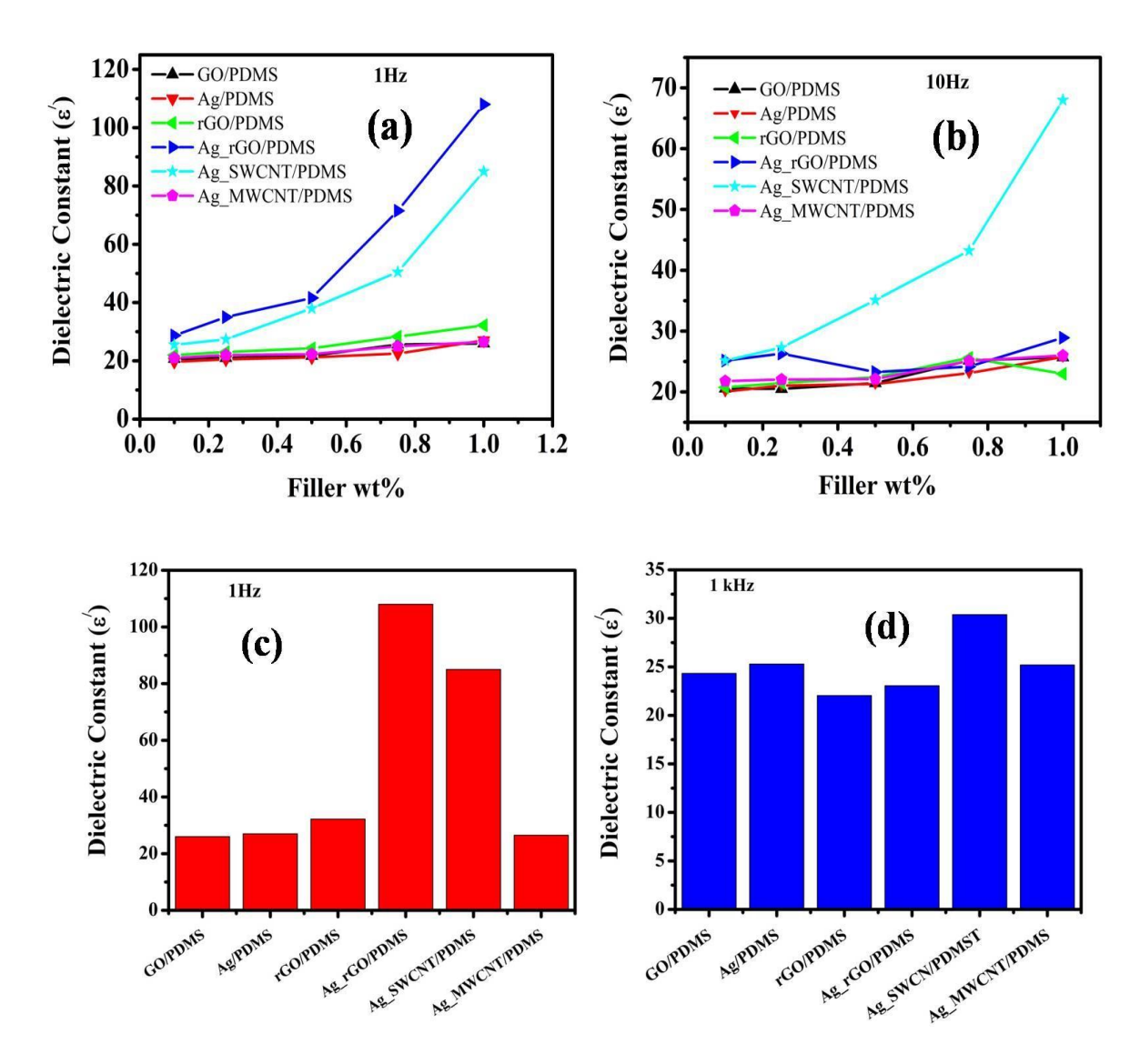


Fig. 4.4 (a-b) Comparison of dielectric permittivity of PDMS nanocomposites with different wt% of nanofillers at 1Hz and 10Hz frequency and (c-d) Graphical representation of dielectric permittivity of PDMS nanocomposites with 1wt% of nanofillers at 1 Hz and 1kHz AC frequency respectively.

It is also observed that the rGO/PDMS, Ag_rGO/PDMS, and Ag_SWCNT/PDMS composites (1wt%) are showing nearly the same value of dielectric constant (25-30) in 1 kHz AC frequency which is nearly the same as the dielectric constant of GO/PDMS, Ag/PDMS, and Ag_MWCNT/PDMS composites which are presented in Fig. 4.4 (d).

Table 4.1: Dielectric constant and loss factor of PDMS-Nnaofiller-based composites.

Sample	Nanofiller wt%	Dielectric Constant (E')	Dielectric loss (Tanδ)
PDMS		4.5	(2)
GO/PDMS	0.1	20.7	0.029
GO/PDMS	0.25	21	0.05
GO/PDMS	0.5	21.7	0.06
GO/PDMS	0.75	25.6	0.09
GO/PDMS	1	26	0.095
Ag/PDMS	0.1	19.7	0.066
Ag/PDMS	0.25	20.5	0.116
Ag/PDMS	0.5	21.2	0.163
Ag/PDMS	0.75	22.5	0.31
Ag/PDMS	1	26	0.404
rGO/PDMS	0.1	22	0.180
rGO/PDMS	0.25	23	0.182
rGO/PDMS	0.5	24.3	0.210
rGO/PDMS	0.75	28.3	0.284
rGO/PDMS	1	32.2	1.112
Ag_rGO/PDMS	0.1	28.7	0.559
Ag_rGO/PDMS	0.25	35	0.769
Ag_rGO/PDMS	0.5	41.6	0.915
Ag_rGO/PDMS	0.75	71.5	1
Ag_rGO/PDMS	1	108	0.985
Ag_SWCNT/PDMS	0.1	25.5	0.0187
Ag_SWCNT/PDMS	0.25	27.4	0.0163
Ag_SWCNT/PDMS	0.5	38	0.0584
Ag_SWCNT/PDMS	0.75	50.5	0.1556
Ag_SWCNT/PDMS	1	85	0.1556
Ag_MWCNT/PDMS	0.1	21	0.0085
Ag_MWCNT/PDMS	0.25	22	0.0044
Ag_MWCNT/PDMS	0.5	22.3	0.0068
Ag_MWCNT/PDMS	0.75	25	0.0044
Ag_MWCNT/PDMS	1	26	0.0029

The dielectric behavior of PDMS composites can be understood from two perspectives.

(a) Role of different types of nano-filler materials

The GO/PDMS, Ag/PDMS, and Ag_MWCNT/PDMS composites are showing lesser improvement in the dielectric permittivity than the other PDMS composite samples. One of the reasons for the lower value of the dielectric constant of GO/PDMS, Ag/PDMS, and Ag_MWCNT/PDMS samples is due to the restacking of the GO sheets and agglomeration of the MWCNTS, as well as of the AgNPs in the polymer matrix. The lower \mathcal{E}' values of the GO/PDMS-based composites are primarily due to the insulating nature of GO where the oxygenated functional groups are present and agglomeration as shown in Fig. 4.5 (a).

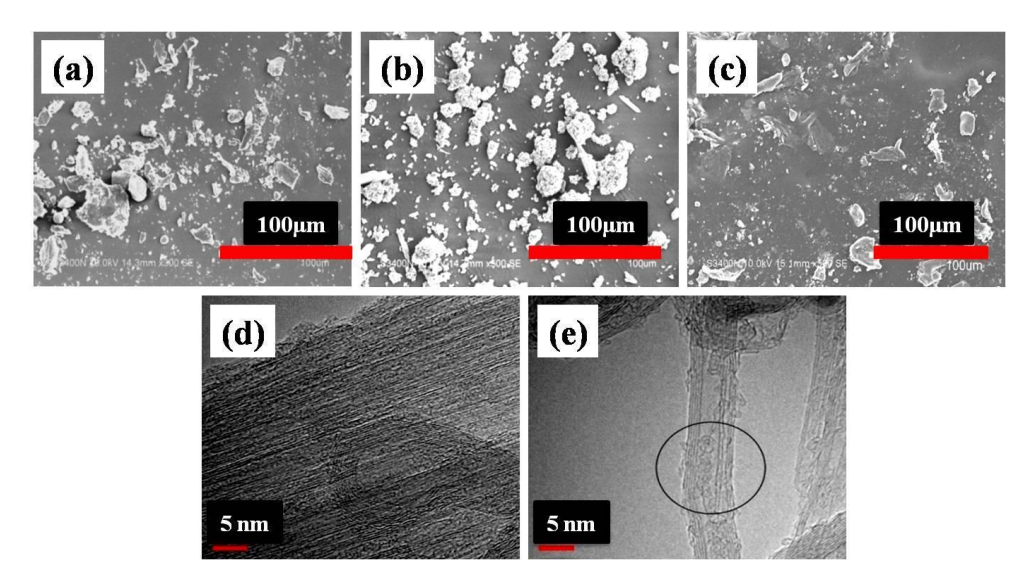


Fig. 4.5 FESEM image of 1 wt% (a) GO/PDMS, (b) Ag/PDMS and (c) Ag_rGO/PDMS nanocomposites and (d) TEM image of SWCNT and (e) MWCNT nanofillers respectively.

The agglomeration of AgNPs in the PDMS matrix is depicted in Fig. 4.5 (b) and that is the reason for the lower value of the dielectric constant of Ag/PDMS nanocomposites. In addition to agglomeration, the amorphous phase present in the MWCNTs can lower the dielectric constant of Ag_MWCNT/DMS nanocomposites as shown in the TEM image (Fig. 4.5 (e)). Hence, in the Ag_MWCNT/DMS composites, the AgNPs have a higher contribution to the dielectric constant than the MWCNTs.

The schematic representation of the distribution of nano-fillers in the PDMS matrix is shown in Fig. 4.6. The rGO retains some amount of sp² structure when reduced by chemical reduction due to the removal of oxygenated functional groups. Therefore the ions in the rGO lead to the formation of more dipoles and hence possess better dielectric properties compared to GO. Therefore, the dielectric constants of rGO/PDMS composites are higher than all other

GO/PDMS composites. The distribution of Ag_rGO nanofiller in the Ag_rGO/PDMS composites is better than the distribution of nanofillers in the GO/PDMS, Ag/PDMS, and rGO/PDMS composites as shown in Fig. 4.5 (c). The planner 2D structure of rGO and the presence of AgNPs lead to the formation of a larger number of micro-capacitors (like parallel plate capacitors) with unbound ions on both sides in the low-frequency region. Besides, the AgNPs are distributed between the rGO flakes that improve the dielectric properties of Ag_rGO/PDMS composites by electron transfer from the AgNPs to rGO in the PDMS matrix as shown in Fig. 4.6 [111, 148]. Therefore the Ag_rGO/PDMS composites are exhibiting better improvement in dielectric properties than the other samples at 1Hz AC frequency with the increase of nanofiller wt%. Therefore, the synergistic effect between rGO and AgNPs leads to the improvement in dielectric permittivity in 1 Hz AC frequency [113]. However, at 10 Hz AC frequency sudden charge migration occurs and beyond 10Hz frequency, the relaxation of the dipole polarization occurs. It is reported that the uniform distribution of AgNPs on the surface of rGO synthesized by the in-situ reduction process improves the dielectric permittivity of polymer composites [148]. In this work, the AgNPs were not grown by the in-situ synthesis method on the rGO surfaces during the chemical reduction of GO. But, commercial AgNPs were added during the chemical reduction of GO. Therefore, the AgNPs were not uniformly distributed on the surface of rGO sheets. Thus, they are sitting in between the rGO flakes in the form of clusters and weakly attached to the rGO surfaces. Therefore, as the AC frequency increases from 1Hz to 10Hz, the charge migration occurs, and charge transfer from AgNPs to rGO surfaces decreases. From 10 Hz AC frequency onwards the dielectric constant decreases due to relaxation of ions and hence, the Ag_rGO/PDMS composites are showing the same dielectric constant as the other PDMS composites in the higher frequency region.

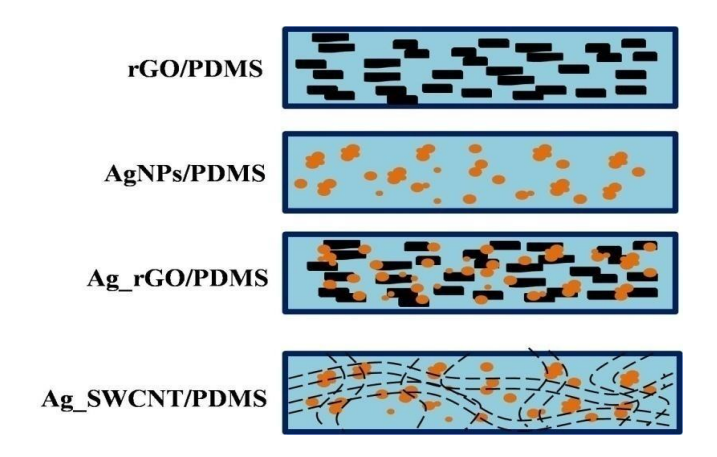


Fig. 4.6 Schematic illustration of the distribution of nanofillers in the PDMS-Nanofiller-based composites.

A similar synergistic effect and electron transfer between AgNPs and SWCNT enhance the dielectric constant of Ag_SWCNT/PDMS composites. Besides, SWCNTs do not have an amorphous phase similar to MWCNTs as shown in Fig. 4.5 (d). The dielectric constant of Ag_SWCNT/PDMS composites is not showing a sudden decrease which is observed for Ag_rGO/PDMS composites but decreases slowly up to 10³ Hz. The electron transfer mechanism is different for 2D rGO sheets and 1D SWCNTs and even when the attachment between the CNTs and AgNPs are not strong they are still bounded by the tanged forest of 1D CNTs. Therefore, sudden relaxation of ions does not occur for the CNTs. Although the dielectric constants of rGO/PDMS and Ag_SWCNT/PDMS composites increase with the wt% of nanofillers in the lower AC frequency region due to interfacial polarization of the large numbers of dipoles, they are not able to rotate rapidly with the rapid change in frequency of oscillation of the high AC frequency. Therefore a lag between the frequencies of the applied AC field and oscillating dipoles hampers the polarization and the dielectric constant decreases due to the relaxation and movement of free ions within the sample [147]. Hence, the dielectric constant of the rGO/PDMS, and Ag_SWCNT/PDMS samples decreases from 1 Hz to 1 kHz and even with higher wt% of nanofillers. The dielectric constant of the 1 wt% Ag_SWCNT/PDMS samples at 1 kHz AC frequency is the highest (30). From Fig. 4.3 (c-d), and Fig. 4.4 (a-b), it is observed that the dielectric constants of the GO/PDMS, Ag/PDMS, and Ag_MWCNT/PDMS composites are maintaining nearly constant values from 1 Hz to 1 kHz frequency. The availability of free charge or ions in GO/PDMS, Ag/PDMS, and Ag_MWCNT/PDMS samples are lesser than the other PDMS composite samples due to the insulating nature and agglomeration of GO, amorphous nature of MWCNTs, and agglomeration of AgNPs. Therefore, the dipole orientations, charge migration, and relaxation of the ions are lesser in the case of the GO/PDMS, Ag/PDMS, and Ag_MWCNT/PDMS composites than the other PDMS composite samples. Hence, they are showing lesser improvement and constant variation of dielectric constant in both the high and low AC frequency region.

(b) Role of different wt% of nano-fillers

The dielectric constant of all the PDMS-based composites increases in the 1Hz frequency with the increase of wt% of nanofillers in the PDMS matrix due to the formation of more numbers of dipoles. It is observed from Fig. 4.4 (a) that the dielectric constant of the rGO/PDMS, Ag_rGO/PDMS, and Ag_SWCNT/PDMS composites are showing an increasing trend with the increase in the wt% of nanofillers in 1Hz frequency. However, the same

increasing trend is not observed for the GO/PDMS, Ag/PDMS, and Ag_MWCNT/PDMS samples which confirm that the nanofillers are not able to provide sufficient ions to form more dipoles to enhance the dielectric constant. Hence, the GO/PDMS, Ag/PDMS, and Ag_MWCNT/PDMS samples are showing poor improvement in the dielectric constant compared to the other samples.

4.3.2 Analysis of dielectric loss (Tanδ) of PDMS-Nanofiller composites

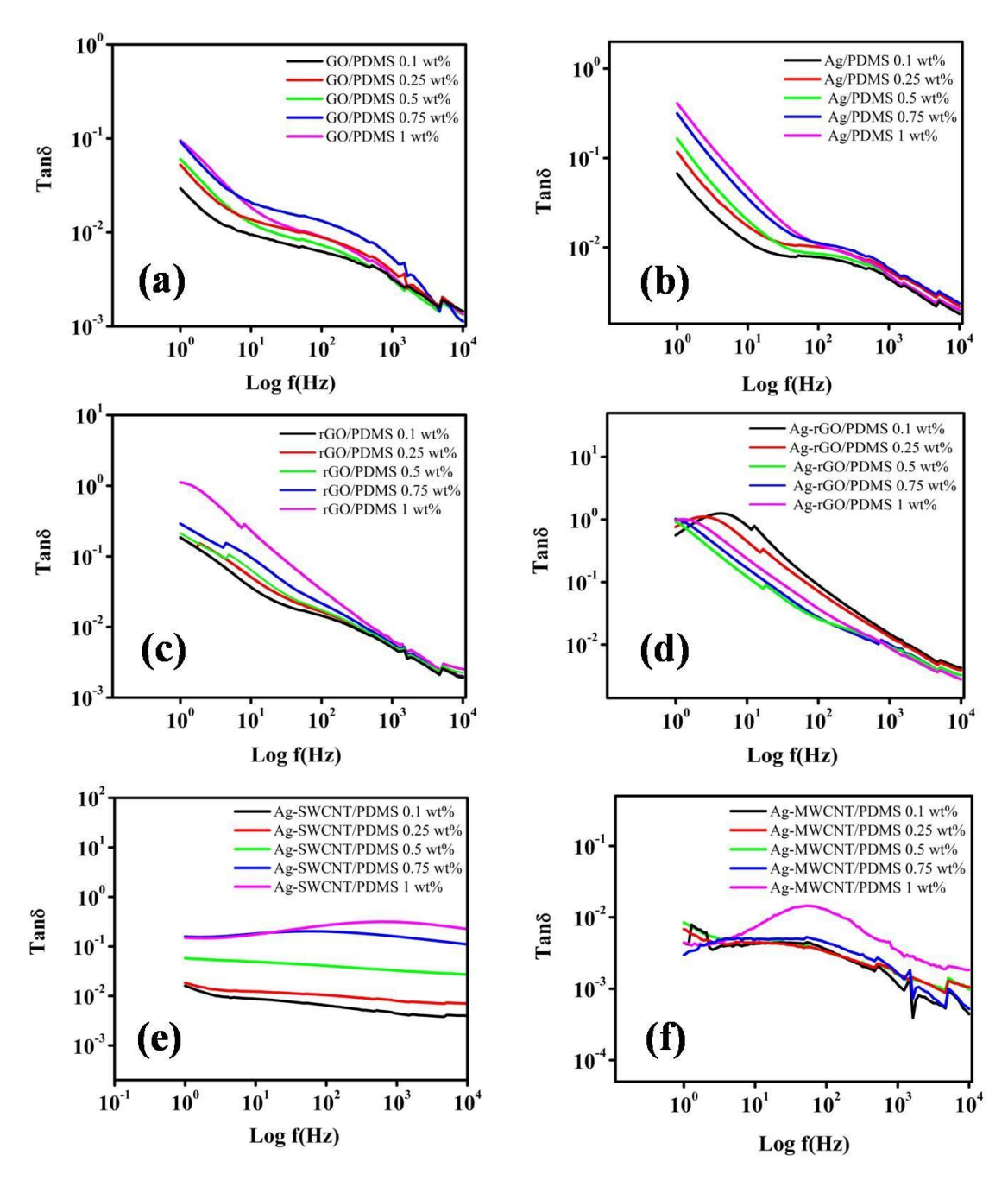


Fig. 4.7 Dielectric loss of (a) GO/PDMS, (b) Ag/PDMS, (c) rRGO/PDMS, (d) Ag_rGO/PDMS, (e) Ag_SWCNT/PDMS and (f) Ag_MWCNT/PDMS flexible polymer composites with different wt% respectively.

The dielectric loss factor of the GO/PDMS, Ag/PDMS, rGO/PDMS, Ag_rGO/PDMS, Ag_SWCNT/PDMS, and Ag_MWCNT/PDMS flexible polymer composites are shown in Fig. 4.7 (a-f). Similar to dielectric permittivity, the dielectric loss factor of the PDMS composites is also showing a decreasing trend from the lower to the higher region of AC frequency as shown in Fig. 4.7. As mentioned earlier in the low-frequency region (1 Hz), the higher \mathcal{E}' and $Tan\delta$ values are attributed to the increase in polar groups to form the microcapacitors and the accumulation of unbound charges on both sides of the polymer-filler interfaces. The accumulation of unbound charges leads to the formation of large dipoles at the interface of the sample causing interfacial polarization [150]. The charge carriers accumulate between the top surfaces of the electrodes in the presence of an electric field that is referred to as Maxwell-Wagner-Sillars (MWS) polarization [11, 65, 151]. In the low-frequency region, dielectric loss occurs due to the charge motion within the material by hopping or tunneling under an AC field [147]. However, in the high-frequency region, the dielectric loss decreases due to the relaxation of the radical ions because they are no longer able to follow the rapid alteration of the high AC field.

(a) Role of different types of nano-filler materials

The dielectric loss factors of the PDMS composites are given in table 4.1. The comparison of dielectric loss factor of PDMS composite samples with different wt% of nanofillers in 1Hz and 10Hz frequency is shown in Fig. 4.8 (a-b) and the graphical representation of dielectric loss factor of PDMS composites with 1wt% of nanofillers at 1 Hz and 1 kHz AC frequency is shown in Fig. 4.8 (c-d). From the results, it is observed that rGO/PDMS and Ag_rGO/PDMS composites are showing the highest loss factor (0.5 to 1) in 1 Hz AC frequency with the increase of wt% of nanofillers as shown in Fig. 4.8 (a). However, the dielectric loss factor of Ag_rGO/PDMS samples is showing a sudden increase from 1Hz to 10Hz frequency as shown in Fig. 4.8 (b). In the dielectric constant plot of Ag_rGO/PDMS samples, a sudden decrease was observed at 10 Hz frequency. Therefore, it is certain that from 1Hz to 10 Hz frequency huge charge migration occurs in the Ag_rGO/PDMS samples with increasing wt% of nanofillers which increases the loss factor. But the dielectric constant of the samples decreases as the polarization of the dipoles decreases. After charge migration, the relaxation of the ions in the frequency beyond 10 Hz decreases both dielectric constant and loss factor in the Ag_rGO/PDMS samples. The Ag_SWCNT/PDMS composites are maintaining a constant variation of dielectric loss factor in both low and high-frequency regions as shown in Fig. 4.7 (e). However, the loss factors of the Ag_SWCNT/PDMS composites are lower than the

rGO/PDMS and Ag_rGO/PDMS composites at 1 Hz AC frequency. The dielectric loss factor of Ag_SWCNT/PDMS samples at 1 Hz AC frequency ranges from 0.016 to 0.15.

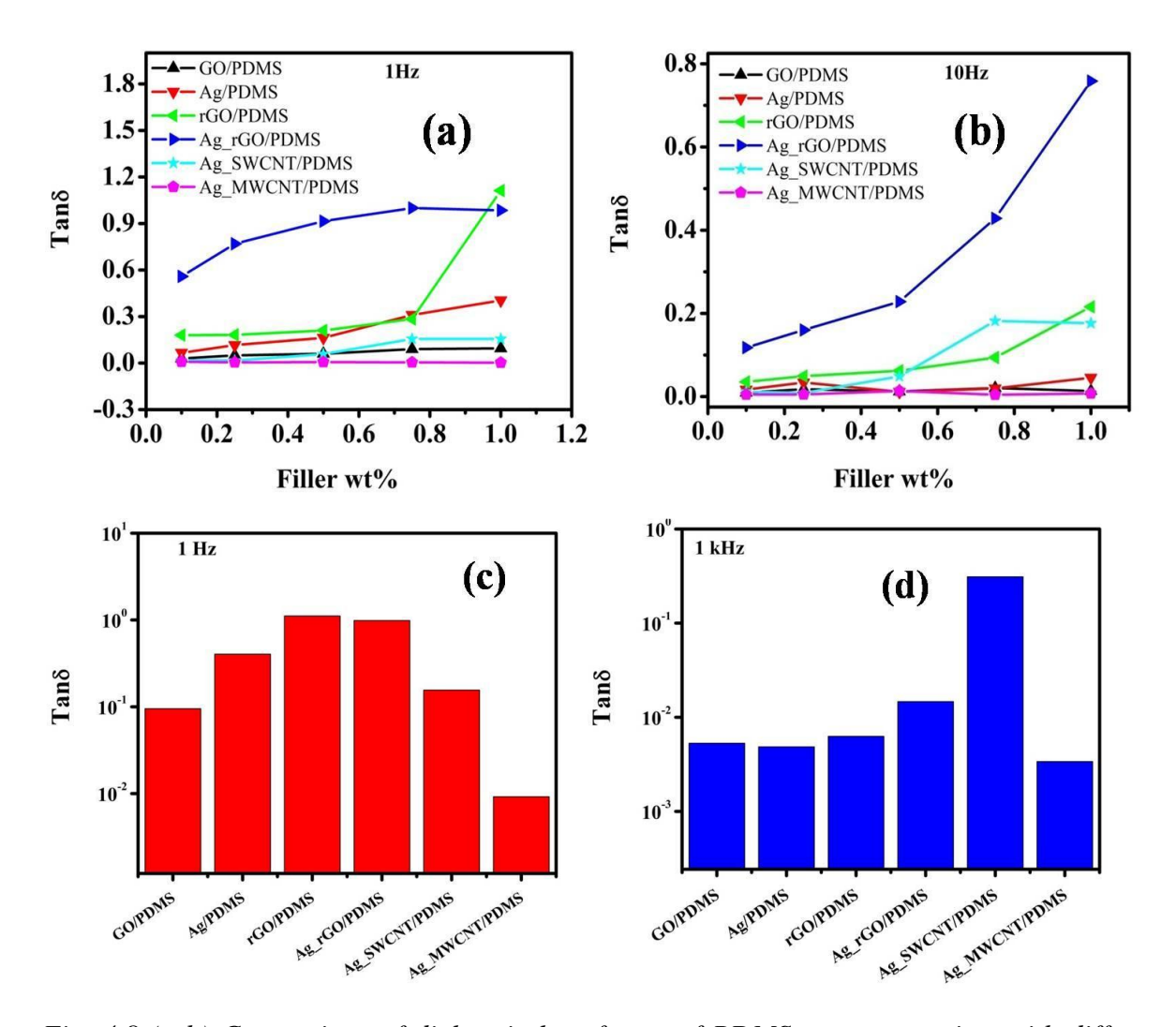


Fig. 4.8 (a-b) Comparison of dielectric loss factor of PDMS nanocomposites with different wt% of nanofillers at 1Hz and 10Hz frequency and (c-d) Graphical representation of dielectric loss factor of PDMS nanocomposites with 1wt% of nanofillers at 1 Hz and 1 kHz AC frequency respectively.

Moreover, the dielectric loss factor of 1wt% Ag_SWCNT/PDMS samples at 1 kHz AC frequency is the highest which is 0.31 as shown in Fig. 4.8 (d). It was observed in the dielectric constant plot of Ag_SWCNT/PDMS samples that the dielectric constant decreases slowly from the higher to lower frequency region (1Hz to 10³Hz). Therefore, Ag_SWCNT/PDMS samples can maintain polarization in the higher frequency region up to 10³Hz. The possible reason may be the distribution of AgNPs in the SWCNTs is random and they are closely bound by the tangled CNTs forest which prevents some of the CNTs from tangling up and minimizing the contact between them. Also, as mentioned earlier the electron transfer mechanism between the CNTs and AgNPs in the Ag_SWCNT nanofiller is

different from the Ag_rGO nanofillers because in the Ag_rGO nanofillers the AgNPs are sitting on the surface of rGO while they are tangled between the 1D CNTs. Thus, the low frequency is not sufficient for free charge migration through tunneling in the CNTs which reduces the dielectric loss, but at the same time increases the dielectric permittivity due to dipole polarization. Thus, the dielectric loss factors of the Ag_SWCNT/PDMS composites are low although the dielectric permittivity is high at 1 Hz frequency. However, in the highfrequency region charge migration occurs in the Ag_SWCNT/PDMS composite which increases the dielectric loss. The Ag_PDMS, GO/PDMS, and Ag_MWCNT/PDMS composites are also showing lower dielectric loss factors than rGO/PDMS-based, and Ag_rGO/PDMS-based, composites at 1Hz frequency. Also, the dielectric loss factor decreases from the 1Hz to 1 kHz frequency. In the Ag_PDMS, Ag_MWCNT/PDMS, and GO/PDMS composites the lower value of loss factor is because the availability of free charges or ions is very less for charge migration due to restacking of insulating of GO, MWCNTs, and agglomeration of AgNPs in the polymer matrix. However, in 1 kHz AC frequency, the \mathcal{E}' of all the PDMS-based composites are nearly the same ($\mathcal{E}'=20-30$) due to residual dipole charges in the samples but the loss factor decreases due to the absence of free charges for charge migration [148].

(b) Role of different wt% of nano-fillers

The dipole polarization increases with the increase of wt% of nanofillers due to the formation of a large number of micro or nano capacitors which ultimately increases the charge migration through hopping or tunneling mechanism at 1Hz frequency. The comparative plot of dielectric loss for all PDMS nanocomposites with the increase in nanofiller wt% at 1Hz frequency is shown in Fig. 4.7(a). It is observed that the dielectric loss of GO/PDMS, Ag/PDMS, rGO/PDMS, Ag_rGO/PDMS, and Ag_SWCNT/PDMS-based composites increase with the increase of nanofiller's wt% due to the increase in charge migration of the dipole charges. In the higher frequency region, the dielectric loss factor decreases due to the relaxation of dipole polarization irrespective of wt% of nanofillers. The Ag_MWCNT/PDMS composite exhibits the lowest loss factor of 0.004 in 1 Hz frequency. This again confirms that along with agglomeration, the amorphous phase present in the MWCNTs decreases the \mathcal{E}' values and lowers the $Tan\delta$ values. The optimized value of the \mathcal{E}' and $Tan\delta$ is found for 1 wt% Ag_rGO/PDMS ($\mathcal{E}' = 108$, $Tan\delta = 0.98$) and Ag_SWCNT/PDMS ($\mathcal{E}' = 85$, $Tan\delta = 0.15$) composites.

4.3.3 Analysis of AC conductivity (σ_{ac}) of PDMS-Nanofiller composites

The AC conductivity plots of PDMS composites containing five different wt% of GO, AgNPs, rGO, Ag_rGO, Ag_SWCNT, and Ag_MWCNT nanofillers is shown in Fig. 4.9 (a-f).

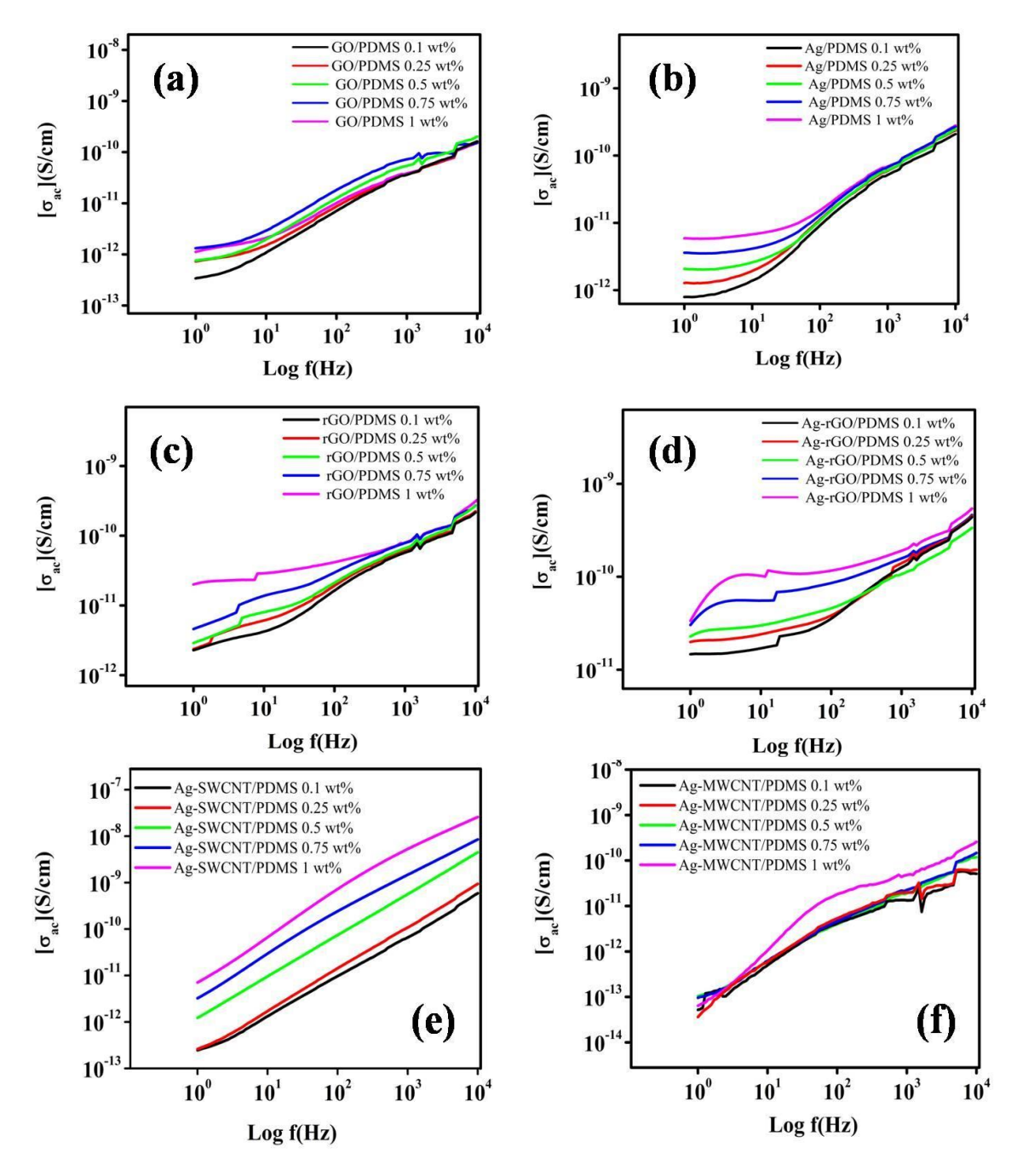


Fig. 4.9 AC conductivity of different wt% of (a) GO/PDMS, (b) Ag/PDMS, (c) rGO/PDMS, (d) Ag_rGO/PDMS, (e) Ag_SWCNT/PDMS and (f) Ag_MWCNT/PDMS flexible polymer composites respectively.

The AC conductivities (σ_{ac}) of Ag/PDMS, rGO/PDMS, Ag_rGO/PDMS-based, and Ag_SWCNT/PDMS-based composites are higher than the AC conductivity of GO/PDMS and Ag_MWCNT/PDMS composites which is observed in Fig. 4.9 (a-f). The AC

conductivity of the GO/PDMS composites at 1 Hz AC frequency is in the range from ~ 10^{-13} to 10^{-12} S/cm as shown in Fig. 4.9 (a). Similarly, the AC conductivity of Ag/PDMS and rGO/PDMS composites at 1 Hz frequency is in the range from ~ 10^{-12} to 10^{-11} S/cm. The AC conductivity of Ag_rGO/PDMS composites at 1 Hz frequency is higher than the other PDMS composites which are ~ 10^{-11} to 10^{-10} S/cm. The Ag_MWCNT/PDMS composites are showing the lowest value of AC conductivity which is ~ 10^{-13} to 10^{-14} S/cm. The AC conductivity of Ag_SWCNT/PDMS composites at 1 Hz frequency is ~ 10^{-13} to 10^{-11} S/cm which increases linearly from 1 Hz to 1 kHz AC frequency. It is noticed that the AC conductivity of all other PDMS composites is converging toward a single point at the AC frequency of 1 kHz and the only exception is Ag_SWCNT/PDMS composite.

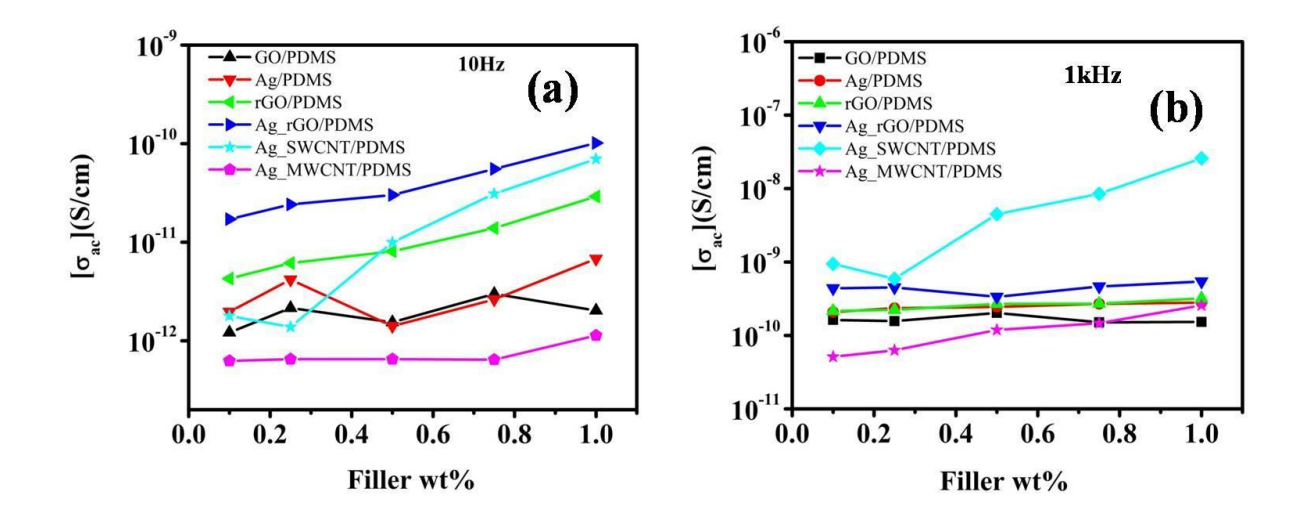


Fig.4.10 (a-b) Comparison of AC conductivity of PDMS nanocomposites with different wt% of nanofillers at 1Hz and 10Hz frequency respectively.

The σ_{ac} values of the PDMS composites increase with the increase of AC frequency from 1 Hz to 1 kHz which is observed from Fig. 4.9 (a-f). The AC conductivity and dielectric loss factor both increase due to charge migration. However, it was observed that the dielectric loss factors of the PDMS composites decreased from the low to high AC frequency region. It is observed that the increases in AC conductivity of the PDMS composites are in the range from~ 10^{-10} to 10^{-8} S/cm from 1Hz to 1 kHz frequency which is a small change. The small increase in the AC conductivities in the high AC frequency region is possibly due to the migration of some of the free charges within the samples during the relaxation of dipole polarization. The graphical representation of the comparison for AC conductivities of PDMS nanocomposites with nanofiller's wt% at 10 Hz and 1 kHz AC frequency is presented in Fig 4.10 (a-b). As mentioned earlier, the AC conductivity of the polymer composites below percolation is primarily due to the migration of charges of the nano-fillers through hopping or

tunneling mechanism which increases with the increase of AC frequency [147, 152, 153]. As the dipole charge increases upon increasing nanofiller's wt% in the elastomer matrix, more free charges migrate along the direction of the AC field through the hopping mechanism. Therefore, the AC conductivity increases with the wt% of nanofillers. The Ag_rGO/PDMS composite is showing the highest improvement in AC conductivity at 10 Hz frequency compared to the other samples as shown in Fig. 4.10(a). In the dielectric constant plot of Ag_rGO/PDMS composites, it was observed that the dielectric constants decreased suddenly at 10 Hz frequency. Similarly, the dielectric loss factors increased at 10 Hz frequency for the Ag_rGO/PDMS composites. Therefore, the increase in the AC conductivity of the Ag_rGO/PDMS composites at 10 Hz frequency proved that the charge migration through tunneling enhanced the AC conductivity, loss factor and reduced the dielectric constant of Ag_rGO/PDMS composites. In both the 1 Hz and 1 kHz frequency region, the Ag_SWCNT/PDMS composite is showing an increasing trend of AC conductivities with the increasing wt% of nanofiller which is shown in Fig 4.10(a-b). The Ag SWCNT/PDMS composite is exhibiting the highest value of AC conductivity in the 1 kHz frequency region. We have observed that the loss factor of Ag_SWCNT/PDMS composite also increases at 1 kHz AC frequency with the increase of wt% of nanofiller. Therefore, it is understood that the charge migration in the Ag_SWCNT/PDMS composites continues in the high-frequency region also.

4.6 Conclusions

The dielectric properties of the PDMS-based polymer composites such as dielectric constant (\mathcal{E}'), dielectric loss ($Tan\delta$), and AC conductivity (σ_{ac}), are investigated. The \mathcal{E}' and $Tan\delta$ values increase with the increase of wt% of the nano-fillers in the low-frequency region. Out of all the PDMS composites, the Ag_rGO/PDMS and Ag_SWCNT/PDMS composites have shown excellent improvement in the dielectric permittivity with low dielectric loss. The optimized value of dielectric properties in 1Hz frequency is obtained for PDMS composites with 1 wt% Ag_rGO ($\mathcal{E}'=108$, $Tan\delta=0.95$) and Ag_SWCNT ($\mathcal{E}'=85$, $Tan\delta=0.15$) nanofillers. The Ag_SWCNT/PDMS composites exhibited better dielectric properties from 1Hz and 1 kHz AC frequency regions than the other PDMS-based nanocomposites. Also, from the measurement of electrical (DC) properties, it was observed that the PDMS composites were showing very high resistance. It is possible to increase the dielectric constant and DC conductivity of the PDMS composites by increasing the wt% of the nanofillers. However, the process requires a large number of nanomaterials to achieve the

desired dielectric properties or electrical conductivity. The present work gives an idea about tuning the dielectric properties of the PDMS composites with low wt% of nanofiller material which can be useful for energy storage-based applications. The main challenge so far is to prevent the agglomeration of the nanofillers which can be achieved by surface functionalization of the nanomaterials. However, surface functionalization may degrade the electrical properties. Therefore, an alternative approach was adopted to fabricate PDMS and nanomaterials coated laboratory parafilm-based flexible sandwich structure which will be discussed in the next chapter.

CHAPTER 5

Demonstration of PDMS/nanomaterials coated parafilm/PDMS-based sandwich structure for strain sensing applications

5.1 Introduction

This chapter presents the fabrication of PDMS/nanomaterials-coated parafilm/PDMS-based sandwich structures and the capability of the sandwich structure to be utilized as a strain sensor for the monitoring of human movements in real-time were investigated. Instead of increasing the wt% of the nanofillers in the PDMS matrix to improve the sensing characteristics, an alternative approach was adopted where the nanomaterials were coated on the surface of a laboratory parafilm, and sandwich structure of PDMS/nanomaterials coated parafilm/PDMS was fabricated for testing human motion detection. The relative resistance change ($\Delta R/R_0$) with the applied strain and the corresponding Gauge factors (GF) of the PDMS/rGO-Parafilm/PDMS, sandwich structured PDMS/Ag_rGO-Parafilm/PDMS, PDMS/SWCNT-Parafilm/PDMS, PDMS/Ag_SWCNT-Parafilm/PDMS-based and flexible/stretchable and wearable strain sensors were also presented in this chapter. The role of Ag NPs which leads to the improvement in the GF of the strain sensors and the mechanism is also described in this chapter. The strain sensors are useful to detect the motions of different human body parts that include bending of fingers in real-time which is also demonstrated in this chapter.

5.2 Fabrication of PDMS/rGO-Parafilm/PDMS, PDMS/Ag_rGO-Parafilm/PDMS, PDMS/SWCNT-Parafilm/PDMS and PDMS/Ag_SWCNT-Parafilm/PDMS flexible sandwich structure

Parafilm was chosen because the blend of polyolefin is non-toxic, stretchable, and melts during heating and after cooling down retains the earlier form. Therefore, it is expected that after coating the nanomaterials, the wax-like surface will provide good adhesion and the nanomaterials will be embedded into the film during the heating and cooling cycle forming a conductive network. Therefore, we assumed that the parafilm coated with nanomaterial will act as the sensing part and the PDMS substrates on both sides will provide flexibility to the sandwich structure while stretching and releasing cycles. The fabrication process of PDMS/rGO-Parafilm/PDMS, PDMS/Ag_rGO-Parafilm/PDMS, PDMS/SWCNT-Parafilm/PDMS and PDMS/Ag_SWCNT-Parafilm/PDMS flexible strain sensors are shown in Fig. 5.1 and Fig. 5.2. The strain sensors were fabricated in two steps. In the first step, parafilm was coated with nanomaterials to fabricate the sensitive unit materials as shown in Fig. 5.1. For this purpose, each of the nanomaterials such as rGO, Ag_rGO, SWCNT, and Ag_SWCNT were dispersed in ethanol (10 mg/mL) by using ultrasonication for 1 hour as

discussed in chapter 2. The parafilm was cut into desired size (5cm×2cm) and dipped into the above-mentioned mixture solution for approximately 5 to 10 seconds. The parafilm coated with the sensing materials was then dried on a hot plate at 50 °C approximately for 5 to 10 minutes and then cooled down. The process was repeated 5 times. Finally, both the ends of the parafilm coated with sensing material were covered with conductive Cu tape.

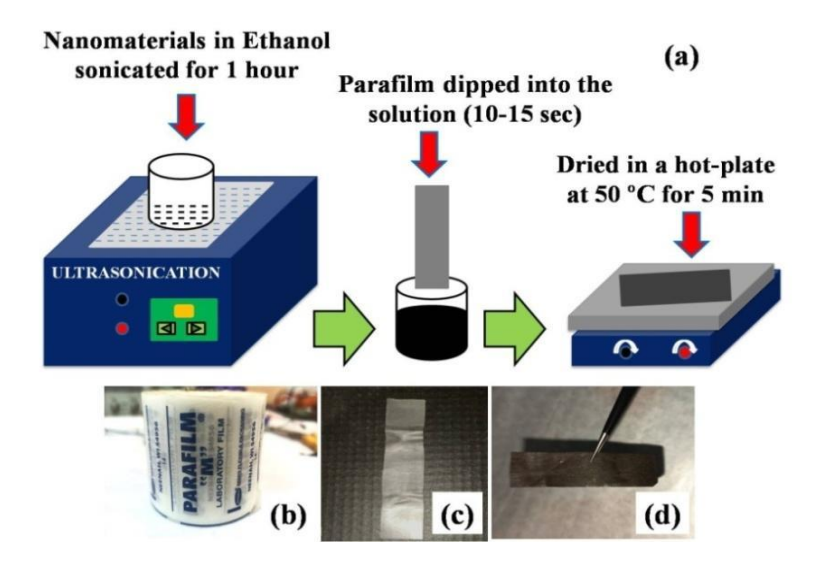


Fig. 5.1 Schematic representation of the (a) preparation of nanomaterials coated parafilm for the fabrication of strain sensor, (b-c) Parafilm used for the fabrication process, and (d) the fabricated nanomaterials coated Parafilm.

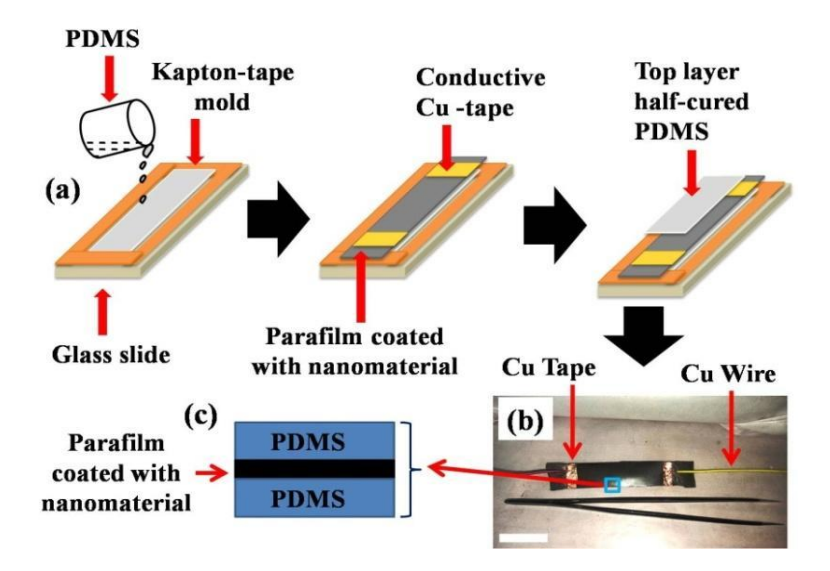


Fig. 5.2 (a) Schematic representation which shows the step-wise fabrication of sandwich structure (PDMS/nanomaterials coated parafilm/PDMS) to be used as a strain sensor (b) fabricated PDMS/nanomaterials coated parafilm/PDMS sandwich structure, and (c) schematic representing the fabricated sandwich structure.

In the second step, molds for casting PDMS were prepared with Kapton tape by using the glass slides as shown in Fig. 5.2. The PDMS prepolymer and curing agents were mixed (10:1) and degassed. The molds were filled with PDMS which was allowed to dry on a hot plate for 15 to 20 minutes at 80 °C. The nanomaterials coated parafilm was placed over the half-dried PDMS and on top of this, half-dried PDMS film was placed as shown in Fig. 5.2 (a). Two wires were connected to the portion of the nanomaterial-coated parafilm where the conductive Cu tape was attached for strain measurements. The dimension of the sandwich structure is approximately 0.15cm in thickness, 4.5 cm in length, and 1.5 cm in breadth respectively. The thickness of the fabricated sandwich structure was measured by using a digital micrometer. The fabricated sandwich structures and their dimensions are given in table 5.1.

Table 5.1 Fabricated sandwich structured PDMS/nanomaterials coated parafilm/PDMS samples.

Samples	Nanomaterials coated to Parafilm	Sandwich Structure	Dimensions (l, w, t) in cm
1	rGO	PDMS/rGO-Parafilm/PDMS	4.5, 1.5, 0.1562
2	Ag_rGO	PDMS/Ag_rGO-Parafilm/PDMS	4.5, 1.5, 0.1547
3	SWCNT	PDMS/SWCNT-Parafilm/PDMS	4.5, 1.5, 0.1534
4	Ag_SWCNT	PDMS/Ag_SWCNT-Parafilm/PDMS	4.5, 1.5, 0.1497

The cross-sectional view of the PDMS/rGO-Parafilm/PDMS, PDMS/Ag_rGO-Parafilm/PDMS, PDMS/SWCNT-Parafilm/PDMS, and PDMS/Ag_SWCNT-Parafilm/PDMS sandwich structures are shown in the FESEM images which are shown in Fig. 5.3 (a, c, e, and g) respectively. The topography of the rGO, Ag_rGO, SWCNT, and Ag_SWCNT coated parafilm is shown in Fig. 5.3 (b, d, f, and h). It is observed that the sensing materials are embedded in the parafilm forming clusters with the parafilm material which exhibits a strong interaction between the nanomaterials and parafilm. Similarly, there was good adhesion between the nanomaterials coated parafilm (blue rectangles) and PDMS which can be observed from Fig. 5.3 (b, d, f, and h) respectively.

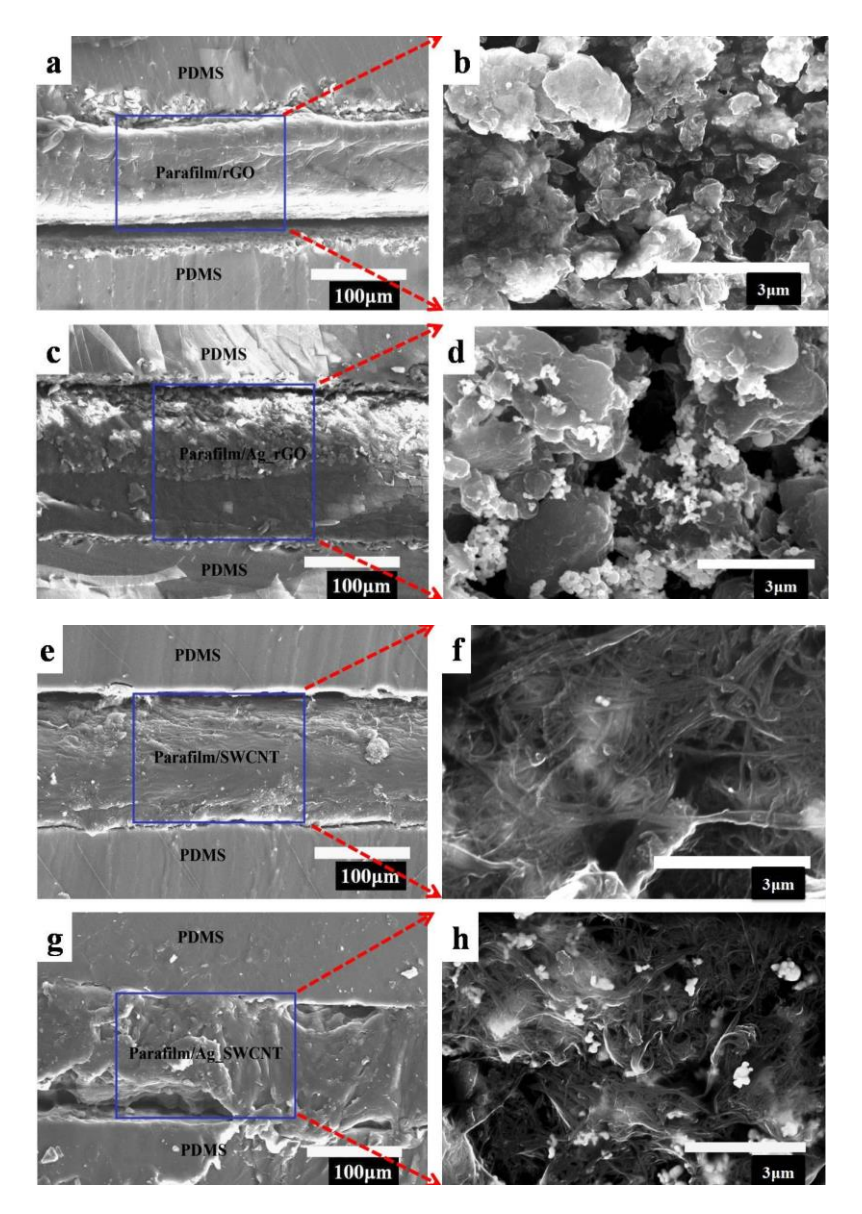


Fig. 5.3 FESEM images (cross-sectional view) of the samples (a) 1, (c) 2, (e) 3, and (g) 4 sandwich structure and (b, d, f, h) morphology of the cross-section of the samples respectively.

5.3 The electrical conductivity of the PDMS/rGO-Parafilm/PDMS, PDMS/Ag_rGO-Parafilm/PDMS, PDMS/SWCNT-Parafilm/PDMS and PDMS/Ag_SWCNT-Parafilm/PDMS sandwich structure

The *I-V* characteristics of the sandwich structures which were fabricated from PDMS and rGO-Parafilm, Ag-rGO-Parafilm, SWCNT-Parafilm, and Ag_SWCNT-Parafilm were measured by using the Agilent 34972A LXI data acquisition unit and the experimental setup is shown in Fig. 5.4. The *I-V* characteristics and DC conductivities of all four samples are shown in Fig. 5.6 (a-b). From Fig. 5.6 (a) it is found that all the samples show linear *I-V*

characteristics. The conductivities of the conductive parts of the sandwiched structures were calculated by the following equation.

$$\sigma = \frac{l}{RA}$$

Where, the symbols σ , R, l, and A represents the DC conductivity, resistance, length of the sample, and area of cross-section of the samples.

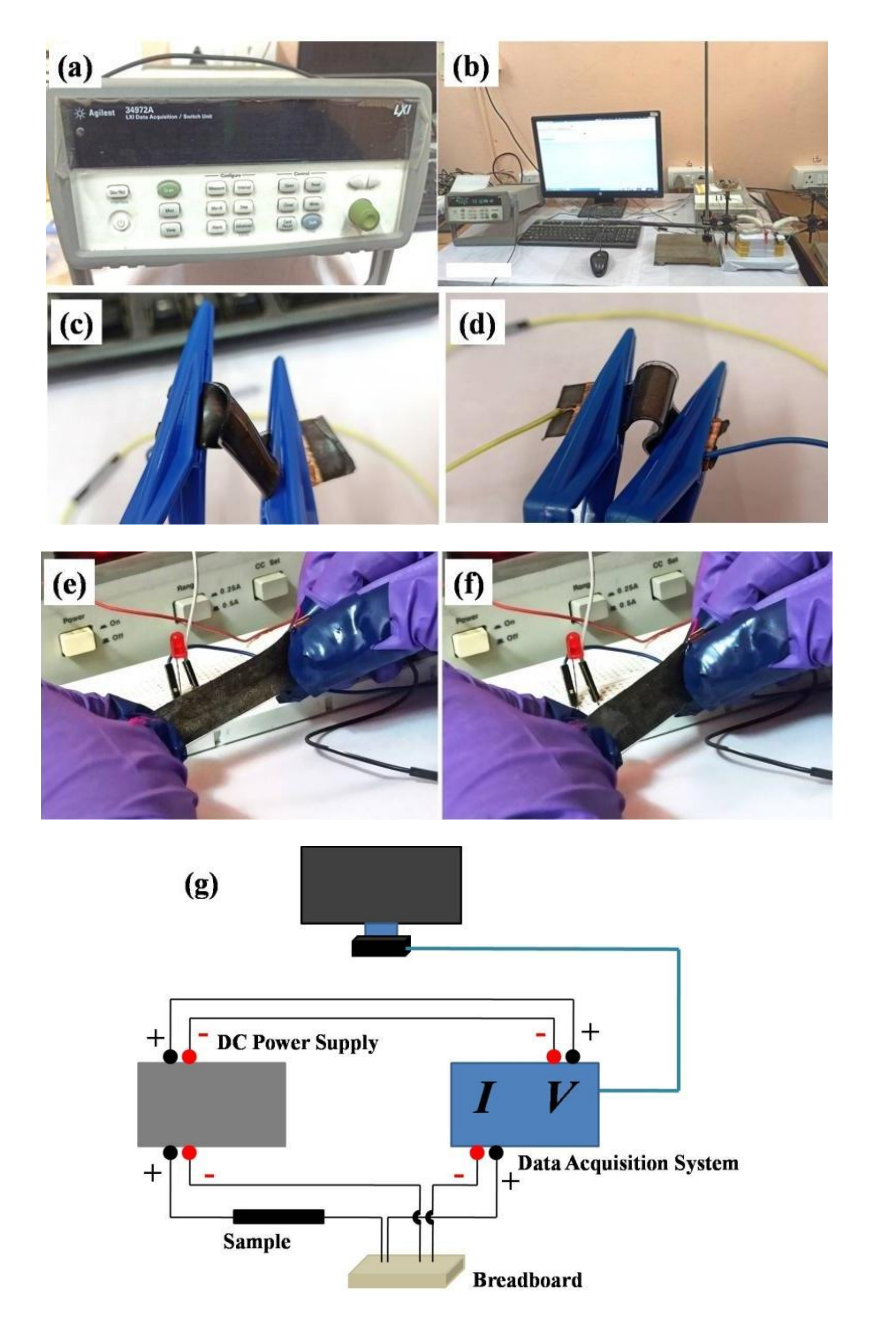


Fig. 5.4 Optical images of the (a) and (b) experimental set-up for the measurement of I-V characteristics and relative change in resistance with the applied strain, (c), (d), and (e) twisting, bending, and stretching deformation of the sandwich structures, and (f) relaxed state of the sensor. (g) The schematic diagram for the measurement of I-V characteristics.

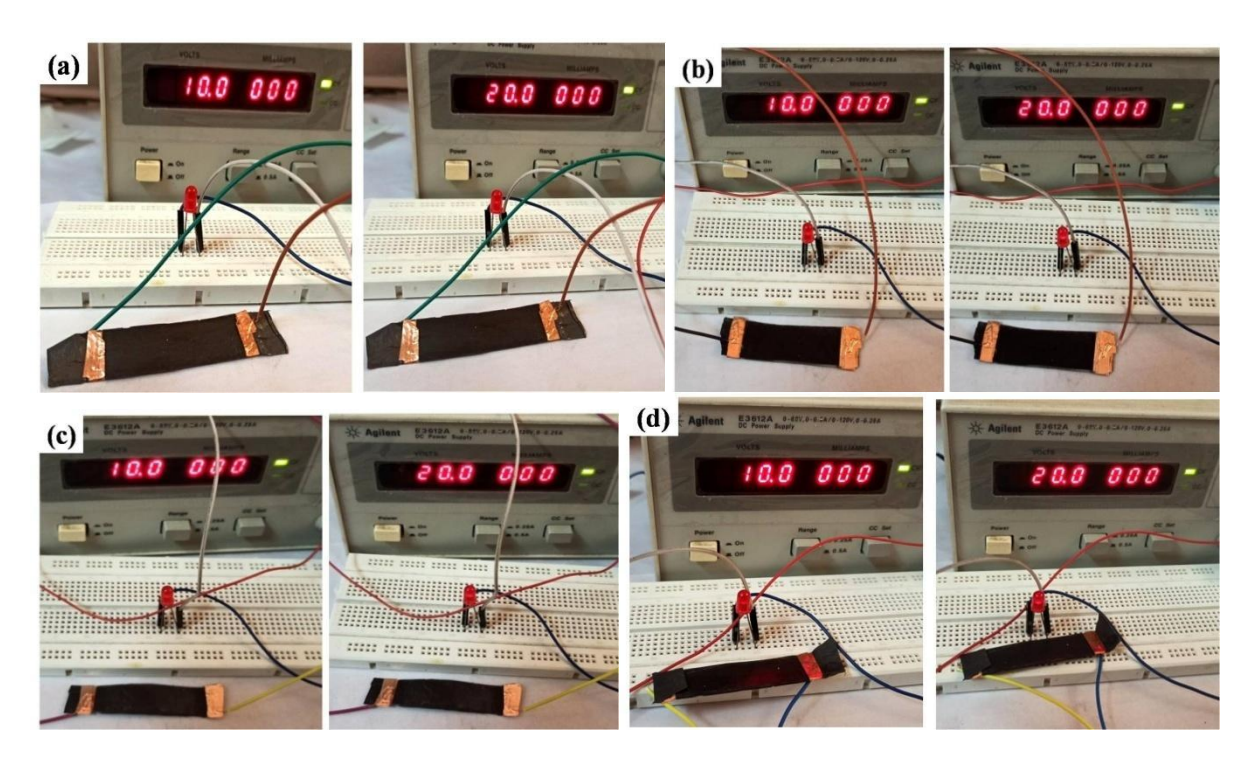


Fig. 5.5 LED testing of all the fabricated samples which indicates that at 20v, the LED glow is more for samples with higher conductivities. The LED light intensity of (b) Sample 2 is higher than (a) Sample 1 and the (d) Sample 4 LED intensity is higher than (c) Sample 3 which confirms the results obtained from IV measurements as stated above.

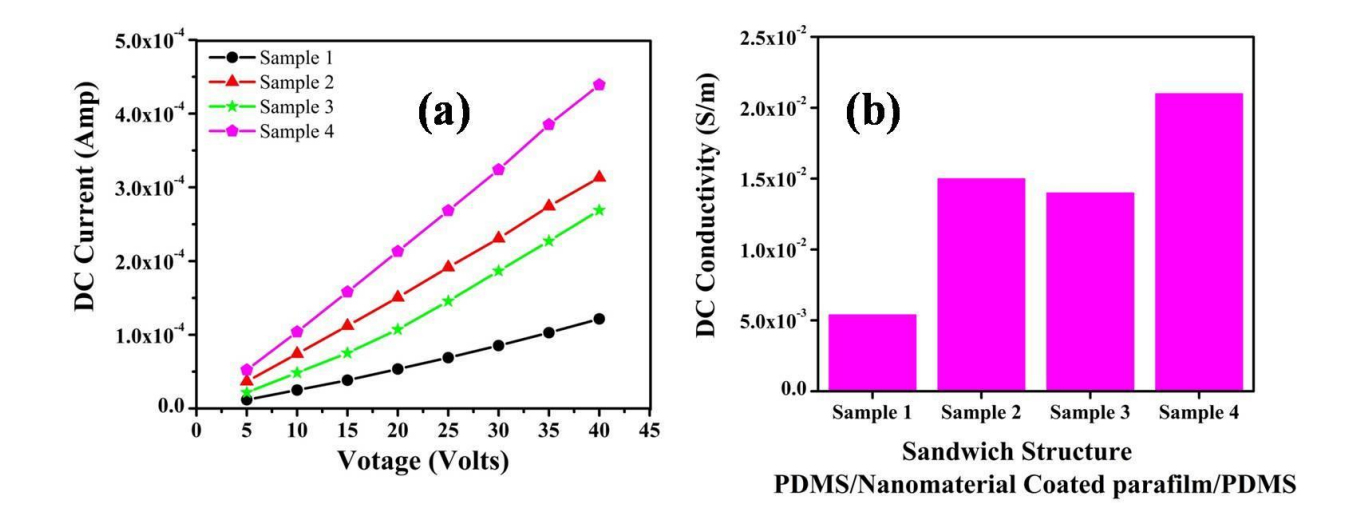


Fig. 5.6 (a) I-V characteristics curve of the sandwich structure of PDMS/Nanomaterials coated Parafilm and (b) Graphical representation of conductivities of all the samples.

The conductivities " σ " of all the samples were evaluated and shown in Fig 5.6 (b). The corresponding conductivities of the sandwich structure samples PDMS/rGO-Parafilm/PDMS, PDMS/Ag_rGO-Parafilm/PDMS, PDMS/SWCNT-Parafilm/PDMS and PDMS/Ag_SWCNT-Parafilm/PDMS the sandwich structure samples are $\sim 5.7 \times 10^{-3}$ S/m, 1.5×10^{-2} Sm⁻¹, 1.4×10^{-2} Sm⁻¹ and 2.1×10^{-2} Sm⁻¹ respectively. By comparing the results it is found that the

conductivity of the PDMS/Ag_rGO-Parafilm/PDMS is higher than the conductivity of the PDMS/rGO-Parafilm/PDMS sample. Similarly, the conductivity of the PDMS/Ag_SWCNT-Parafilm/PDMS is higher than the conductivity of the PDMS/SWCNT-Parafilm/PDMS sample. The results suggest that the Ag NPs added to rGO and CNTs improve the conductivity of the fabricated samples. Thus, the AgNPs acts as an electrical bridge between the rGO and SWCNTs by providing conductive paths and thus improving the conductivity [111].

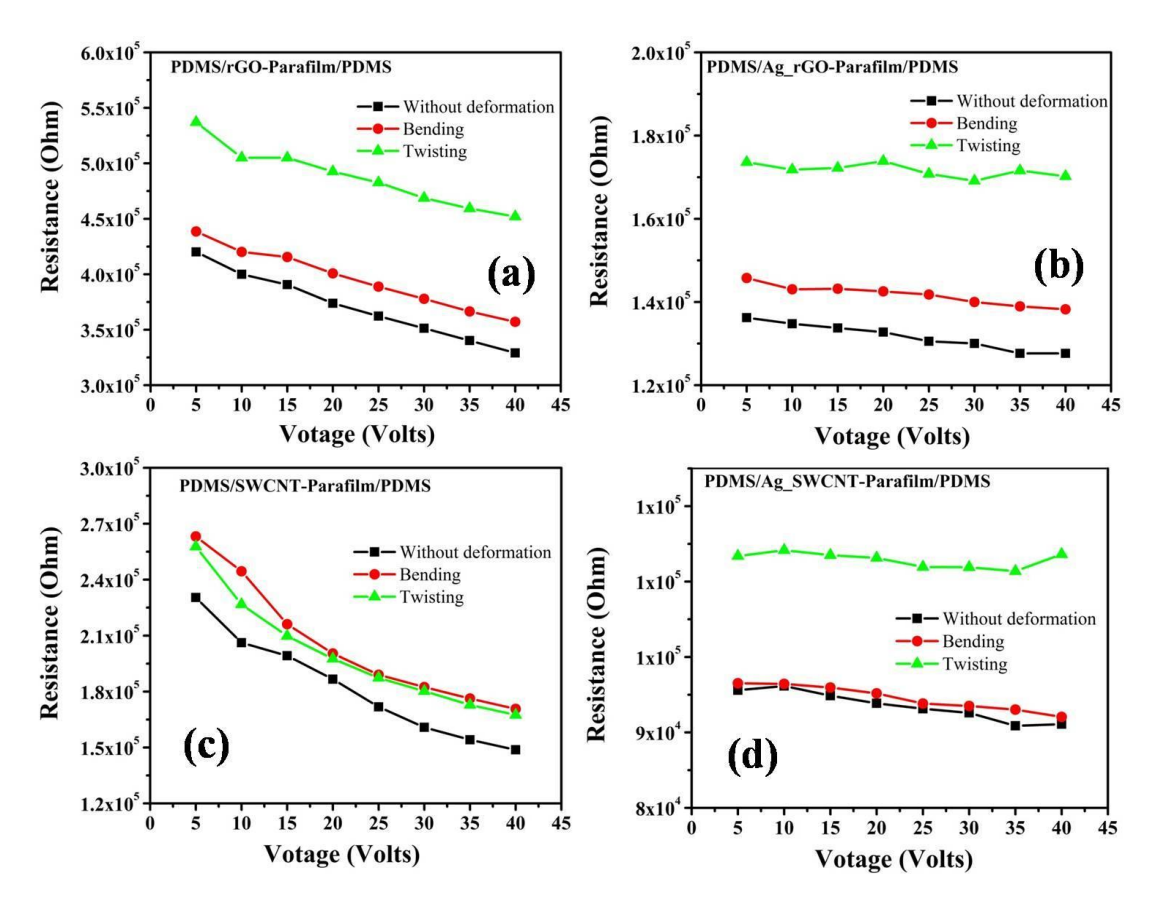


Fig. 5.7 Graphical representation of (a, b, c, and d) change in resistance with changing the voltage of the sandwich structured sample 1, 2, 3, and 4 for testing twisting and bending deformations respectively.

5.4 Strain sensing characteristics

The change in resistance of the sensors with the change in voltage was also investigated by applying deformation such as bending and twisting as shown in Fig. 5.7 (a-d). The experimental setup for measuring the change in resistance relative to the applied strain and deformations by bending and twisting of all the samples is shown in Fig 5.4. It is found that the resistance also changes nearly linearly with the applied voltage. Also, the resistance of the sensors increases due to the bending and twisting deformation. It is observed from Fig. 5.7 (a-d).

d) that PDMS/Ag_SWCNT-Parafilm/PDMS sample shows very little change in resistance by bending mode whereas it jumps to higher resistance in the twisting mode of deformation. Also, resistance does not change much with varying the voltage. Similarly, change in resistance with the applied voltage is not much for a PDMS/Ag_rGO-Parafilm/PDMS sample. It is also observed from the experimental results that the resistance of all the samples increases more under the twisting mode of deformation than the bending mode of deformation. The obtained results indicate that the fabricated samples are effective for sensing bending and twisting mode of deformations and further testing was carried out by applying longitudinal strain to all the samples that are shown in Fig. 5.8.

The resistance change was measured by the 4-Wire Ohms configuration by applying a fixed voltage (5V) and longitudinal strain (stretching) to the sensors as shown in Fig. 5.6. In the 4-Wire Ohms configuration, one channel acts as the source, and the other channel acts as the sensor which measures the change in resistance. The longitudinal strain was applied to the samples by pulling both ends of the samples equally as shown in Fig. 5.8 (b) in the range from 5%-35%. The sensors started to break down from the applied strain of 40%. Thus, the maximum 35% strain was applied to all the samples under testing.

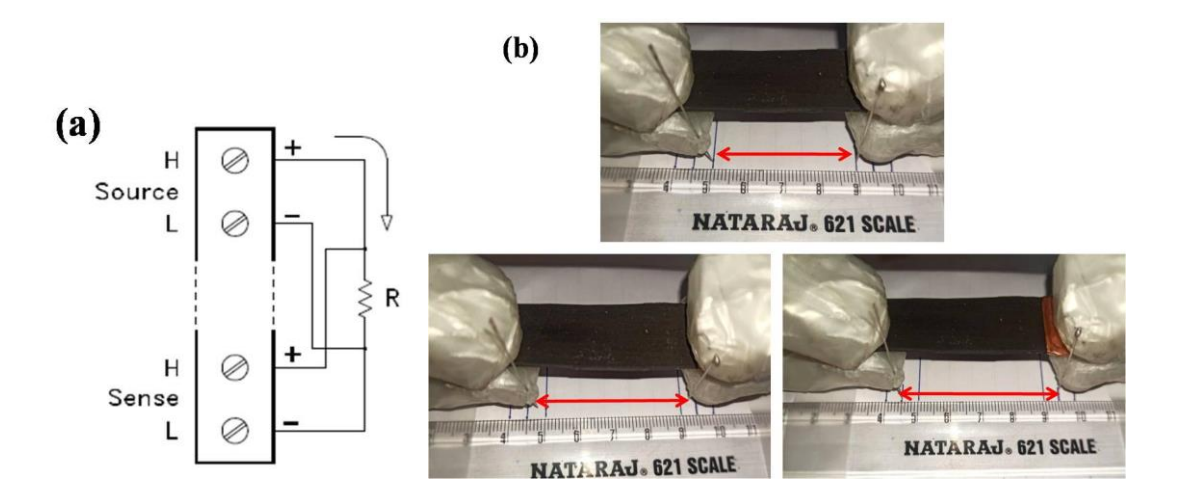


Fig. 5.8 (a) The 4-Wire Ohms configuration used for the measurement of change in resistance by applying a longitudinal strain and (b) strain measurement by equally pulling both the end of the samples.

The relative resistance changes are measured by the following formula

$$\frac{\Delta R}{R_0} = \frac{R - R_0}{R_0}$$

Where " R_{θ} " is the initial resistance and "R" is the resistance after the application of a particular strain to the fabricated samples.

The strain is calculated from the following formula

$$\varepsilon = \frac{l - l_0}{l_0}$$

Where " l_0 " is the initial length and "l" is the length after the application of a particular strain to the samples which is illustrated in Fig. 5.8 (b).

Finally, the Gauge factor (GF) is evaluated by using the following equation and shown in Fig. 5.9 (b).

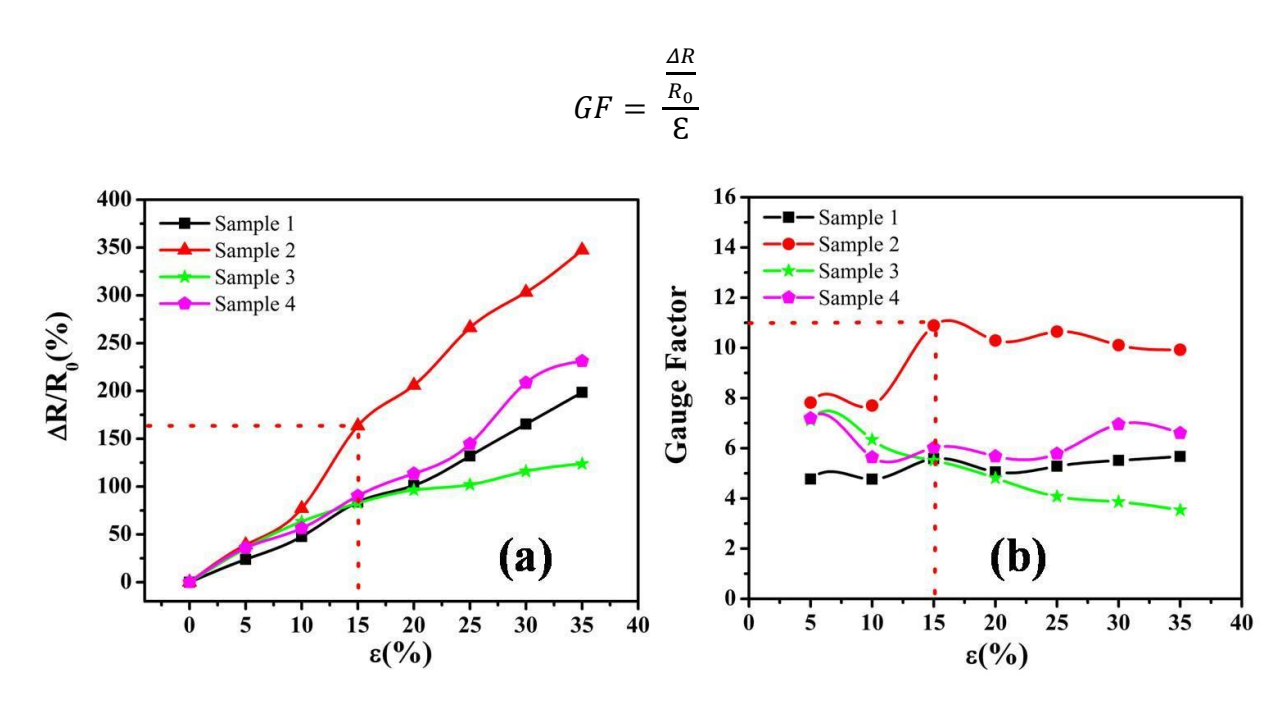


Fig. 5.9 Graphical presentation of (a) $\Delta R/R_0$ and (b) GF of all the fabricated samples with applied strain.

The $\Delta R/R_0$, that is presented in Fig. 5.9 (a), shows that the Ag_rGO based sandwich structure sample has a higher relative change in resistance and GF at 35% applied strain ($\Delta R/R_0 = 347$ % and GF = 10) than the rGO based sample ($\Delta R/R_0 = 198$ % and GF = 5.7). However, the linearity of the PDMS/rGO-Parafilm/PDMS sample is slightly higher ($R^2 = 0.994$) than the PDMS/Ag_rGO-Parafilm/PDMS sample ($R^2 = 0.989$). Similarly, the PDMS/Ag_SWCNT-Parafilm/PDMS sample has shown the higher value of $\Delta R/R_0$, GF and, linearity ($\Delta R/R_0 = 231$ %, GF = 6.6 and $R^2 = 0.979$) than the PDMS/SWCNT-Parafilm/PDMS sample ($\Delta R/R_0 = 124$ %, GF = 3.5 and $R^2 = 0.913$). It is also seen that the relative resistance drastically

increases for the PDMS/Ag_rGO-Parafilm/PDMS sample after 10% applied strain as compared to the other fabricated samples as shown in Fig. 5.9 (a). The same trend can be seen in the gauge factor of the PDMS/Ag_rGO-Parafilm/PDMS sample (Fig. 5.9 (b)). These experimental results indicated that the PDMS/Ag_rGO-Parafilm/PDMS sample shows the highest sensitivity and can be effectively used for strain sensors. From the experimental results, it is observed that the addition of Ag NPs to the rGO and SWCNTs contributes to the dense interconnection between them and hence improves the conductivity in the samples with $\Delta R/R_0$, GF, and linearity.

Table 5.2 Performance of the sandwich structured strain sensors by applying 35% strain.

<mark>Sensor</mark>	Conductivity	Relative	Gauge	Gauge	Linearity
	(S/m)	change in	Factor	Factor	R ²
		resistance	GF @ 15%	GF @ 35%	
		$\Delta R/R_0$	strain	strain	
		@35%			
		strain			
PDMS/rGO-	5.7×10 ⁻³	198	5.58	5.7	0.994
Parafilm/PDMS					
PDMS/Ag_rGO-	1.5×10 ⁻²	347	10.89	10	0.989
Parafilm/PDMS					
PDMS/SWCNT-	1.4×10 ⁻²	124	5.5	3.5	0.913
Parafilm/PDMS					
PDMS/Ag_SWCNT-	2.1×10 ⁻²	231	6	6.6	0.979
Parafilm /PDMS					

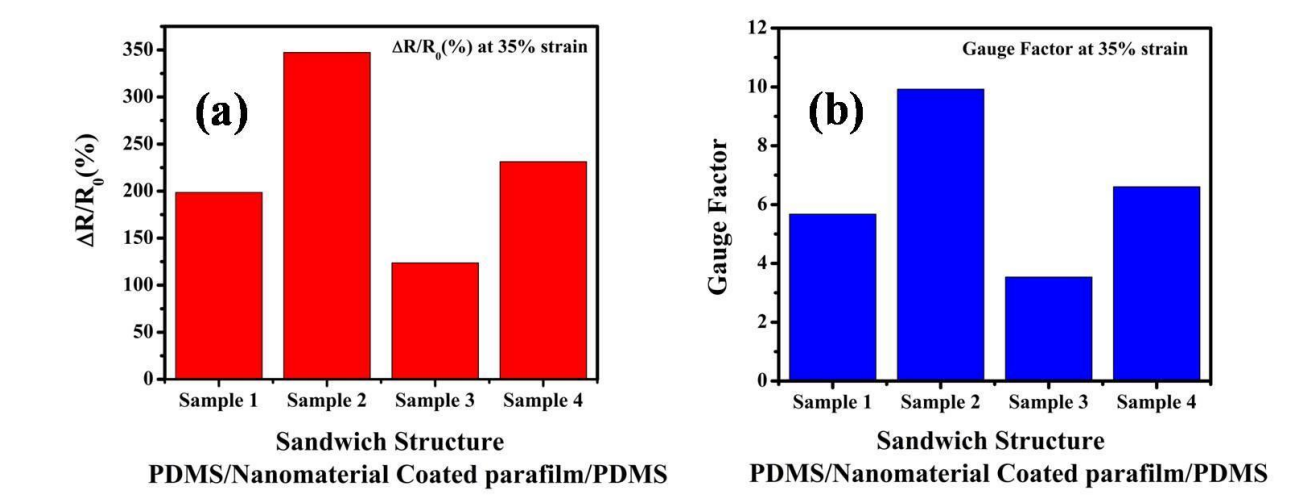


Fig. 5.10 Graphical representation of (a) $\Delta R/R_0$ and (b) GF of the fabricated sandwich structure samples.

The rGO-based sample has shown better improvement in $\Delta R/R_0$, GF, and linearity than the SWCNT-based sample. The contact resistance in the electrical network of the parafilm coated with rGO flakes and CNTs arises from the contact between the neighboring rGO flakes and between the tangled CNTs which results in low conductivity and a high value of initial resistance of the samples (R_o) [27]. The AgNPs in the rGO flakes and between the dense networks of CNTs significantly lowers the contact resistance in the Ag_rGO and Ag_SWCNT-based samples and hence the initial resistance of the samples (R_o) decreases. The possible mechanism of variations in relative resistance under the applied strain is illustrated in Fig. 5.11.

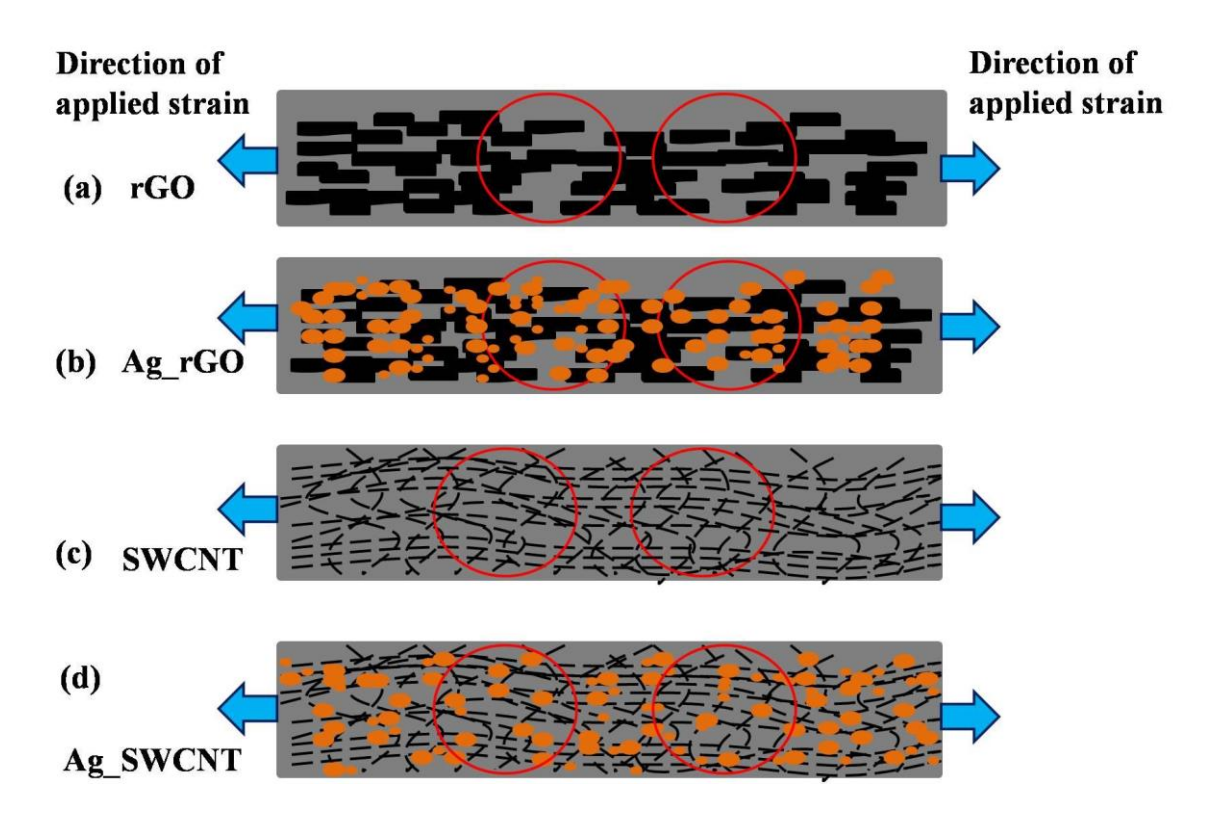


Fig. 5.11 Schematic representation of variation in the conductive network of the (a) rGO, (b) Ag_rGO , (c) SWCNTs, and (d) Ag_SWCNT -based samples under applied strain.

In the absence of strain, the sensitive materials are closely distributed. Due to the planar structure of rGO, the overlapping areas or the connecting network decreases during the stretching and hence decreases the conductivity and increases the relative resistance in the samples. The structure of the rGO is a planner or like sheets that are susceptible to crack more than the SWCNTs [27]. When the longitudinal strain is applied to the rGO-based sample (Fig. 5.11 (a)), the cross-link between the rGO is partially lost causing a decrease in electrical conductivity, and hence resistance increases. The SWCNTs are densely packed networks inside the samples. Although the cross-link between the SWCNTs is also partially

lost by applying strain, still the overall connectivity is maintained due to the 1-D morphology of SWCNTs as shown in Fig. 5.11 (c). Hence, the SWCNT-Based sample shows a lesser change in relative resistance under the applied strain than the rGO-based sample. However, in the case of Ag_rGO and Ag_SWCNT-based samples, the AgNPs enhance the conductivity by providing a dense conductive network even when strain is applied as illustrated in Fig. 5.11 (b and d). When the conductivity of the Ag_rGO and Ag_SWCNT-based samples are more and contact resistance is lesser than the rGO and SWCNT-based samples, the relative resistance changes drastically when the dense connective network of Ag_rGO-based and Ag_SWCNT-based samples is disrupted by the applied strain. Therefore, Ag_rGO-based and Ag_SWCNT-based samples show higher relative resistance and GF than the rGO-based and SWCNT-based samples. The $\Delta R/R_0$ and GF of the Ag-rGO-based sample are much higher than the Ag-SWCNT-based sample under the applied strain. The AgNPs enhance the conductivity and lowers the contact resistance in the Ag-rGO-based and Ag-SWCNT-based samples and maintain a connective network up to some extent even during the application of strain which is shown in Fig. 5.11 (b,d) [111]. However, the contact resistance in the Ag_SWCNT-based sample is expected to be higher than the Ag-rGO-based sample due to the higher conductivity of the SWCNTs than the rGO. Moreover, the distribution of the AgNPs in between the rGO sheets is more uniform than the distribution in between the tangled CNTs. Hence, the relative resistance changes drastically for the Ag_rGO-based sandwich structure during stretching which was more susceptible for crack propagation than the Ag_SWCNT-based sample. The obtained results explain that the AgNPs added to the rGO and SWCNTs improve the sensing characteristics of the fabricated sandwich structured samples. The Ag-rGO-based sandwich structure has shown higher sensing characteristics than the other samples and can be used as a strain sensor.

The repeatability of the fabricated samples was studied by stretching and relaxing and the hysteresis loops that are shown in Fig. 5.12 (a-d). In Fig. 5.12 (a-c), non-hysteresis behavior is observed for the sensing materials based on rGO and SWCNTs. However, hysteresis behavior is observed for the sensing materials based on Ag_rGO and Ag_SWCNT as shown in Fig. 5.12 (b) and (d). The hysteresis loop suggests that during relaxation of strain, AgNPs incorporated into the rGO and SWCNTs increase the contact between them, and hence the resistance drops more rapidly and the relative change in resistance decreases in the unloading cycle. The results suggest that the fabricated samples are showing good sensitivity and repeatability. Therefore, the fabricated samples are used for detecting various human body

movements by measuring the relative change in resistance with the movements of body parts such as the movement of the finger, wrist, and elbow, etc.

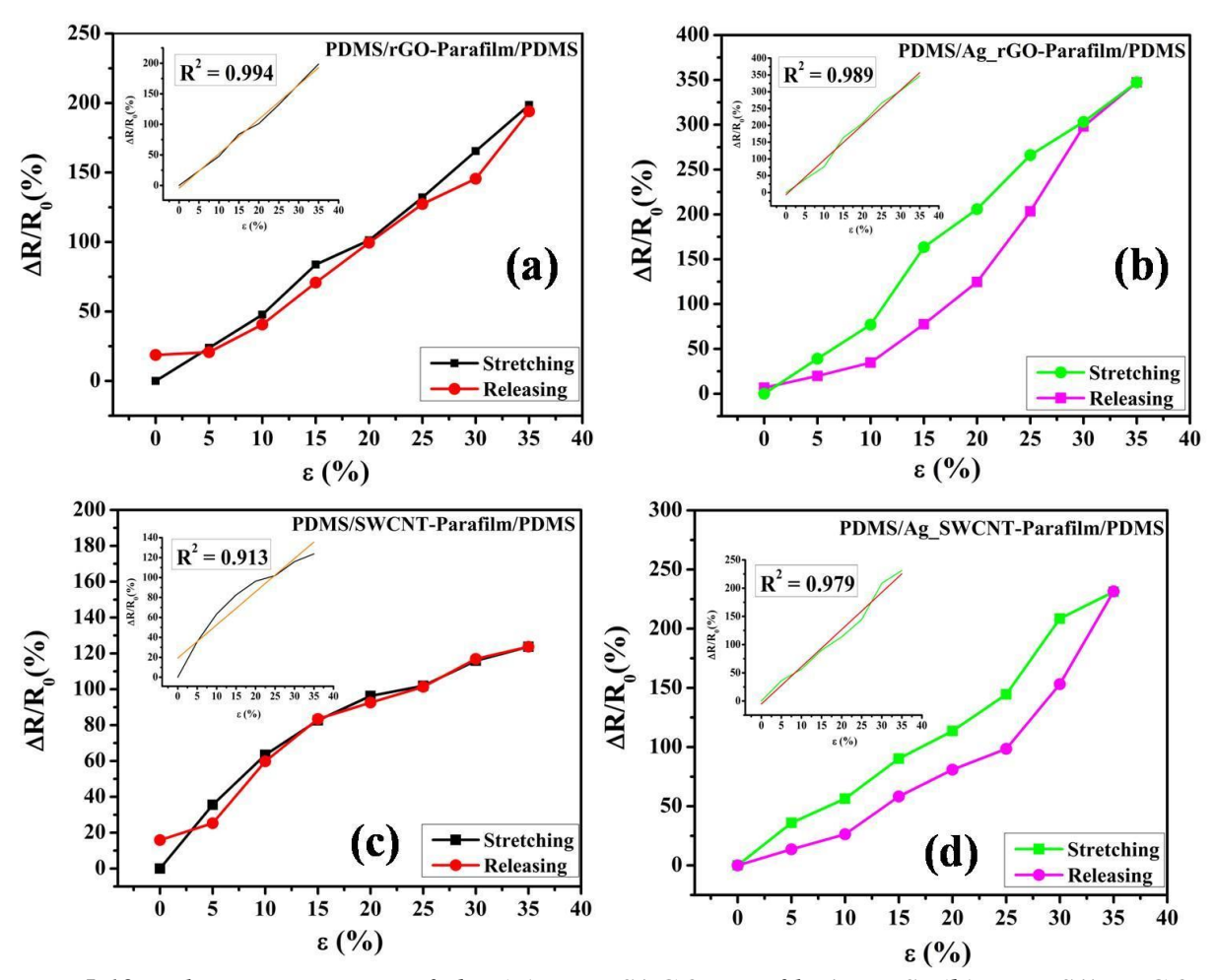


Fig. 5.12 Relative resistance of the (a) PDMS/rGO-Parafilm/PDMS, (b) PDMS/Ag_rGO-Parafilm/PDMS, (c) PDMS/SWCNT-Parafilm/PDMS, and (d) PDMS/Ag_SWCNT-Parafilm/PDMS samples under applied strain and relaxation.

5.5 Demonstration of detection of various movements of the human body by using the fabricated strain sensor

Three different sets of tests were conducted to achieve favorable monitoring of different movements of the body parts in real-time which includes the movement of the finger, wrist joint, and elbow joint. Both the ends of the sensors were attached to the joints of the finger, elbow, and wrist in such a way that the joints remain just below the middle part of the samples. Then, the strain was applied to the samples by bending the joints of the finger, wrist, and elbow at an angle ($\theta \sim 90^{\circ}$) as shown in Fig 5.13. As shown in Fig. 5.13, the sensors can detect small movements which include bending of the hand finger and wrist where the $\Delta R/R_0$ is small because the motion exerts much lower strain in the sensitive material. Likewise, the

sensors can detect larger movements such as the moment of the elbow where the relative change in resistance is higher than the other two deformations because the hand muscles exert much larger strain in the sensitive material.

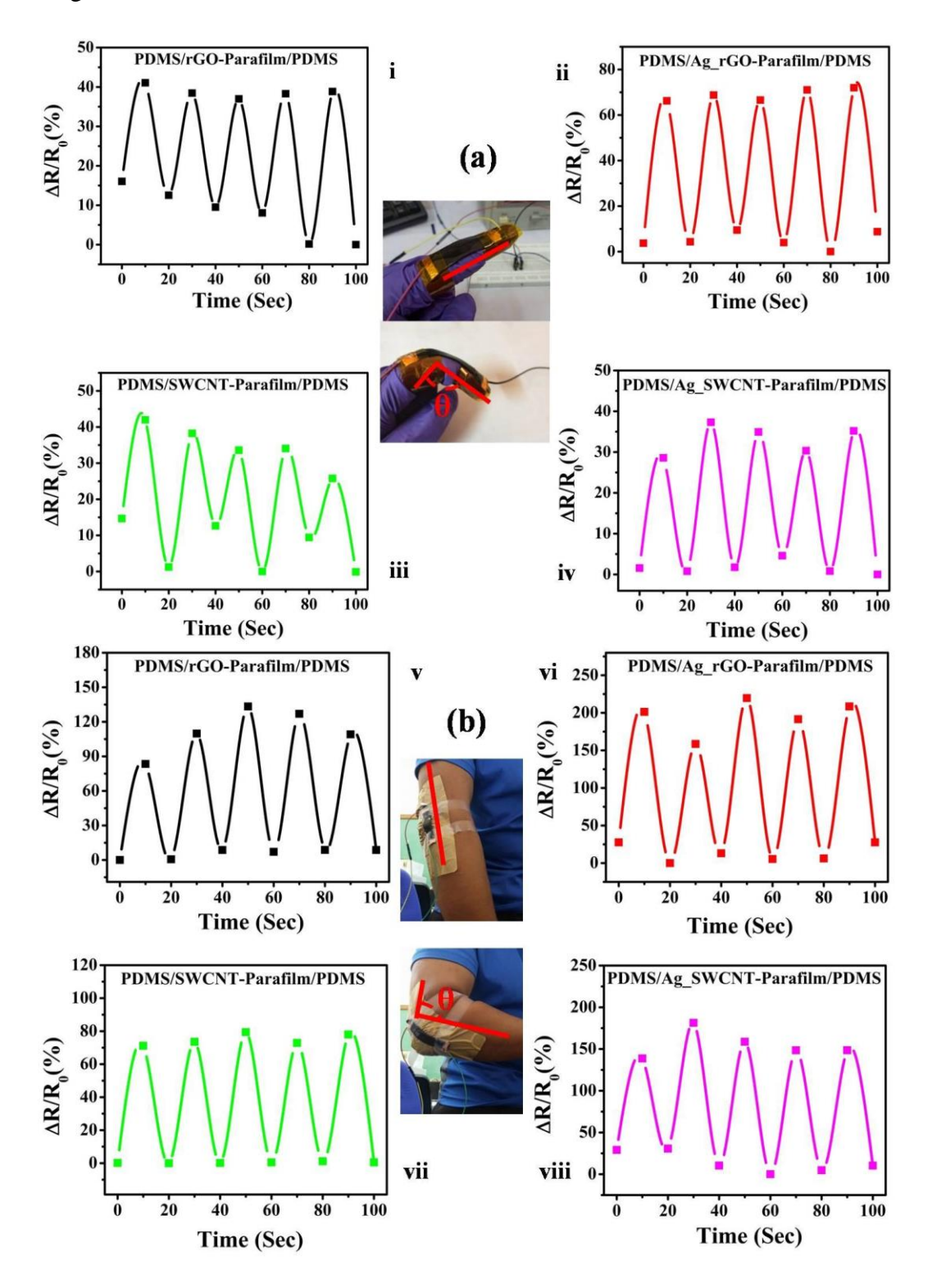


Fig. 5.13 Detection of various movements of the human body by the fabricated sensors: (a) Response of the sensors to the strain which was applied by the cycle motion of the index finger (i-iv) and (b) elbow (v-viii) respectively (continued next page).

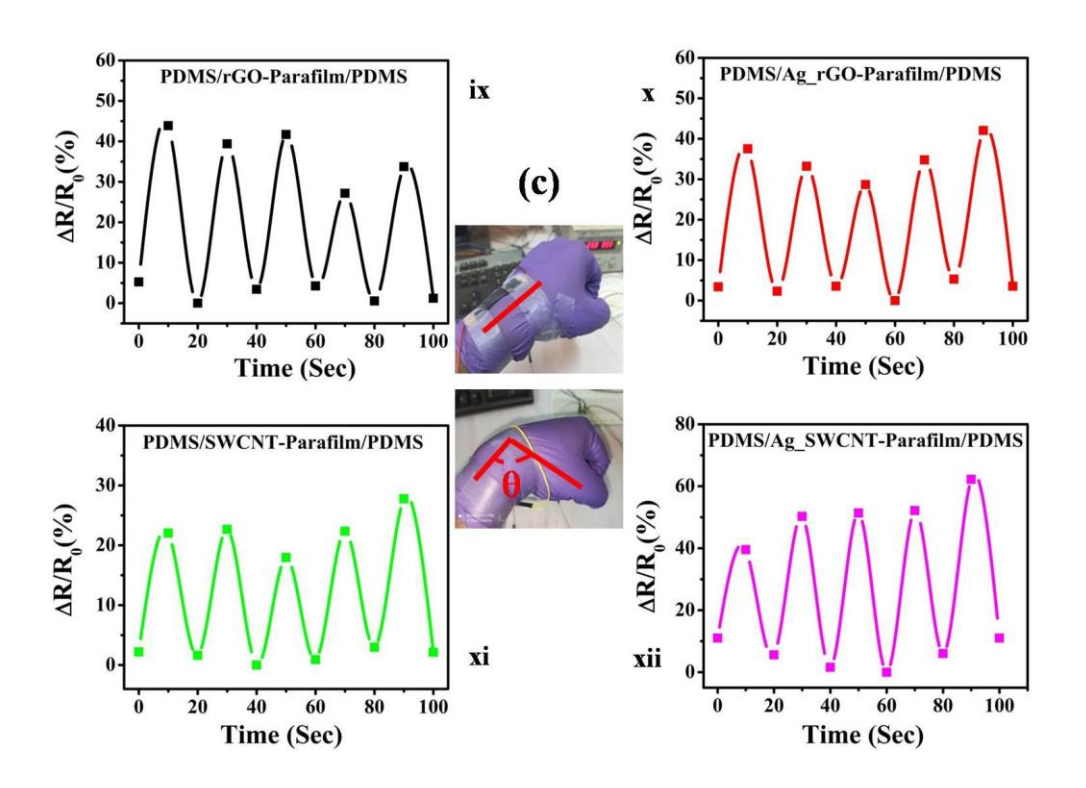


Fig. 5.13 Detection of various movements of the human body by the fabricated sensors: (c) Response of the sensors to the strain which was applied by the cycle motion of the wrist (ix-xii).

The relative change in resistance due to the slight deformation in the sensing material was measured concerning the bending of the joints. The measurement was carried out by keeping a 10-sec interval in the data acquisition system in between bending of the joints and relaxing to achieve optimum change in resistance. The data points were recorded as per the cycle of motion for bending of the joints and relaxing. The performance of the sensors to monitor the repeated motion of the index finger can be seen in Fig. 5.13 (a) and the range of $\Delta R/R_0$ is from ~30-70. The response of the sensors to the motion of the wrist is shown in Fig. 5.13 (c) and the relative resistance change is in the range from ~25-60. However, a higher strain is produced by the bending of the elbow than the former two movements due to the increased curvature and the $\Delta R/R_0$ is in the range of ~70-200 as shown in Fig. 5.13 (b). Therefore, the resistive-type sandwich structured strain sensors are capable to detect various motions of the human body parts ranging from small to large movements.

5.6 Demonstration of stability of the fabricated strain sensor in detecting movements of the human body for a longer duration

The stability of the strain sensors was also investigated by a long time cycle test where the strain was applied to the sensors through the motion of the index finger for 10 min duration

as shown in Fig. 5.14. The data was recorded by keeping a 3-sec interval per movement of bending and relaxing.

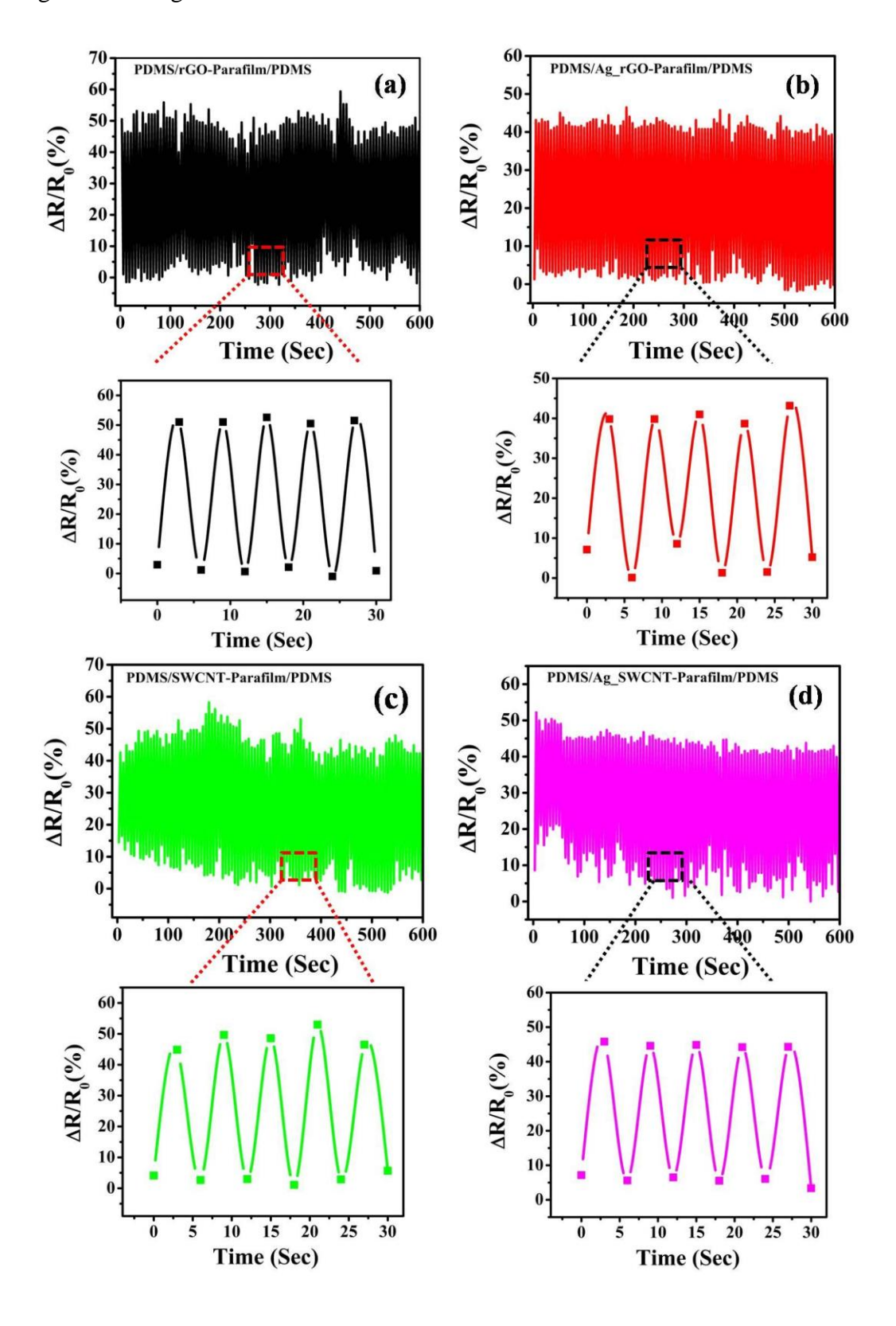


Fig. 5.14 Graphical representation that shows the stable detection of strain with time by the sensors at a faster rate (3 sec per movement). The tests were conducted with the cycle motion of the index finger for a longer duration (10 minutes).

For short-term monitoring of human motion, all the fabricated sensors have shown good response to detecting different human movements in real-time as shown in Fig. 5.13. However, the $\Delta R/R_0$ is more stable for Ag_rGO-based and Ag_SWCNT-based sensors than the rGO-based and SWCNT-based sensors. Therefore, the sensors fabricated by using Ag_rGO and Ag_SWCNT nanomaterials have shown better stability for monitoring human motion in a faster cycle for a longer duration. From the inset Fig. 5.14, it is found that the response time of all the sensors is less than 5 sec. Therefore, the fabricated strain sensors successfully demonstrated their ability to effectively monitor human motion in real-time at a faster rate and have shown potential for fabricating high-sensitive wearable sensors for human motion detection.

5.7 Conclusions

PDMS-based sandwich structured sensors were fabricated by coating nanomaterials such as rGO, Ag_rGO, SWCNT, and Ag_SWCNT to the parafilm films by a cost-effective method and without any material loss. The fabricated sensors have shown excellent response to the applied strain, good sensitivity, flexibility, and stretchability. The resistive-type strain sensors have shown excellent performance to detect different movements of various parts of the human body in real-time such as the cycle of motion of index finger, elbow, and wrist joints with better response time. The strain sensors fabricated from nanomaterials such as Ag_rGO and Ag_SWCNT have shown better performance to monitor human motion for the long term. Therefore, PDMS/Nanomaterials coated parafilm/PDMS-based sandwich structured flexible strain sensors have the potential to be utilized for applications such as wearable devices for the recognition of human motion.

CHAPTER 6 Conclusions

In the first part of this research work, different nanomaterials were successfully synthesized. GO was synthesized by the improved Hummers method and GO was chemically reduced by using hydrazine monohydrate. Similarly, Ag_rGO nanomaterial was also prepared by the chemical reduction method from GO and AgNPs. The Ag_SWCNT and Ag_MWCNT nanomaterials were synthesized by directly mixing the CNTs and AgNPs in an isopropanol solution. The TEM images of GO and rGO showed that both GO and rGO exhibited flakelike morphology and a few-layer morphology of rGO was observed. From the XRD analysis, it was found that GO was reduced which was confirmed from the XRD peak corresponding to (002) crystallographic plane of rGO. From the FTIR analysis, it was observed that due to the chemical reduction most of the oxygenated groups of GO were eliminated as they were absent in the FTIR spectra of rGO. The I_D/I_G ratios of rGO and Ag-rGO were higher than the I_D/I_G ratio of GO. From the morphological study of Ag_rGO nanomaterials, it was observed that AgNPs were sitting in between rGO flakes forming and the presence of AgNPs in the Ag_rGO composite was also confirmed from the XRD analysis. The TEM images of CNTs revealed that the MWCNTs have some amounts of amorphous phase present in them. The AgNPs were distributed between the tangled CNTs in the Ag_SWCNT and Ag_MWCNT nanomaterials. From the XRD, FTIR, and Raman analysis of Ag_SWCNT and Ag_MWCNT, it was found that the AgNPs were present with CNTs.

In the second part, flexible PDMS-based polymer composites were fabricated by incorporating different nanofillers such as GO, AgNPs, rGO, Ag_rGO, Ag_SWCNTs, and Ag_MWCNT. The SEM images of PDMS composites revealed that the nanofillers were distributed in the PDMS composite samples but they were agglomerated. The change in intensity of the XRD, FTIR, and Raman peaks of PDMS composites confirmed that the H-bonding that formed between the functional groups of the nanomaterials and PDMS polymer matrix was present. The dielectric spectroscopy was performed for the investigation of the dielectric constant, dielectric loss, and AC conductivity of the PDMS-based polymer composites. From the obtained results of dielectric properties, it is seen that the dielectric constant and dielectric loss increases with the increase of wt% of the nano-fillers in the low-frequency region. Also, the dielectric properties depend upon types of nanomaterials. Better dielectric properties were obtained for the PDMS composites fabricated by incorporating the Ag_rGO and Ag_SWCNT nanomaterials. These two samples showed higher dielectric permittivity than the other PDMS composites and the dielectric loss factor was comparatively low (less than 1). The possible mechanism for the improvement in dielectric permittivity was

discussed which is related to the distribution of AgNPs in the rGO layers and in between the tangled CNT. The AgNPs prevent the rGO from piling up and the electron transfer from the AgNPs to the rGO and the CNTs improved the dielectric properties in 1 Hz frequency. However, in 1 kHz frequency, the dielectric constant of Ag_rGO/PDMS composites decreases due to charge migration. The Ag_SWCNT/PDMS composites exhibited better properties in 1 kHz frequency than the Ag rGO/PDMS composites. The optimized value of dielectric properties is found for PDMS composites fabricated by incorporating 1 wt% Ag rGO ($\mathcal{E}' = 108$, Tan $\delta = 0.95$) and Ag SWCNT ($\mathcal{E}' = 85$, Tan $\delta = 0.15$) nanofillers. From the DC measurements, AC conductivity, and specific resistance results, it was found that the resistances of the PDMS nanocomposites were very high. The specific resistances of Ag_rGO/PDMS and Ag_SWCNT/PDMS composites at 1 kHz frequency were ~5.24×10⁹ Ω cm and 1.87×10^8 Ω cm respectively. The dielectric properties of the PDMS-based composites can be improved by increasing the wt% of the nanofillers. It is also possible to improve the distribution of AgNPs in between the rGO layers by adding more amount of well-dispersed AgNPs during chemical reduction of GO to synthesize Ag_rGO nanomaterials which may improve the electrical and dielectric properties of Ag rGO/PDMS composites. However, the process requires a large number of nanomaterials, and the flexibility of the PDMS composites will be compromised with a higher wt% of nanofillers. Besides, further study and methods need to be investigated to control the agglomeration of the nanomaterials in the polymer matrix which may improve the dielectric properties. Although the PDMSbased composites are not electrically conductive, the present work gives an idea about the fabrication of PDMS-based composites by a cost-effective method and tuning the dielectric properties of the PDMS composites with low wt% of nanofiller material which can be useful for dielectric-based sensors, capacitors, and energy storage-based applications. The capacitance-based measurements of sensing properties of the materials were not performed due to the unavailability of instruments.

Finally, a novel approach was adopted to fabricate PDMS/nanomaterials coated Parafilm/PDMS-based flexible sandwich structure where different nanomaterials were coated to a laboratory parafilm. After coating the nanomaterials, the wax-like surface of the parafilm provided good adhesion, and the nanomaterials embedded into the film during the heating and cooling cycle forming an electrically conductive network. Therefore, the parafilm coated with nanomaterial acted as the sensing part and the PDMS substrates provided flexibility to the sandwich structure during the application of strain. Different conductive nanomaterials

such as rGO, Ag_rGO, SWCNT, and Ag_SWCNT were coated to the laboratory parafilm to form an electrically conductive network of nanomaterials.

Table 6.1: Comparison of sensing properties of PDMS/Nanomaterials-coated-Parafilm/PDMS-based flexible and wearable sensors with the recently published results.

Sensor System	Content of conductive material	Stretchability %	Sensitivity (GF)	Linearity	Application	References
GNPs/PDMS	0.35 mg/ml	50	1.55	NA	Detection various human motions	[98]
GNPs/PDMS	40 wt%	25	62.5	NA	Detection of motion of the index finger and wrist pulse	[99]
MWCNTs/PDMS	15 mg	40	7.22	NA	Movements of the human body including bending of the wrist, elbow, and knee	[107]
CB-MWCNT/PDMS	2 wt%	130	61.82	NA	Detection of human motion and physiological activities	[108]
CNTs/PDMS	8 wt%	40	1.21	0.992	Human motion detection	[109]
Ag NPs/PDMS	0.0185 M	70	25.7	0.982		[110]
Ag NPs/PDMS	150 wt%	50	939		Real time monitoring of human body dynamics	[112]
PDMS/rGO/PDMS	10 mg/ml	35	5.7	0.994	Detection of movements of the index finger, wrist, and elbow joints	This work
PDMS/Ag_rGO/PD MS	10 mg/ml	35	10	0.989	-do-	This work
PDMS/SWCNT/PD MS	10 mg/ml	35	3.5	0.913	-do-	This work
PDMS/Ag_SWCNT/ PDMS	10 mg/ml	35	6.6	0.979	-do-	This work

The fabricated PDMS/rGO-Parafilm/PDMS, PDMS/Ag_rGO-Parafilm/PDMS, PDMS/SWCNT-Parafilm/PDMS, and PDMS/Ag_SWCNT-Parafilm/PDMS flexible sandwich structures exhibited an excellent response to the applied strain up to 35% and good sensitivity (GF =10), linearity, and repeatability owing to their flexibility and electrical

conductivity which is given in table 6.1. The strain sensors fabricated from nanomaterials such as Ag_rGO and Ag_SWCNT have shown better electrical conductivity, relative resistance with applied strain, better sensitivity and performance than the other fabricated sensors. The strain sensors exhibited excellent ability to detect different movements of the human body such as the cycle of motion of index finger, elbow, and wrist joints. The novelty of this work is that we adopted a very simple and low-cost method to fabricate wearable strain sensors based on the sandwich structure of PDMS/Nanomaterials coated Parafilm/PDMS by using laboratory parafilm which has not been reported so far and we achieved a balanced performance between sensitivity and stretchability, and good strain response in comparison to the reported works. The performance of the sandwich structures can be improved in the future by adopting the following methods

- a. Coating the parafilm multiple time (10-15 times) with the nanomaterial which may increase the conductivity,
- b. By applying PDMS film coating during the heating of the parafilm to the adhesion of the layers.
- c. Optimizing the thickness of the PDMS layers.

Therefore, the PDMS and parafilm-based flexible strain sensors have the potential to be utilized for strain sensing applications for example wearable devices for the detection of human motion.

CHAPTER 7 References

- 1. J. Xie, Q. Chen, H. Shen, and G. Li. Review—Wearable Graphene Devices for Sensing. Journal of The Electrochemical Society, 2020, 167, 037541.
- A. D. Valentine, T. A. Busbee, J. W. Boley, J. R. Raney, A. Chortos, A. Kotikian, J. D. Berrigan, M. F. Durstock, J. A. Lewis. Hybrid 3D Printing of Soft Electronics. Advanced Materials, 2017, 29, 1703817.
- 3. J. S. Heo, M. F. Hossain, and I. Kim. Challenges in Design and Fabrication of Flexible/Stretchable Carbon- and Textile-Based Wearable Sensors for Health Monitoring: A Critical Review. Sensors, 2020, 20, 3927; doi:10.3390/s20143927.
- 4. H. Souri, H. Banerjee, A. Jusufi, N. Radacsi, A. A. Stokes, I. Park, M. Sitti, and M. Amjadi. Wearable and Stretchable Strain Sensors: Materials, Sensing Mechanisms, and Applications. Advanced Intelligent Systems, 2020, 2, 2000039.
- 5. Y. Cheng, R. Wang, J. Sun, L. Gao. A Stretchable and Highly Sensitive Graphene-Based Fiber for Sensing Tensile Strain, Bending, and Torsion. Advanced Materials, 2015, 27, 7365.
- 6. S. Ryu, P. Lee, J. B. Chou, R. Xu, R. Zhao, A. J. Hart, S. G. Kim. Extremely Elastic Wearable Carbon Nanotube Fiber Strain Sensor for Monitoring of Human Motion. ACS Nano, 2015, 9, 5929.
- 7. J. Di, S. Yao, Y. Ye, Z. Cui, J. Yu, T. K. Ghosh, Y. Zhu, Z. Gu. Stretch-Triggered Drug Delivery from Wearable Elastomer Films Containing Therapeutic Depots. ACS Nano, 2015, 9, 9407.
- 8. M. Amjadi, A. Pichitpajongkit, S. Lee, S. Ryu, I. Park. Highly stretchable and sensitive strain sensor based on silver nanowire-elastomer nanocomposite. ACS Nano, 2014, 8, 5154.
- 9. M. Amjadi, Y. J. Yoon, I. Park. Ultra-stretchable and skin-mountable strain sensors using carbon nanotubes-Ecoflex nanocomposites. Nanotechnology, 2015, 26, 375501.
- 10. D. Rus, M. T. Tolley. Design, fabrication, and control of soft robots. Nature, 2015, 521, 467.
- 11. C. Harito, D. V. Bavykin, B. Yuliarto, H. K. Dipojonob, and Frank C. Walsh. Polymer nanocomposites having a high filler content: synthesis, structures, properties, and applications. Nanoscale, 2019, 11, 4653–4682.
- 12. S. Zhao, J. Li, D. Cao, G. Zhang, J. Li, K. Li, Y. Yang, W. Wang, Y. Jin, R. Sun, and C. P. Wong. Recent Advancements in Flexible and Stretchable Electrodes for Electromechanical Sensors: Strategies, Materials, and Features. ACS Applied Materials Interfaces, 2017, 9, 12147–12164.
- 13. M. Amjadi, K. U. Kyung, I. Park, M. Sitti. Stretchable, Skin-Mountable, and Wearable Strain Sensors and Their Potential Applications: A Review. Advanced Functional Materials, 2016, 26, 1678.
- 14. N. Wen, L. Zhang, D. Jiang, Z. Wu, B. Li, C. Suna, and Z. Guo. Emerging flexible sensors based on nanomaterials: recent status and applications. Journal of Materials Chemistry A, 2020, 8, 25499–25527.
- 15. D. G. Papageorgiou, I. A. Kinloch, R. J. Young. Graphene/elastomer nanocomposites. Carbon 95, 2015, 460-484.
- 16. K. Sun, P. Xie, Z. Wang, T. Su, Q. Shao, J. E. Ryu, X. Zhang, J. Guo, A. Shankar, J. Li, R. Fan, D. Cao, Z. Guo. Flexible polydimethylsiloxane/multi-walled carbon

- nanotubes membranous metal composites with negative permittivity. Polymer 125, 2017, 50-57.
- 17. L. Z. Guan, L. Zhao, Y. J. Wan, and L. C. Tang. Three-dimensional graphene-based polymer nanocomposites: preparation, properties, and applications. Nanoscale, 2018, 10, 14788–14811.
- 18. L. Ji, P. Meduri, V. Agubra, X. Xiao, and M. Alcoutlabi. Graphene-Based Nanocomposites for Energy Storage. Advanced Energy Materials, 2016, 1502159.
- 19. M. Silva, N. M. Alves, M. C. Paiva. Graphene-polymer nanocomposites for biomedical applications. Polymer Advanced Technology, 2018, 29, 687–700.
- 20. S. Choi, S. I. Han, D. Kim, T. Hyeon, and D. H. Kim. High-performance stretchable conductive nanocomposites: materials, processes, and device applications. Chem. Soc. Rev., 2019, 48, 1566.
- 21. S. Khan and L. Lorenzelli. Recent advances of conductive nanocomposites in printed and flexible electronics. Smart Material Structures, 2017, 26, 083001 (23pp).
- 22. M. Amjadi, M. Turan, C. P. Clementson, M. Sitti. Parallel Microcracks-based Ultrasensitive and Highly Stretchable Strain Sensors. ACS Applied Material Interfaces, 2016, 8, 5618.
- 23. J. Shi, X. Li, H. Cheng, Z. Liu, L. Zhao, T. Yang, Z. Dai, Z. Cheng, E. Shi, L. Yang, Z. Zhang, A. Cao, H. Zhu, and Y. Fang. Graphene Reinforced Carbon Nanotube Networks for Wearable Strain Sensors. Advanced Functional Materials, 2016, 26, 2078–2084.
- 24. G. S. Jeong, D. Baek, H. C. Jung, J. H. Song, J. H. Moon, S. W. Hong, I. Y. Kim, and S. Lee. Solderable and electroplatable flexible electronic circuit on a porous stretchable elastomer. Nature Communication, 2012, 3, 977.
- 25. G. Shi, Z. Zhao, J.-H. Pai, I. Lee, L. Zhang, C. Stevenson, K. Ishara. R. Zhang, H. Zhu, J. Ma. Highly Sensitive, Wearable, Durable Strain Sensors and Stretchable Conductors Using Graphene/Silicon Rubber Composites. Advanced Functional Materials, 2016, 26, 7614.
- 26. Z. F. Liu, S. Fang, F. A. Moura, J. N. Ding, N. Jiang, J. Di, M. Zhang, X. Lepro, D. S. Galvao, C. S. Haines, N. Y. Yuan, S. G. Yin, D. W. Lee, R. Wang, H. Y. Wang, W. Lv, C. Dong, R. C. Zhang, M. J. Chen, Q. Yin, Y. T. Chong, R. Zhang, X. Wang, M. D. Lima, R. Ovalle-Robles, D. Qian, H. Lu, and R. H. Baughman. STRETCHY ELECTRONICS. Hierarchically buckled sheath-core fibers for superelastic electronics, sensors, and muscles. Science, 2015, 349, 400–404.
- 27. S. Pan, Z. Pei, Z. Jin, J. Song, W. Zhang, Q. Zhang, and S. Sang. A highly stretchable strain sensor based on CNT/graphene/fullerene-SEBS. RSC Advances, 2020, 10, 11225–11232.
- 28. Y. G. Seol, Q. T. Tran, O. Yoon, I. Sohn, and N. Lee. Nanocomposites of reduced graphene oxide nanosheets and conducting polymer for stretchable transparent conducting electrodes. Journal of Material Chemistry, 2012, 22, 23759–23766.
- 29. X. Shi, S. Liu, Y. Sun, J. Liang, and Y. Chen. Lowering Internal Friction of 0D–1D–2D Ternary Nanocomposite-Based Strain Sensor by Fullerene to Boost the Sensing Performance. Advanced Functional Materials, 2018, 28, 1800850.

- 30. F. Han, J. Li, S. Zhao, Y. Zhang, W. Huang, G. Zhang, R. Sun, and C.-P. Wong. A crack-based nickel@graphene-wrapped polyurethane sponge ternary hybrid obtained by electrodeposition for highly sensitive wearable strain sensors. Journal of Material Chemistry. C, 2017, 5, 10167.
- 31. Y. Wang, J. Hao, Z. Huang, G. Zheng, K. Dai, C. Liu, C. Shen. A Highly Sensitive and Stretchable Yarn Strain Sensor for Human Motion Tracking Utilizing a Wrinkle-Assisted Crack Structure. Carbon. N. Y. 2018, 126, 360.
- 32. H. Liu, Y. Li, K. Dai, G. Zheng, C. Liu, C. Shen, X. Yan, J. Guo, and Z. Guo. Electrically conductive thermoplastic elastomer nanocomposites at ultralow graphene loading levels for strain sensor applications. Journal of Material Chemistry C, 2016, 4, 157–166.
- 33. G. Cai, J. Wang, K. Qian, J. Chen, S. Li, and P. S. Lee. Extremely Stretchable Strain Sensors Based on Conductive Self-Healing Dynamic Cross-Links Hydrogels for Human-Motion Detection. Advanced Science, 2017, 4, 1600190.
- 34. L. Meihong, W. Pengbo, W. Jiangru, G. Min, W. Xiaoxuan, W. Yonggang, S. Rui, and Z. Liqun. Wearable, Healable, and Adhesive Epidermal Sensors Assembled from Mussel-Inspired Conductive Hybrid Hydrogel Framework. Advanced Functional Material, 2017, 27, 1703852.
- 35. E. S. Bhagavatheswaran, M. Parsekar, A. Das, H. H. Le, S. Wiessner, K. W. Stoeckelhuber, G. Schmaucks and G. Heinrich. Journal of Physical Chemistry C, 2015, 119, 21723–21731.
- 36. M. Hempel, D. Nezich, J. Kong, and M. Hofmann. A Novel Class of Strain Gauges Based on Layered Percolative Films of 2D Materials. Nano Letters, 2012, 12, 5714–5718.
- 37. S. Wang, X. Zhang, X. Wu and C. Lu. Tailoring percolating conductive networks of natural rubber composites for flexible strain sensors via a cellulose nanocrystal templated assembly. Soft Matter, 2016, 12, 845–852.
- 38. W. Zhang, B. Yin, J. Wang, A. Mohamed, and H. Jia. Ultrasensitive and wearable strain sensors based on natural rubber/graphene foam. Journal Alloys Compound, 2019, 785, 1001.
- 39. Z. Ji, X. Zhang, C. Yan, X. Jia, Y. Xia, X. Wang, and F. Zhou. 3D Printing of Photocuring Elastomers with Excellent Mechanical Strength and Resilience. Macromolecules: Rapid Communications, 2019, 40, 1800873.
- 40. D. Han, C. Farino, C. Yang, T. Scott, D. Browe, W. Choi, J. W. Freeman, and H. Lee. Soft Robotic Manipulation and Locomotion with a 3D Printed Electroactive Hydrogel. ACS Applied Material Interfaces, 2018, 10, 17512–17518.
- 41. Y. Zhang, K. H. Lee, D. H. Anjum, R. Sougrat, Q. Jiang, H. Kim, and H. N. Alshareef. MXenes stretch hydrogel sensor performance to new limits. Advanced Science, 2018, 4, eaat0098.
- 42. S. G. Rathod, R. F. Bhajantri, V. Ravindrachary, J. Naik, and D. J. M. Kumar. High mechanical and pressure-sensitive dielectric properties of graphene oxide doped PVA nanocomposites. RSC Advances, 2016, 6, 77977–77986.

- 43. X. Huang, B. Sun, Y. Zhu, S. Li, P. Jiang. High-k polymer nanocomposites with 1D filler for dielectric and energy storage applications. Progress in Materials Science, 2019, 100, 187–225.
- 44. D. Zhu, S. H. Wang, and X. Zhou. Recent progress in fabrication and application of polydimethylsiloxane sponges. Journal of Material Chemistry A, 2017, 5, 16467–16497.
- 45. L. W. Jang, J. Lee, M. E. Razu, E. C. Jensen, and J. Kim. Fabrication of PDMS Nanocomposite Materials and Nanostructures for Biomedical Nanosystems. IEEE Transaction on Nanobioscience, Vol. 14, No. 8, December 2015.
- 46. Y. R. Jeong, H. Park, S. W. Jin, S. Y. Hong, S. Lee, and J. S. Ha. Highly Stretchable and Sensitive Strain Sensors Using Fragmentized Graphene Foam. Advanced Functional Materials, 2015, 25, 4228–4236.
- 47. S. Chun, Y. Choi, and W. Park. All-graphene strain sensor on soft substrate. Carbon, 2017, 116, 753.
- 48. S. H. Bae, Y. Lee, B. K. Sharma, H. J. Lee, J. H. Kim, J. H. Ahna. Graphene-based transparent strain sensor. Carbon, 2013, 51, 236-242.
- 49. S. Wu, S. Peng, Z. J. Han, H. Zhu, C. H. Wang. Ultrasensitive and Stretchable Strain Sensors Based on Mazelike Vertical Graphene Network. ACS Applied Material Interfaces, 2018, 10, 36312.
- 50. T. Yamada, Y. Hayamizu, Y. Yamamoto, Y. Yomogida, A. Izadi-Najafabadi, D. N. Futaba and K. Hata, Nat. A stretchable carbon nanotube strain sensor for human-motion detection. Nanotechnology, 2011, 6, 296.
- 51. R. Rahimi, M. Ochoa, W. Yu, B. Ziaie. Highly stretchable and sensitive unidirectional strain sensor via laser carbonization. ACS Applied Material Interfaces 2015, 7, 4463–4470.
- 52. Y. Cai, J. Shen, Z. Dai, X. Zang, Q. Dong, G. Guan, L. J. Li, W. Huang, and X. Dong. Extraordinarily Stretchable All-Carbon Collaborative Nanoarchitectures for Epidermal Sensors. Advanced Materials, 2017, 29, 1606411.
- 53. H. Yan, Y. Chen, Y. Deng, L. Zhang, X. Hong, W. Lau, J. Mei, D. Hui, H. Yan, Y. Liu. Coaxial printing method for directly writing stretchable cable as a strain sensor. Applied Physical Letters, 2016, 109.
- 54. N. Lu, C. Lu, S. Yang, and J. Rogers. Highly Sensitive Skin-Mountable Strain Gauges Based Entirely on Elastomers. Advanced Functional Materials, 2012, 22, 4044–4050.
- 55. N. S. Jang, S. H. Kim, J. M. Kim. Simple and rapid micropatterning of conductive carbon composites and its application to elastic strain sensors. Carbon, 2014, 77, 199–207.
- 56. Z. Cao, R. Wang, T. He, F. Xu, J. Sun. Interface-Controlled Conductive Fibers for Wearable Strain Sensors and Stretchable Conducting Wires. ACS Applied Material Interfaces, 2018, 10, 14087.
- 57. K. K. Kim, S. Hong, H. M. Cho, J. Lee, Y. D. Suh, J. Ham, and S. H. Ko. Highly Sensitive and Stretchable Multidimensional Strain Sensor with Prestrained Anisotropic Metal Nanowire Percolation Networks. Nano Letters, 2015, 15, 5240–5247.

- 58. S. Yao and Y. Zhu. Wearable multifunctional sensors using printed stretchable conductors made of silver nanowires. Nanoscale, 2014, 6, 2345–2352.
- 59. Y. Yang, L. Shi, Z. Cao, R. Wang, J. Sun. Strain Sensors with a High Sensitivity and a Wide Sensing Range Based on a Ti3C2Tx (MXene) Nanoparticle—Nanosheet Hybrid Network. Advanced Functional Materials, 2019, 29, 1807882.
- 60. K. Tybrandt, D. Khodagholy, B. Dielacher, F. Stauffer, A. F. Renz, G. Buzsaki, and J. Voros. High-Density Stretchable Electrode Grids for Chronic Neural Recording Advanced Materials, 2018, 30, 1706520.
- 61. G. S. Jeong, D. Baek, H. C. Jung, J. H. Song, J. H. Moon, S. W. Hong, I. Y. Kim, and S. Lee. Solderable and electroplatable flexible electronic circuit on a porous stretchable elastomer. Nature Communications, 2012, 3, 977.
- 62. C. Luo, J. Jia, Y. Gong, Z. Wang, Q. Fu, C. Pan. Highly Sensitive, Durable, and Multifunctional Sensor Inspired by a Spider. ACS Applied Material Interfaces, 2017, 9, 19955.
- 63. M. E. Rhazi, S. Majid, M. Elbasri, F. E. Salih, L. Oularbi, and Khalid Lafdi. Recent progress in nanocomposites based on conducting polymer: application as electrochemical sensors. International Nano Letters, 2018, 8, 79–99.
- 64. Z. M. Dang, M. S. Zheng, and J. W. Zha. 1D/2D Carbon Nanomaterial-Polymer Dielectric Composites with High Permittivity for Power Energy Storage Applications. Small, 2016, 12, No. 13, 1688–1701.
- 65. Prateek, V. K. Thakur, and R. K. Gupta. Recent Progress on Ferroelectric Polymer-Based Nanocomposites for High Energy Density Capacitors: Synthesis, Dielectric Properties, and Future Aspects. Chemical Review, 2016, 116, 4260–4317.
- 66. Z. Spitalskya, D. Tasis, K. Papagelis, and C. Galiotis. Carbon nanotube-polymer composites: Chemistry, processing, mechanical and electrical properties. Progress in Polymer Science, 2010, 35, 357–401.
- 67. M. Bhattacharya. Polymer Nanocomposites—A Comparison between Carbon Nanotubes, Graphene, and Clay as Nanofillers. Materials, 2016, 9, 262.
- 68. B. F. Jogi, M. Sawant, M. Kulkarni, P. K. Brahmankar. Dispersion and Performance Properties of Carbon Nanotubes (CNTs) Based Polymer Composites: A Review. Journal of Encapsulation and Adsorption Sciences, 2012, 2, 69-78.
- 69. J. Chen, B. Liu, X. Gao, and D. Xu. A review of the interfacial characteristics of polymer nanocomposites containing carbon nanotubes. RSC Advances, 2018, 8, 28048
- 70. Y. Liu and S. Kumar. Polymer/Carbon Nanotube Nano Composite Fibers—A Review. ACS Applied Material Interfaces, 2014, 6, 6069–6087.
- 71. E. Singh, M. Meyyappan, and H. Singh Nalwa. Flexible Graphene-Based Wearable Gas and Chemical Sensors. ACS Applied Material Interfaces, 2017, 9, 34544–34586.
- 72. A. Nag, A. Mitra, S. C. Mukhopadhyay. Graphene and its sensor-based applications: A review. Sensors and Actuators A, 2018, 270, 177–194.
- 73. Z. Wang, J. K. Nelson, H. Hillborg, S. Zhao, and L. S. Schadler. Graphene Oxide Filled Nanocomposite with Novel Electrical and Dielectric Properties. Advanced Materials, 2012, 24, 3134–3137.

- 74. K. Hu, D. D. Kulkarni, I. Choi, V. V. Tsukruk. Graphene-polymer nanocomposites for structural and functional applications. Progress in Polymer Science, 2014, 39, 1934–1972.
- 75. K. K. Sadasivuni, D. Ponnamma, B. Kumar, M. Strankowskie, R. Cardinaels, P. Moldenaers, S. Thomas, Y. Grohens. Dielectric properties of modified graphene oxide filled polyurethane nanocomposites and its correlation with rheology. Composite Science Technology, 2014, 104, 18-25.
- 76. X. F. Zhang, Z. G. Liu, W. Shen, and S. Gurunathan. Silver Nanoparticles: Synthesis, Characterization, Properties, Applications, and Therapeutic Approaches. International Journal of Molecular Science, 2016, 17, 1534.
- 77. K. Jyoti, M. Baunthiyal, A. Singh. Characterization of silver nanoparticles synthesized using Urtica dioica Linn. leaves and their synergistic effects with antibiotics. Journal of Radiation Research and Applied Sciences, 2016, 9, 217-227.
- 78. W. Zhang, E. Bi, M. Li, L. Gao. Synthesis of Ag/RGO composite as effective conductive ink filler for flexible inkjet printing electronics. Colloids and Surfaces A: Physicochem. Eng. Aspects, 2019, 490, 232–240.
- 79. J. Ren, C. Wang, X. Zhang, C. Tian, K. Chen, Y. Yin, F. Torrisi. Environmentally-friendly conductive cotton fabric as flexible strain sensor based on hot press reduced graphene oxide. Carbon, 2017, 111, 622–630.
- 80. Y. Ai, T. H. Hsu, D. C. Wu, L. Lee, J.-H. Chen, Y.-Z. Chen, S.-C. Wu, C. Wu, Z. M. Wang, and Y.-L. Chueh. An ultrasensitive flexible pressure sensor for multimodal wearable electronic skins based on large-scale polystyrene ball@reduced graphene-oxide core-shell nanoparticles. Journal of Material Chemistry C, 2018, 6, 5514.
- 81. H. P. Zhou, X. Ye, W. Huang, M. Q. Wu, L. N. Mao, B. Yu, S. Xu, I. Levchenko, and K. Bazooka. Wearable, Flexible, Disposable Plasma-Reduced Graphene Oxide Stress Sensors for Monitoring Activities in Austere Environments. ACS Applied Material Interfaces, 2019, 11, 15122.
- 82. J. Ma, P. Wang, H. Chen, S. Bao, W. Chen, H. Lu. Highly Sensitive and Large-Range Strain Sensor with a Self-Compensated Two-Order Structure for Human Motion Detection. ACS Applied Material Interfaces, 2019, 11, 8527.
- 83. R. Rahimi, M. Ochoa, W. Yu, B. Ziaie. Highly stretchable and sensitive unidirectional strain sensor via laser carbonization. ACS Applied Material Interfaces, 2015, 7, 4463–4470.
- 84. C. Lee, L. Jug, and E. Meng, E. Erratum: High strain biocompatible polydimethylsiloxane-based conductive graphene and multiwalled carbon nanotube nanocomposite strain sensors. Applied Physical Letters, 2013, 103 (18), 183511.
- 85. Chao-Xuan Liua, Jin-WooChoi. Analyzing resistance response of embedded PDMS and carbon nanotubes composite under tensile strain. Microelectronic Engineering. 2014, 117, Pages 1-7.
- 86. X. Guo, Y. Huang, Y. Zhao, L. Mao, L. Gao, W. Pan, Y. Zhang, P. Liu. Highly stretchable strain sensor based on SWCNTs/CB synergistic conductive network for wearable human-activity monitoring and recognition. Smart Material Structure, 2017, 26, 095017.

- 87. J. Sun, Y. Zhao, Z. Yang, J. Shen, E. Cabrera, M. J. Lertola, W. Yang, D. Zhang, A. Benatar, J. M. Castro, D. Wu, L. J. Lee. Nanotechnology. 2018, 29, 355304.
- 88. B. Nie, X. Li, J. Shao, X. Li, H. Tian, D. Wang, Q. Zhang, B. Lu. Flexible and Transparent Strain Sensors with Embedded Multiwalled Carbon Nanotubes Meshes ACS Applied Material Interfaces, 2017, 9, 40681.
- 89. J. H, Lee, D. Yang, S. Kim, I. Park. Stretchable strain sensor based on metal nanoparticle thin film for human motion detection & flexible pressure sensing devices. Nanoscale 2014, 6, 11932.
- 90. L. Liu, Q. Zhang, D. Zhao, A. Jian, J. Ji, Q. Duan, W. Zhang, and S. Sang. Preparation and Property Research of Strain Sensor Based on PDMS and Silver Nanomaterials. Journal of Sensors, 2017, 7843052, 8 pages.
- 91. K. Takei, Z. Yu, M. Zheng, H. Ota, T. Takahashi, and A. Javey. Highly sensitive electronic whiskers based on patterned carbon nanotube and silver nanoparticle composite films. Proceeding of National Academy of Science, U. S. A., 2014, 111, 1703.
- 92. Y. Tang, Z. Zhao, H. Hu, Y. Liu, X. Wang, S. Zhou, and J. Qiu. Highly Stretchable and Ultrasensitive Strain Sensor Based on Reduced Graphene Oxide Microtubes–Elastomer Composite. ACS Applied Material Interfaces, 2015, 7, 27432–27439.
- 93. S. Wu, R. B. Ladani, J. Zhang, K. Ghorbani, X. Zhang, A. P. Mouritz, A. J. Kinloch, and C. H. Wang. Strain Sensors with Adjustable Sensitivity by Tailoring the Microstructure of Graphene Aerogel/PDMS Nanocomposites. ACS Applied Material Interfaces, 2016, 8, 24853–24861.
- 94. X. Ye, Z. Yuan, H. Tai, W. Li, X. Du, and Y. Jiang. A wearable and highly sensitive strain sensor based on a polyethyleneimine–rGO layered nanocomposite thin film. Journal of Material Chemistry, C, 2017, 5, 7746—7752.
- 95. X. M. Zhang, X. L. Yang and K. Y. Wang. Conductive graphene/polydimethylsiloxane nanocomposites for flexible strain sensors. Journal of Materials Science: Materials in Electronics, 2019, 30, 19319–19324.
- 96. G. Li, K. Dai, M. Ren, Y. Wang, G. Zheng, C. Liu, and C. Shen. Aligned flexible conductive fibrous networks for highly sensitive, ultra stretchable, and wearable strain sensors. Journal of Material Chemistry, C, 2018, 6, 6575—6583.
- 97. Y. Jung, K. Jung, B. Park, J. Choi, D. Kim, J. Park, J. Ko and H. Cho. Wearable piezoresistive strain sensor based on graphene-coated three-dimensional microporous PDMS sponge. Micro and Nano System Letters, 2019, 7, 20.
- 98. H. Lee, M. J. Kim, J. H. Kim, J. Y. Lee, E. Ji, A. Capasso, H. J. Choi, W. Shim, and G. H. Lee. Highly flexible graphene nanoplatelet-polydimethylsiloxane strain sensors with proximity-sensing capability. Materials Research Express, 2020, 7, 045603.
- 99. S. Baloda, Z. A. Ansari, S. Singh, and N. Gupta. Development and Analysis of Graphene Nanoplatelets (GNPs)-Based Flexible Strain Sensor for Health Monitoring Applications. IEEE SENSORS JOURNAL, VOL. 20, NO. 22, NOVEMBER 15, 2020.

- 100. Z. Su, H. Chen, Y. Song, X. Cheng, X. Chen, H. Guo, L. Miao, and H. Zhang. Microsphere-Assisted Robust Epidermal Strain Gauge for Static and Dynamic Gesture Recognition. Small, 2017, 13, 1702108.
- 101. Y. Jung, K. K. Jung, D. H. Kim, D. H. Kwak, and J. S. Ko. Linearly Sensitive and Flexible Pressure Sensor Based on Porous Carbon Nanotube/Polydimethylsiloxane Composite Structure. Polymers 2020, 12, 1499; doi:10.3390/polym12071499.
- 102. Y. Gao, X. Fang, J. Tan, T. Lu, L. Pan, and F. Xuan. Highly sensitive strain sensors based on fragmentized carbon nanotube/polydimethylsiloxane composites. Nanotechnology, 2018, 29, 235501.
- 103. S. Wang, P. Xiao, Y. Liang, J. Zhang, Y. Huang, S. Wu, S. W. Kuo, and T. Chen. Network cracks-based wearable strain sensors for subtle and large strain detection of human motions. Journal of Material Chemistry, C, 2018, 6, 5140.
- 104. K. Park, P. Tran, N. Deaton, and J. P. Desai. Multi-walled Carbon Nanotube (MWCNT)/PDMS-based Flexible Sensor for Medical Applications. 2019 International Symposium on Medical Robotics (ISMR).
- 105. Q. Li, J. Li, D. Tran, C. Luo, Y. Gao, C. Yub, and F. Xuan. Engineering of carbon nanotube/polydimethylsiloxane nanocomposites with enhanced sensitivity for wearable motion sensors. Journal of Material Chemistry, C, 2017, 5, 11092.
- 106. J. H. Kim, J. Y. Hwang, H. R. Hwang, H. S. Kim, J. H. Lee, J. W. Seo, U. S. Shin & S. H. Lee. Simple and cost-effective method of highly conductive and elastic carbon nanotube/polydimethylsiloxane composite for wearable electronics. Scientific Reports, 2018, 8, 1375.
- 107. T. Li, J. Li, A. Zhong, F. Han, R. Sun, C. P. Wong, F. Niue, G. Zhang, Y. Jin. A flexible strain sensor based on CNTs/PDMS microspheres for human motion detection. Sensors and Actuators A, 2020, 306, 111959.
- 108. P. Zhang, Y. Chen, Y. Li, Y. Zhang, J. Zhang, and L. Huang. A Flexible Strain Sensor Based on the Porous Structure of a Carbon Black/Carbon Nanotube Conducting Network for Human Motion Detection. Sensors, 2020, 20, 1154; doi:10.3390/s20041154.
- 109. J. Du, L. Wang, Y. Shi, F. Zhang, S. Hu, P. Liu, A. Li, and J. Chen. Optimized CNT-PDMS Flexible Composite for Attachable Health-Care Device. Sensors, 2020, 20, 4523; doi:10.3390/s20164523.
- 110. H. M. Soe, A. A. Manaf, A. Matsuda, M. Jaafar. Development and fabrication of highly flexible, stretchable, and sensitive strain sensor for long durability based on silver nanoparticles—polydimethylsiloxane composite. Journal of Materials Science: Materials in Electronics, 2020, 31:11897–11910.
- 111. I. Kim, K. Woo, Z. Zhong, P. Ko, Y. Jang, M. Jung, J. Jo, S. Kwon, S. H. Lee, S. Lee, H. Youn, and J. Moon. A photonic sintering derived Ag flake/ nanoparticle-based highly sensitive stretchable strain sensor for human motion monitoring. Nanoscale, 2018, 10, 7890–7897.
- H. Li, J. Zhang, J. Chen, Z. Luo, J. Zhang, Y. Alhandarish, Q. Liu, W. Tang & L. Wang. A Supersensitive, Multidimensional Flexible Strain Gauge Sensor Based on Ag/PDMS for Human Activities Monitoring. Scientific Reports, 2020, 10, 4639.

- 113. X. Zhao, W. Xu, W. Yib, Y. Penga. A flexible and highly pressure-sensitive PDMS sponge based on silver nanoparticles decorated reduced graphene oxide composite. Sensors and Actuators A, 2019, 291, 23–31.
- 114. L. Zhang, H. Kou, Q. Tan, G. Liu, W. Zhang, and J. Xiong. High-performance strain sensor based on a 3D conductive structure for wearable electronics. Journal of Physics D: Appl. Phys. 2019, 52, 395401.
- 115. Z. Yuan, Z. Pei, M. Shahbaz, Q. Zhang, K. Zhuo, C. Zhao, W. Zhang, X. Ma, and S. Sang. Wrinkle Structured Network of Silver-Coated Carbon Nanotubes for Wearable Sensors. Nanoscale Research Letters, 2019, 14:356 https://doi.org/10.1186/s11671-019-3186-5.
- 116. Y. Yang, C. Luo, J. Jia, Y. Sun, Q. Fu, and C. Pan. A Wrinkled Ag/CNTs-PDMS Composite Film for a High-Performance Flexible Sensor and Its Applications in Human-Body Single Monitoring. Nanomaterials, 2019, 9, 850; doi:10.3390/nano9060850.
- 117. B. Liua, H.Tangc, Z. Luo, W. Zhang, Q. Tua, X. Jin.Wearable carbon nanotubes-based polymer electrodes for ambulatory electrocardiographic measurements. Sensors and Actuators A, 2017, 265, 79–85.
- 118. S. Nasiria, M. R. Khosravanic. Progress and challenges in fabrication of wearable sensors for health monitoring. Sensors and Actuators A, 2020, 312, 112105.
- 119. D. C. Marcano, D. V. Kosynkin, J.M. Berlin, A. Sinitskii, Z. Sun, A. Slesarev, L.B. Alemany, W. Lu, J.M. Tour, Improved synthesis of graphene oxide, ACS Nano 4 (8) (2010) 4806–4814.
- 120. L. Stobinski, B. Lesiaka, A. Malolepszy, M. Mazurkiewicz, B. Mierzwa, J. Zemek, P. Jiricek, I. Bieloshapk. Graphene oxide and reduced graphene oxide studied by the XRD, TEM, and electron spectroscopy methods. Journal of Electron Spectroscopy and Related Phenomena 195 (2014) 145–154.
- 121. J. Jayachandiran, J. Yesuraj, M. Arivanandhan, A. Raja, S. Austin Suthanthiraraj, R. Jayavel, and D. Nedumaran. Synthesis and Electrochemical Studies of rGO/ZnO Nanocomposite for Supercapacitor Application. Journal of Inorganic and Organometallic Polymers and Materials (2018) 28:2046–2055.
- 122. T. F. Emiru, D. W. Ayele. Controlled synthesis, characterization, and reduction of graphene oxide: A convenient method for large-scale production. Egyptian Journal of Basic and Applied Sciences 4 (2017) 74–79.
- 123. S. Park, J. An, J. R. Potts, A. Velamakanni, S. Murali, and R. S. Ruoff. Hydrazine-reduction of graphite- and graphene oxide. CARBON 49 (2011) 3019 3023.
- 124. M. A. M. Khan, S. Kumar, M. Ahamed, S. A. Alrokayan, and M. S. Al Salhi. Structural and thermal studies of silver nanoparticles and electrical transport study of their thin films. Nanoscale Research Letters, 6, (2011), 434.
- 125. K. Anandalakshmi, J. Venugobal and V. Ramasamy. Characterization of silver nanoparticles by green synthesis method using Pedalium murex leaf extract and their antibacterial activity. Applied Nanoscience 6, (2016), 399–408.

- 126. B. K. Mehta, M. Chhajlani, and B. D. Shrivastava. Green synthesis of silver nanoparticles and their characterization by XRD. IOP Conf. Series: Journal of Physics: Conf. Series 1823364 (526071879) 0012050.
- 127. M. S. P. Kyung, H. K. Young, and S. Lee. Fluorination of single-walled carbon nanotube: The effects of fluorine on structural and electrical properties. Journal of Industrial and Engineering Chemistry Volume 37, 25 May 2016, Pages 22-26
- 128. B. D. Ossonon and D. Belanger. Synthesis and characterization of sulfophenylfunctionalized reduced graphene oxide sheets. RSC Adv., 7, (2017), 27224.
- 129. F. T. Johra, W. G. Jung. Hydrothermally reduced graphene oxide as a supercapacitor. Applied Surface Science, 357, (2015), 1911–1914.
- 130. N. Hu, Z. Yang, Y. Wang, L. Zhang, Y. Wang, X. Huang, H. Wei, L. Wei, and Y. Zhang. Ultrafast and sensitive room temperature NH₃ gas sensors based on chemically reduced graphene oxide. Nanotechnology 25 (2014) 025502 (9pp).
- 131. L. Gharibshahi, E. Saion, E. Gharibshahi, A. H. Shaari, and K. A. Matori. Structural and Optical Properties of Ag Nanoparticles Synthesized by Thermal Treatment Method. Materials, 10, (2017), 402.
- 132. B. Wang, Y. Wua, X. Wang, Z. Chena, C. He. Copper phthalocyanine noncovalent functionalized single-walled carbon nanotube with enhanced NH3 sensing performance. Sensors and Actuators B 190 (2014) 157–164.
- 133. M. S. Tehrani, P. A. Azar, P. E. Namin, S. M. Dehaghi. Removal of Lead Ions from Wastewater Using Functionalized Multiwalled Carbon Nanotubes with Tris(2-Aminoethyl)Amine. Journal of Environmental Protection, 2013, 4, 529-536.
- 134. N. M. S Hidayah, W. W. Liu, C. W. Lai, N. Z. Noriman, C. S. Khe, U. Hashim and H. C. Lee. Comparison on Graphite, Graphene Oxide, and Reduced Graphene Oxide: Synthesis and Characterization. Conference Paper in AIP Conference Proceedings · October 2017, DOI: 10.1063/1.5005764.
- 135. Y. Shi, D. Xiong, J. Li, K. Wang and N. Wang. In situ repair of graphene defects and enhancement of its reinforcement effect in polyvinyl alcohol hydrogels. RSC Adv., 2017, 7, 1045.
- 136. A. K. Das, M. Srivastav, R. K. Layek, Md. E. Uddin, D. Jung, N. H. Kima and J. H. Lee. Iodide-mediated room temperature reduction of graphene oxide: a rapid chemical route for the synthesis of a bifunctional electrocatalyst. J. Mater. Chem. A, 2014, 2, 1332–1340.
- 137. M. Assali, A.l Naser Zaid, F. Abdallah, M. Almasri, R. Khayyat. Single-walled carbon nanotubes-ciprofloxacin nanoantibiotic: strategy to improve ciprofloxacin antibacterial activity. International Journal of Nanomedicine. Volume 2017:12 Pages 6647—6659.
- 138. J. C. Valmalette, Z. Tan, H. Abe & S. Ohara. Raman scattering of linear chains of strongly coupled Ag nanoparticles on SWCNTs. Scientific Reports, 4, 5238.
- 139. Y. Zhang, Y. Zhu, G. Lin, R. S. Ruoff, N. Hud, D. W. Schaefer, J. E. Mark. What factors control the mechanical properties of poly (dimethylsiloxane) reinforced

- with nanosheets of 3-aminopropyltriethoxysilane modified graphene oxide? Polymer 54, 2013, 3605-3611.
- 140. L. M. Johnson, L. Gao, C. W. Shields, M. Smith, K. Efimenko, K. C. J. Genzer and G. P. López. Elastomeric microparticles for acoustic mediated Bioseparations. Journal of Nanobiotechnology 2013, 11-22.
- 141. M. Rezakazemi, A. Vatania, and T. Mohammadi. Synergistic interactions between POSS and fumed silica and their effect on the properties of crosslinked PDMS nanocomposite membranes. RSC Adv., 2015, 5, 82460–82470.
- 142. H. D. Shetty, A. Patra, and V. Prasad. Polydimethylsiloxane-multiwalled carbon nanotube composite as a metamaterial. Materials Letters 210 (2018) 309–313.
- 143. X. Fan, F. Khosravi, V. Rahneshin, M. Shanmugam, M. Loeian, J. Jasinski, R. W Cohn, E. Terentjev and B. Panchapakesan. MoS2 actuators: reversible mechanical responses of MoS2-polymer nanocomposites to photons. Nanotechnology 26, 2015, 261001 (11pp).
- 144. M. H. Al-Saleh. Carbon-based Polymer nanocomposites as dielectric energy storage materials. Nanotechnology, 2019, 30, 062001.
- 145. S. Song, Y. Zhai, and Y. Zhang.Bioinspired Graphene Oxide/Polymer Nanocomposite Paper with High Strength, Toughness, and Dielectric Constant. ACS Appl. Mater. Interfaces 2016, 8, 31264–31272.
- 146. J. Yuan, W. Neri, C. Zakri, P. Poulin, and A. Colin. Electrostrictive polymer composites based on liquid crystalline graphene for mechanical energy harvesting. Proceeding IEEE, 2018,978-1-5386-6389-9.
- 147. I. Tantis, G. C. Psarras, and D. Tasis. Functionalized graphene poly(vinyl alcohol) nanocomposites: Physical and dielectric properties. Express Polymer Letters Vol.6, No.4, 2012, 283–292.
- 148. G. Sahu, M. Das, M. Yadav, B. P. Sahoo, and J. Tripathy. Dielectric Relaxation Behavior of Silver Nanoparticles and Graphene Oxide Embedded Poly(vinyl alcohol) Nanocomposite Film: An Effect of Ionic Liquid and Temperature. Polymers 2020, 12, 374.
- 149. J. Bian, Q. Zhao, Z. Hou, J. Dong, Q. Yang, and G. Zhang. Effect of alumina shapes on dielectric properties of UV-cured epoxy acrylic composite with alumina. Royal Society Open Science, 6, 2018, 181509.
- 150. I. S. Yahia, and M. I. Mohammed. Facile synthesis of graphene oxide/PVA nanocomposites for laser optical limiting: bandgap analysis and dielectric constants. Journal of Materials Science: Materials in Electronics, 29, 2018, 8555–8563.
- 151. C. Yang, H. Wei, L. Guan, J. Guo, Y. Wang, X. Yan, X. Zhang, S. Wei, and Z. Guo. Polymer nanocomposites for energy storage, energy-saving, and anticorrosion. J. Mater. Chem. A, 2015, 3, 14929–14941.
- 152. G. C. Psarras. Hopping conductivity in polymer matrix-metal particles composites. Composites Part A: Applied Science and Manufacturing, 37, 2006, 1545–1553.
- 153. Z. Wang, J. K. Nelson, H. Hillborg, S. Zhao, and L. S. Schadler. Graphene Oxide Filled Nanocomposite with Novel Electrical and Dielectric Properties. Adv. Mater. 2012, 24, 3134–3137.

Development of nanomaterials incorporated PDMS-based smart materials for flexible and wearable sensors

by Bikash Borah

Submission date: 26-Aug-2021 02:21PM (UTC+0530)

Submission ID: 1636185454

File name: Bikash_Thesis_new.pdf (9.62M)

Word count: 21366 Character count: 109462

Development of nanomaterials incorporated PDMS-based smart materials for flexible and wearable sensors

ORIGINALITY REPORT

SIMILARITY INDEX

INTERNET SOURCES

PUBLICATIONS

STUDENT PAPERS

<1%

<1%

PRIMARY SOURCES

Shuai Wang, Peng Xiao, Yun Liang, Jiawei Zhang, Youju Huang, Si Wu, Shiao-Wei Kuo, Tao Chen. "Network cracks-based wearable strain sensors for subtle and large strain detection of human motions", Journal of Materials Chemistry C, 2018

Publication

Xiuhua Zhao, Wei Xu, Wangmin Yi, Yitian Peng. "A flexible and highly pressure-sensitive PDMS sponge based on silver nanoparticles decorated reduced graphene oxide composite", Sensors and Actuators A: Physical, 2019

Publication

iopscience.iop.org

Internet Source

5

worldwidescience.org Internet Source

Biao Yin, Yanwei Wen, Tao Hong, Zhongshuai

Xie, Guoliang Yuan, Qingmin Ji, Hongbing Jia.

"Highly Stretchable, Ultrasensitive, and Wearable Strain Sensors Based on Facilely Prepared Reduced Graphene Oxide Woven Fabrics in an Ethanol Flame", ACS Applied Materials & Interfaces, 2017

Publication

6	pubs.rsc.org Internet Source	<1%
7	www.freepatentsonline.com Internet Source	<1%
8	Submitted to Gachon University Student Paper	<1%
9	Chandramika Bora, Jahnabi Sharma, Swapan Dolui. "Polypyrrole/Sulfonated Graphene Composite as Electrode Material for Supercapacitor", The Journal of Physical Chemistry C, 2014 Publication	<1%
10	Lu Wang, Yimin Zhou. "Stable visible light photocatalyst based on the graphene protected Ag PO nanocomposite ", Fullerenes, Nanotubes and Carbon Nanostructures, 2016 Publication	<1%
11	nanoscalereslett.springeropen.com Internet Source	<1%
12	Qi Li, Jin Li, Danhquang Tran, Chengqiang Luo,	<1%

Yang Gao, Cunjiang Yu, Fuzhen Xuan.

"Engineering of carbon nanotube/polydimethylsiloxane nanocomposites with enhanced sensitivity for wearable motion sensors", Journal of Materials Chemistry C, 2017

"Advanced Carbon Materials and Technology", Wiley, 2014

<1%

Publication

Amit A. Vernekar, Govindasamy Mugesh.
"Hemin-Functionalized Reduced Graphene
Oxide Nanosheets Reveal Peroxynitrite
Reduction and Isomerization Activity",
Chemistry - A European Journal, 2012
Publication

<1%

Hyokeun Lee, Min Jung Kim, Jong Hun Kim, Jong-Young Lee et al. "Highly flexible graphene-polydimethylsiloxane strain sensors with proximity-sensing capability", Materials Research Express, 2020

<10/

Riccardo Goldoni, Yasemin Ozkan-Aydin, Yun-Soung Kim, Jongsu Kim et al. "Stretchable Nanocomposite Sensors, Nanomembrane Interconnectors, and Wireless Electronics toward Feedback–Loop Control of a Soft Earthworm Robot", ACS Applied Materials & Interfaces, 2020

<1%

Publication

17	kyutech.repo.nii.ac.jp Internet Source	<1%
18	www.worldscientificnews.com Internet Source	<1%
19	doktori.bibl.u-szeged.hu Internet Source	<1%
20	epub.uni-bayreuth.de Internet Source	<1%
21	K. Hareesh, R.P. Joshi, S.S. Dahiwale, V.N. Bhoraskar, S.D. Dhole. "Synthesis of Agreduced graphene oxide nanocomposite by gamma radiation assisted method and its photocatalytic activity", Vacuum, 2016 Publication	<1%
22	Kazem Shahidi, Denis Rodrigue. "Production of Composite Membranes by Coupling Coating and Melt Extrusion/Salt Leaching", Industrial & Engineering Chemistry Research, 2017 Publication	<1%
23	Peng Zhang, Yucheng Chen, Yuxia Li, Yao Zhang, Jian Zhang, Liangsong Huang. "A Flexible Strain Sensor Based on the Porous Structure of a Carbon Black/Carbon Nanotube Conducting Network for Human Motion Detection", Sensors, 2020 Publication	<1%

24	Thangavelu Palaniselvam, Harshitha Barike Aiyappa, Sreekumar Kurungot. "An efficient oxygen reduction electrocatalyst from graphene by simultaneously generating pores and nitrogen doped active sites", Journal of Materials Chemistry, 2012 Publication	<1%
25	aip.scitation.org Internet Source	<1%
26	Zhenhua Tang, Shuhai Jia, Fei Wang, Changsheng Bian, Yuyu Chen, Yonglin Wang, Bo Li. "Highly Stretchable Core–Sheath Fibers via Wet-Spinning for Wearable Strain Sensors", ACS Applied Materials & Interfaces, 2018 Publication	<1%
27	www.reiner-lemoine-stiftung.de Internet Source	<1%
28	Amir khan, Ravi Reddy, Chinmayananda Gouda, Dipti Gupta, Hong-Cheu Lin. "Highly Stretchable Supramolecular Conductive Self- Healable Gels for Injectable Adhesive and Flexible Sensor Applications", Journal of Materials Chemistry A, 2020 Publication	<1%
29	Hu Liu, Qianming Li, Yibing Bu, Na Zhang, Chunfeng Wang, Caofeng Pan, Liwei Mi,	<1%

Zhanhu Guo, Chuntai Liu, Changyu Shen. "Stretchable conductive nonwoven fabrics with self-cleaning capability for tunable wearable strain sensor", Nano Energy, 2019

<1%

<1%

<1%

<1%

James Taban Abdalla, Jinzhong Wang, Dongbo Wang. "Effect of Ag/rGO on the Optical Properties of Plasmon-Modified SnO2 Composite and Its Application in Self-Powered UV Photodetector", Crystals, 2019

Publication

Publication

Publication

- Kanoun, Olfa, Christian Müller, Abderahmane Benchirouf, Abdulkadir Sanli, Trong Dinh, Ammar Al-Hamry, Lei Bu, Carina Gerlach, and Ayda Bouhamed. "Flexible Carbon Nanotube Films for High Performance Strain Sensors", Sensors, 2014.
- Mikhail A. Kanygin, Mahnaz Shafiei, Behraad Bahreyni. "Electrostatic Twisting of Core-Shell Nanofibers for Strain Sensing Applications", ACS Applied Polymer Materials, 2020
- Seong Jun Kim, Shuvra Mondal, Bok Ki Min, Choon-Gi Choi. " Highly Sensitive and Flexible Strain-Pressure Sensors with Cracked Paddy-Shaped MoS /Graphene Foam/Ecoflex Hybrid

Nanostructures ", ACS Applied Materials & Interfaces, 2018

Publication

Vera Schroeder, Suchol Savagatrup, Maggie He, Sibo Lin, Timothy M. Swager. "Carbon Nanotube Chemical Sensors", Chemical Reviews, 2018

<1%

Publication

Publication

etheses.bham.ac.uk

<1%

C N R Rao, K S Subrahmanyam, H S S Ramakrishna Matte, B Abdulhakeem et al. "A study of the synthetic methods and properties of graphenes", Science and Technology of Advanced Materials, 2016

< 1 %

Jing Chen, Jinjie Zhang, Zebang Luo, Jinyong Zhang et al. "Superelastic, Sensitive, and Low Hysteresis Flexible Strain Sensor Based on Wave-Patterned Liquid Metal for Human Activity Monitoring", ACS Applied Materials & Interfaces, 2020

<1%

Songfang Zhao, Jinhui Li, Duxia Cao, Guoping Zhang, Jia Li, Kui Li, Yang Yang, Wei Wang, Yufeng Jin, Rong Sun, Ching-Ping Wong.

"Recent Advancements in Flexible and Stretchable Electrodes for Electromechanical

<1%

Sensors: Strategies, Materials, and Features", ACS Applied Materials & Interfaces, 2017

Publication

39

Tingyu Li, Jinhui Li, Ao Zhong, Fei Han, Rong Sun, Ching-Ping Wong, Fangfang Niu, Guoping Zhang, Yufeng Jin. "A flexible strain sensor based on CNTs/PDMS microspheres for human motion detection", Sensors and Actuators A: Physical, 2020

<1%

Publication

Exclude quotes On Exclude bibliography On

Exclude matches

< 14 words